

# Quantum gas apparatus for Bose-Einstein condensation of $^{87}\text{Rb}$

by

Taras Hrushevskyi

A thesis submitted in partial fulfillment of the requirements for the degree of

Master of Science

Department of Physics

University of Alberta

©Taras Hrushevskyi, 2017

# *Abstract*

In a Bose-Einstein Condensate (BEC), due to extremely low temperatures, wave functions of all particles in the system overlap and form a single macroscopic wavefunction. This brings quantum mechanical effects to the macroscopic scale and allows us to better understand known quantum mechanical laws and effects, as well as develop new ones. In addition to being of fundamental scientific interest, BEC can serve in practical applications, such as quantum metrology, atomic interferometry, and quantum information and communication.

Here we describe our approach for producing BECs in  $^{87}\text{Rb}$ . To create atomic flux towards our science chamber, a 2-dimensional magneto-optical trap (2D-MOT) with push beam is used. The initial atomic cloud is formed in 15 s by 3D-MOT and consists of  $10^9$  atoms at  $500\ \mu\text{K}$ . After the MOT, atoms are cooled with optical molasses to  $50\ \mu\text{K}$  and transferred to a quadrupole magnetic trap, where radio-frequency (RF) induced evaporation is performed, which lowers temperature to  $10\ \mu\text{K}$ . After RF evaporation, the atomic cloud is transferred to a crossed beams optical dipole trap (ODT). During evaporation in the ODT, the temperature is reduced below the critical temperature  $T_c=286\ \text{nK}$ , where condensation starts, and eventually reaches  $40\ \text{nK}$ . As a result, a quasi-pure BEC with  $10^5\ ^{87}\text{Rb}$  atoms is formed. The complete sequence from the MOT loading to the BEC formation takes about 30 s. Observations of the inversion of the aspect ratio of the cloud during free expansion and a bimodal velocity distribution prove quantum degeneracy.

Presented in this thesis are the necessary background for understanding the experimental steps, a description of the schemes and technical details of our setup, and a characterizations of all the experimental steps.

## *Preface*

The BEC apparatus and experiment were designed by Dr. Lindsay LeBlanc.

The vacuum system was designed by Dr. Lindsay LeBlanc, and assembled by Dr. Lindsay LeBlanc and Greg Popowich. The oven region was rebuilt few times by Dr. Lindsay LeBlanc, Greg Popowich, Dr. Erhan Saglamyurek and myself. Custom holders for vacuum parts, for coils and for optics were designed by Dr. Lindsay LeBlanc and produced by Greg Popowich.

The temperature controller for oven was designed and built by Dr. Lindsay LeBlanc, upgraded by myself.

Pneumatic mirrors mounts were designed by Roger C. Brown, S. Olmschenk, Saijun Wu, A. M. Dyckovsky, R. Wyllie, and J. V. Porto<sup>1</sup>, produced in University of Alberta Physics Machine Shop, upgraded by Greg Popowich and myself, installed and aligned by Dr. Erhan Saglamyurek and myself.

The cooling and repump lasers optical setups were set up and aligned by Dr. Lindsay LeBlanc, Dr. Erhan Saglamyurek and myself. The beat note locking system was installed by Dr. Lindsay LeBlanc.

The radio frequency circuit was designed by Dr. Lindsay LeBlanc, assembled and installed by myself.

The 2D-MOT optics on vacuum system were installed by Dr. Lindsay LeBlanc and aligned by Andrei Tretiakov and myself, recently realigned by Dr. Erhan Saglamyurek and myself. The 3D-MOT optics on vacuum system were installed by Dr. Lindsay LeBlanc; then (a few times) disassembled, assembled and aligned by Dr. Erhan Saglamyurek and myself.

The side imaging system was designed by Dr. Lindsay LeBlanc and assembled by myself; upgraded, aligned and characterized by Dr. Erhan Saglamyurek and myself. The bottom imaging system was designed, assembled and installed by Dr. Lindsay LeBlanc and William Morrish; aligned and characterized by Dr. Erhan Saglamyurek and myself.

The 2D- and 3D-MOT coils were designed by Dr. Lindsay LeBlanc, produced and installed by Greg Popowich. The current control system was designed by Dr. Ian Spielman (NIST), modified by Dr. Lindsay LeBlanc, set up by Greg Popowich, upgraded and calibrated by Dr. Erhan Saglamyurek and myself.

The bias coils were designed by Dr. Lindsay LeBlanc, produced, characterized and installed by Andrei Tretiakov and myself.

The optical dipole trap setup was designed by Dr. Lindsay LeBlanc and Alice Shen, assembled by myself, installed, upgraded, aligned and characterized by Dr. Erhan Saglamyurek and myself.

Experiment control software was written by Drs. I. Spielman and J.V. Porto at NIST and adapted by Dr. Lindsay LeBlanc.

The image acquisition software was written by Dr. Lindsay LeBlanc and William Morrish, fundamentally upgraded by Dr. Lindsay LeBlanc. The data analysis software was written by Dr. Lindsay LeBlanc and Scott Wilson.

Experimental steps were optimized and characterized by Dr. Lindsay LeBlanc, Dr. Erhan Saglamyurek and myself.

## *Acknowledgements*

I would like to thank:

Dr. Lindsay LeBlanc, for being an awesome supervisor, for her support, guidance and great patience during my Master's program; for never being busy to meet me and answer my questions; for the huge amount of work she did to design the BEC setup and to make it work; for her help with thesis preparation, advice, discussing content, reading the whole document, and the innumerable corrections she put there.

Dr. Frank Hegmann and Dr. Joseph Maciejko for agreeing to be in my committee, for their support and understanding.

Greg Popowich for building the vacuum system, for building and maintaining all the necessary parts of the setup, for reacting fast to vacuum leaks even after the end of working hours.

Dr. Erhan Saglamyurek, the person with whom we spend almost every day of the last year and a half in the lab; for his work on the BEC setup; for his optimism; for his great knowledge and experience in laser and fiber optics, quantum memory and other fields that he generously shares with me and other people; for his advice including those about my thesis and corrections he provided.

Andrei Tretiakov for his work on the BEC setup during the initial stages and occasional help after he started the Hybrid system project; for sharing with me a week of building the bias coils; for discussions on thesis content, especially the theory sections; for his help with LaTeX and Python.

Scott Wilson for doing Python programming for data acquisition and analysis.

William Morrish for building imaging system.

Ben Smith for volunteering to proof read my thesis, for valuable notices and corrections.

Anindya Rastogi for occasional help in the lab and sharing his optics parts.

Logan Cooke, Jacques Thibault, as well as the other group members for making an awesome, friendly atmosphere in the lab and in the group's office, and for all our fun during non-academic activities.

Oleksandr Bohomolov for his help with 3D image creation.

Vel ([www.LaTeXTemplates.com](http://www.LaTeXTemplates.com)) for making great LaTeX template.

University of Alberta and Department of Physics for the chance to study and work in such a great place.

And last, but not the least, my parents Bohdan and Roma, my sister Iaryna, and all my friends for their support and belief in me.

# Contents

|  |            |
|--|------------|
| <b>Abstract</b>  | <b>ii</b>  |
| <b>Preface</b>   | <b>iii</b> |
| <b>Acknowledgements</b>                                      | <b>v</b>   |
| <b>1 Introduction</b>  | <b>1</b>   |
| <b>2 Background</b>  | <b>3</b>   |
| 2.1 Basic principles of laser cooling and trapping . . . . . | 3          |
| 2.1.1 Laser (Doppler) cooling . . . . .                      | 3          |
| 2.1.2 Polarization gradient (sub-Doppler) cooling . . . . .  | 5          |
| Motion induced orientation cooling . . . . .                 | 5          |
| Sisyphus cooling . . . . .                                   | 7          |
| 2.1.3 Optical dipole trap . . . . .                          | 9          |
| 2.1.4 Magneto-optical trap . . . . .                         | 10         |
| 2.2 Magnetic trap . . . . .                                  | 12         |
| 2.3 Evaporation cooling . . . . .                            | 14         |
| RF evaporation from magnetic trap . . . . .                  | 16         |
| Evaporation from ODT . . . . .                               | 16         |
| 2.4 Bose-Einstein condensate . . . . .                       | 17         |
| 2.4.1 Non-interacting Bose gas . . . . .                     | 17         |
| 2.4.2 Interacting BEC in a trap . . . . .                    | 19         |
| 2.5 Imaging . . . . .  | 21         |
| <b>3 BEC setup</b>   | <b>26</b>  |
| 3.1 Ultrahigh vacuum system . . . . .                        | 27         |
| 3.1.1 Main parts of the vacuum system . . . . .              | 28         |
| 3.1.2 Cleaning and Bakeout . . . . .                         | 31         |
| 3.2 Magnetic field control . . . . .                         | 33         |
| 3.2.1 2D-MOT coils . . . . .                                 | 34         |
| 3.2.2 3D-MOT/MT coils . . . . .                              | 35         |
| 3.2.3 Bias coils . . . . .                                   | 40         |

|          |  |           |
|----------|--|-----------|
| 3.2.4    | Radio frequency circuit  | 41        |
| 3.2.5    | Pneumatic mirror mounts  | 43        |
| 3.3      | Lasers and Optics  | 44        |
| 3.3.1    | Repump laser   | 46        |
|          | "4 to 4" and "4 to 6" fiber beam splitters                             | 49        |
| 3.3.2    | Cooling laser  | 49        |
|          | Beat note locking  | 52        |
|          | Cooling laser's optical setup  | 54        |
| 3.3.3    | Imaging  | 56        |
|          | Pixel size calibration   | 58        |
| 3.3.4    | Optical dipole trap  | 60        |
|          | Optical dipole trap alignment  | 62        |
| <b>4</b> | <b>Results</b>   | <b>66</b> |
| 4.1      | Experimental sequence  | 66        |
| 4.2      | Magneto-optical traps  | 67        |
| 4.3      | Polarization gradient cooling  | 74        |
| 4.4      | Magnetic trapping  | 76        |
| 4.4.1    | Optical pumping  | 76        |
| 4.4.2    | Magnetic trap (MT)   | 76        |
|          | MT compression   | 77        |
|          | Magnetic trap lifetime   | 78        |
| 4.5      | Evaporative cooling  | 79        |
| 4.5.1    | Radio frequency induced evaporation from quadrupole mag-<br>netic trap | 79        |
|          | Transfer to ODT and Decompression.                                     | 80        |
| 4.5.2    | Forced evaporation from optical-dipole trap: Achieving BEC             | 83        |
|          | Trap frequency   | 83        |
| 4.6      | BEC signatures   | 85        |
| 4.6.1    | Aspect ratio inversion during free expansion                           | 86        |
| 4.6.2    | Bimodality in velocity distribution                                    | 86        |
| <b>5</b> | <b>Conclusions</b>   | <b>90</b> |

# List of Figures

|      |  |    |
|------|--|----|
| 2.1  | Level scheme and Clebsh-Gordan coefficient for atom with three Zeeman levels in ground state . . . . . | 6  |
| 2.2  | Sisyphus cooling scheme . . . . .  | 7  |
| 2.3  | Level scheme and Clebsh-Gordan coefficient for atom with two Zeeman levels in ground state. . . . .    | 8  |
| 2.4  | Operation principle of magneto-optical trap . . . . .  | 11 |
| 2.5  | General principle of evaporative cooling . . . . .   | 14 |
| 2.6  | Scheme for evaporation from a magnetic trap and an optical dipole trap                                 | 16 |
| 2.7  | Example of raw and processed images for absorption imaging technique. . . . .                          | 22 |
| 2.8  | Example of temperature measurements. . . . .   | 24 |
| 3.1  | Vacuum system 3D model . . . . .   | 27 |
| 3.2  | Oven . . . . .   | 29 |
| 3.3  | Flexible bellow . . . . .  | 30 |
| 3.4  | 2D-MOT coils . . . . .   | 34 |
| 3.5  | 2D-MOT coils current control scheme . . . . .  | 36 |
| 3.6  | 3D-MOT coils . . . . .   | 37 |
| 3.7  | MOSFETs bank . . . . .   | 38 |
| 3.8  | 3D-MOT/MT current control . . . . .  | 39 |
| 3.9  | Bias coils together with 3D-MOT/MT coils mounted on the cage around glass cell . . . . .               | 41 |
| 3.10 | Radio-frequency circuit . . . . .  | 42 |
| 3.11 | Horizontal pneumatic mirror mounts . . . . .   | 44 |
| 3.12 | Vertical pneumatic mirror mounts . . . . .   | 45 |
| 3.13 | Legend for optical components . . . . .  | 46 |
| 3.14 | Cooling laser's optical setup . . . . .  | 47 |
| 3.15 | 2D-MOT 4 to 4 splitter . . . . .   | 50 |
| 3.16 | 3D-MOT 4 to 6 splitter . . . . .   | 51 |
| 3.17 | Beat note locking scheme . . . . .   | 53 |
| 3.18 | Cooling laser's optical setup . . . . .  | 55 |

|      |   |    |
|------|---|----|
| 3.19 | Imaging systems optical setups . . . . .  | 57 |
| 3.20 | Free fall measurements for pixel calibration . . . . .  | 59 |
| 3.21 | Optical dipole trap setup . . . . .   | 61 |
| 3.22 | ODT Power and Splitt AOM calibration . . . . .  | 62 |
| 3.23 | ODT alignment data . . . . .  | 63 |
| 3.24 | Absorption images of the atomic cloud before and after transfer to the ODT . . . . .                      | 64 |
| 4.1  | $^{87}\text{Rb}$ $D_2$ transition level diagram with marked transitions used for our experiment . . . . . | 69 |
| 4.2  | Spatial configuration of the beams in 3D-MOT. . . . .   | 71 |
| 4.3  | 3D-MOT loading time . . . . .   | 72 |
| 4.4  | Typical 3D-MOT absorption image . . . . .   | 73 |
| 4.5  | Typical molasses absorption image . . . . .   | 75 |
| 4.6  | Optical pumping scheme for moving $^{87}\text{Rb}$ atoms into $ F = 2, m_F = 2\rangle$ state . . . . .    | 77 |
| 4.7  | Magnetic trap lifetime . . . . .  | 78 |
| 4.8  | Characteristics of the evaporation cooling . . . . .  | 81 |
| 4.9  | Phase space density and atom number change as function of evaporation time . . . . .                      | 82 |
| 4.10 | The velocity distributions for thermal, transition and condensed clouds . . . . .                         | 84 |
| 4.11 | Optical dipole trap frequency measurements . . . . .  | 85 |
| 4.12 | Inversion of aspect ratio in a free expanding BEC . . . . .   | 87 |
| 4.13 | Bimodal fits to the cross sections of the clouds with different condensate fraction . . . . .             | 89 |

# List of Tables

|     |  |    |
|-----|--|----|
| 3.1 | Vacuum parts specifications. . . . .         | 32 |
| 3.2 | 2D-MOT coil resistance. . . . .              | 35 |
| 3.3 | Imaging system pixel size . . . . .          | 59 |
| 4.1 | 2D- and 3D-MOT light power levels. . . . .   | 68 |
| 4.2 | Optical molasses light power levels. . . . . | 74 |

# Chapter 1

## Introduction

Cold atom physics is one of the most fascinating research fields that has brought endless possibilities to study quantum phenomena using atoms. In particular, the possibility of cooling atoms down to the nano-kelvin regime (ultracold), which is the lowest achievable temperature range in the universe, has opened an avenue for performing experimental and theoretical studies that would not be possible in any other way.

The experimental realization of Bose-Einstein condensate (BEC) is a unique example of what is achievable with ultracold atoms. Predicted theoretically in 1924-25 by Albert Einstein and Satyendra Nath Bose, BEC was produced for the first time in atomic vapours in 1995 from  $^{87}\text{Rb}$  vapour by Eric Cornell and Carl Wieman's group [1]. Since that time ultracold atom physics developed rapidly and the number of condensed isotopes continually rises. Between them are  $^1\text{H}$  [2],  $^7\text{Li}$  [3],  $^{23}\text{Na}$  [4],  $^{39}\text{K}$  [5],  $^{40}\text{Ca}$  [6],  $^{41}\text{K}$  [7],  $^{52}\text{Cr}$  [8],  $^{84}\text{Sr}$  [9],  $^{85}\text{Rb}$  [10],  $^{86}\text{Sr}$  [11],  $^{88}\text{Sr}$  [12],  $^{133}\text{Cs}$  [13],  $^{164}\text{Dy}$  [14],  $^{168}\text{Er}$  [15],  $^{168}\text{Yb}$  [16], and  $^{174}\text{Yb}$  [16].

A BEC is described by a quantum mechanical ground state of (typically  $10^3 - 10^6$ ) bosonic atoms that are completely indistinguishable in any degree of freedom. This feature of a BEC results in the creation of a very large quantum mechanical object. In this way, it is possible to observe and study the "wave nature of matter" at macroscopic scales by means of BECs. This is the essence of the field of matter-wave interferometry using ultracold atoms, which allows for fundamental tests of quantum mechanics and as well as developing metrology tools for very sensitive measurements: atomic interferometry [17, 18, 19], frequency stabilization [20], and atomic clocks [21, 22]. Furthermore, precise control of quantum matter-waves associated

with ultracold atoms allows one to observe and investigate exotic quantum phenomena such as vortex formation [23, 24], dark solitons [25, 26] and other many-body quantum effects.

In addition, the possibility of trapping and precisely positioning ultracold quantum gases in different sites of artificial lattice structure formed by light, the ability to manipulate them by tuning their background environment and interactions between atoms, make such systems an excellent platform to simulate quantum phenomena in condensed matter systems, like spin-orbit coupling [27, 28, 29] and to look for the optimal parameters for new many-body quantum states.

Finally, ultracold atoms allows precise control over not only motional degrees of freedom but also internal degrees of freedom such as spin states with very long coherence times. This makes ultracold atoms attractive tools for quantum information processing applications; they can be used to stop light for quantum information storage [30, 31], to detect single photons without destroying them for quantum communication [32], or to measure extremely low magnetic fields for quantum sensing applications [33].

As mentioned before the study of ultracold atoms brings endless possibilities. On the other hand, the cost we have to pay is the high level of experimental complexity.

In Chapter 2 a brief theory of atom cooling/trapping techniques is presented. This includes principles of Doppler, sub-Doppler and evaporative cooling; and optical dipole, magneto-optical and magnetic trapping. Also, in this chapter some necessary results of trapped Bose-Einstein condensates and principles of absorption imaging are given. Chapter 3 contains a detailed description of our experimental setup. Schemes of main blocks of the apparatus as well as operating parameters are included in this chapter. Chapter 4 presents a description of our experimental sequence and experimental characterizations. Chapter 5 concludes this thesis with a brief discussion of planned experiments for the next steps.

# Chapter 2

## Background

In this chapter I will present background that is necessary for understanding experimental steps and next chapters of this thesis. It describes the idea of laser and evaporation cooling, magnetic, optical dipole and magneto-optical trapping. Also, in this chapter, some basic results for trapped quantum gas are shown. The last section includes the principle of absorption imaging and an approach to imaging analysis.

### 2.1 Basic principles of laser cooling and trapping

There are two types of radiative forces that can act on an atom in a light field - dissipative and dispersive forces [34]. Dissipative forces occur from scattering processes and are caused by momentum transfer from light to atoms. Such scattering forces are used for cooling of atoms. Dispersive forces are associated with a light-intensity-dependent energy level shift (AC Stark effect). Such a light shift can create a potential well or barrier for atoms, depending on detuning. These types of forces are used for atom trapping.

#### 2.1.1 Laser (Doppler) cooling

Laser cooling plays the main role in cooling neutral atoms. The simplest and historically the first (was proposed in 1975 [35]) is Doppler cooling.

Let us consider atoms inside a red detuned (with respect to the atomic transition) beam. For atoms at rest or moving in the direction of beam propagation, absorption

from the beam is negligibly small. But for atoms that move towards the beam, the Doppler shift can compensate detuning. For them, absorption increases drastically. From the absorbed photons, atoms receive energy and momentum. Here we will consider that light intensity is low, so emission is spontaneous. During spontaneous emission, the atom radiates in a random direction and receives no net momentum in any direction upon averaging over many such events. Thus, the force that slows the atom down is [36]

$$\mathbf{F} = \frac{d\mathbf{p}}{dt} = \hbar\mathbf{k}\Gamma_{sc}, \quad (2.1)$$

where  $\mathbf{k}$  is the wave vector,  $\hbar$  is the reduced Planck constant  $\Gamma_{sc}$  is the photon scattering rate

$$\Gamma_{sc} = \frac{s_0\Gamma/2}{1 + s_0 + [2\delta_{eff}/\Gamma]^2}, \quad (2.2)$$

and  $\Gamma$  is the natural linewidth,  $s_0$  is the saturation parameter – the ratio of light intensity to saturation intensity  $I/I_{sat}$ , and  $I_{sat} = \pi\hbar c\Gamma/3\lambda^3$ , where  $c$  is the speed of light in vacuum and  $\lambda$  is the wavelength of light.  $\delta_{eff}$  is the effective detuning in the frame of the atom:

$$\delta_{eff} = \delta + \omega_D, \quad (2.3)$$

$\omega_D = -\mathbf{k} \cdot \mathbf{v}$  is Doppler shift for atom with velocity  $\mathbf{v}$ ,  $\delta$  is the optical detuning:  $\delta = \omega_L - \omega_0$ , where  $\omega_L$  is laser light frequency and  $\omega_0$  is frequency, resonant with an atomic transition.

In presence of two counterpropagating beams, two forces 2.1 from each beam are added and the resulting force is described as [37]:

$$\mathbf{F}_{tot} = \frac{8\hbar k^2 \delta s_0 \mathbf{v}}{\Gamma(1 + s_0 + (2\delta/\Gamma)^2)^2}. \quad (2.4)$$

This force is linearly proportional to the atomic velocity near zero-velocity, which is analogous with viscosity in liquids. For that reason, this laser cooling technique is called optical molasses. Three pairs of counterpropagating beams in mutually orthogonal directions are enough to cool atoms that move in any direction.

For cooling to work, the Doppler shift (velocity) of the atom should match the light's detuning. For constant detuning, beams will address only atoms with a certain velocity. The issue can be solved in two ways. First, adding a magnetic field

gradient will shift atomic levels to different values as atoms move through the field. At different points, atoms with different velocities will be on resonance with the light. So-called Zeeman slowers work on this principle [38, 39, 40]. The other way is to change the detuning of the light in time [41, 42]. This method doesn't require additional magnets. It is just enough to sweep laser frequency, which is why the technique is called "chirp cooling".

Together with cooling, some heating is always present during Doppler cooling because a photon emission process is involved. For spontaneous emission there is some motion associated with the "last" momentum kick, which is always in a random direction - thus thermal. When the velocity of the atom is large and the associated Doppler shift brings laser light close to resonance with the counterpropagating beam, cooling is much stronger than heating. But, as the atom becomes colder, the Doppler shift cannot compensate the light detuning, and absorption from the counterpropagating beam drops while that from the copropagating beam rises. Cooling efficiency drops and at some temperature  $T_D$ , when the two processes equalize each other. The balance between them sets the cooling limit.  $T_D$  is called the Doppler temperature and depends only on natural linewidth [43]

$$T_D = \frac{\hbar\Gamma}{2k_B}. \quad (2.5)$$

For  $^{87}\text{Rb}$ , the Doppler limit is equal to  $145 \mu\text{K}$ .

### 2.1.2 Polarization gradient (sub-Doppler) cooling

For two counterpropagating beams, a complex polarization pattern may occur which causes a cooling effect. We will describe qualitatively two cases that lead to atomic cooling below the Doppler limit:  $\sigma^+ - \sigma^-$  and  $\text{lin} \perp \text{lin}$ . A full theoretical explanation of sub-Doppler cooling is given in [44].

#### Motion induced orientation cooling

Two counter-propagating laser beams with  $\sigma^+$  and  $\sigma^-$  polarization create a standing wave with a polarization gradient – a linear polarization that rotates around the

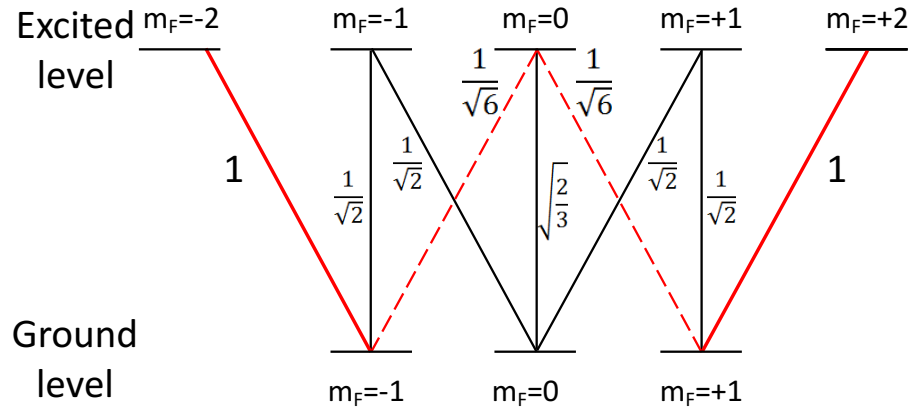


FIGURE 2.1: Level scheme and Clebsch-Gordan coefficient for atoms with three Zeeman levels in ground state. Adapted from [44].

beam's axis. As an atom moves through such a field it sees a rotating polarisation. As a result, an effect known as motion-induced atomic orientation arises. In the simplest case, for an atom with three sublevels  $m_F = 0, \pm 1$  in ground the state, it causes motion-dependent population of  $|g, m_F = +1\rangle$  and  $|g, m_F = -1\rangle$ : if the atom moves towards a  $\sigma^-$  polarized beam,  $|g, m_F = -1\rangle$  is more populated; if an atom moves towards  $\sigma^+$  then  $|g, m_F = +1\rangle$  is more populated.

From the dipole matrix elements for these transitions, an atom in  $|g, m_F = -1\rangle$  state will absorb from  $\sigma^-$  beam with six times higher probability than from  $\sigma^+$  (Fig. 2.1). But due to motion-induced atomic orientation for atoms moving towards  $\sigma^-$ ,  $|g, m_F = -1\rangle$  is more populated. This means that the atoms will absorb more probably from the  $\sigma^-$  - beam against which they move. Since the subsequent emission is a random process, in analogy with Doppler cooling, this acts as a damping force on the atom. The same cooling process works for atoms that move against  $\sigma^+$  beam.

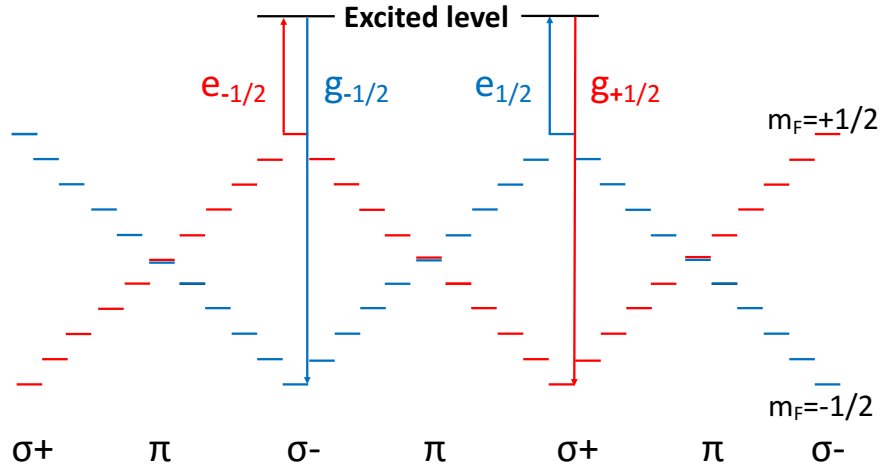


FIGURE 2.2: Sisyphus cooling scheme. Adapted from [44].

### Sisyphus cooling

Two counterpropagating beams with mutually perpendicular linear polarizations create a total field with variable polarization along beams axes: the local polarization changes from linear to circular clockwise then through linear to circular counter-clockwise and so on. In the previous case of  $\sigma^+ - \sigma^-$  polarization total field polarization is always linear and energy shifts due to AC Stark effect for all ground sublevels are the same. But for the case "lin  $\perp$  lin" the energy shift is different for different Zeeman sublevels since polarization changes between  $\pi, \sigma^+$  and  $\sigma^-$ . We will consider the simplest case – an atom that has two sublevels in the ground state. In the region of linear  $\pi$ -polarization, the energy shift is the same for both  $m_F = -1/2$  and  $m_F = +1/2$  levels. In the  $\sigma^-$  region, the shift for  $m_F = -1/2$  is bigger than for  $m_F = +1/2$ . But in the region of  $\sigma^+$  polarization  $m_F = +1/2$  is more shifted than  $m_F = -1/2$  (Fig. 2.2).

Let's say an atom in the  $|g, m_F = +1/2\rangle$  state moves through the polarization gradient created by lin  $\perp$  lin beams starting from the left linear polarization region. As it enters the  $\sigma^-$  region it starts to climb a potential hill. The atomic kinetic energy is transferred into potential energy and it slows down. At the top of the hill, the atom absorbs  $\sigma^-$  light (since it happens in the  $\sigma^-$  region) and jumps into excited state with

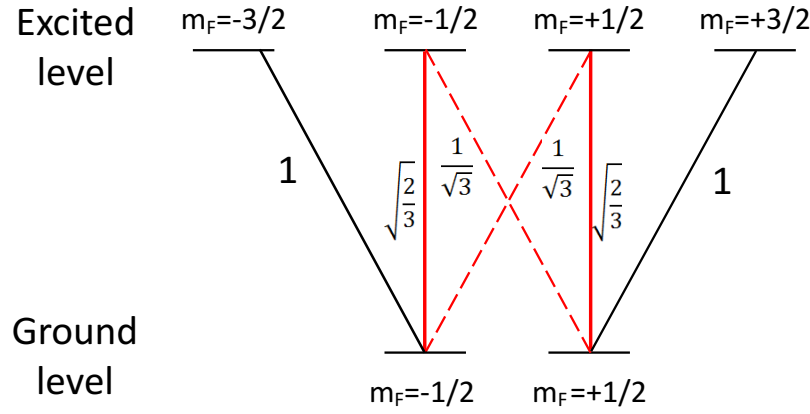


FIGURE 2.3: Level scheme and Clebsch-Gordan coefficient for atom with two Zeeman levels in ground state. Adapted from [44].

$m_F = -1/2$ .

From  $|e, m_F = -1/2\rangle$  with 2 times higher probability (Fig. 2.3) the atom will fall into the  $|g, m_F = -1/2\rangle$  state and emit a photon<sup>1</sup>. Since for  $m_F = -1/2$ , the level energy shift in the  $\sigma^-$  region is larger, the emitted photon has higher energy than the absorbed photon. Now, the atom in the  $|g, m_F = -1/2\rangle$  state enters  $\sigma^+$  and all above described repeats. As a result, the atomic kinetic energy dissipates with spontaneous emission. With analogy to a character from Greek mythology, this cooling scheme is called Sisyphus cooling.

In the lin  $\perp$  lin configuration polarization, changes from  $\sigma^+$  to  $\sigma^-$  inside the region of  $\lambda/2$  size. As temperature of the atom drops, its de Broglie wavelength  $\lambda_{dB}$  increases. At some temperature  $T_{subD}$ ,  $\lambda_{dB}$  reaches  $\lambda/2$  and the atom cannot distinguish the polarization of the region and cooling stops.  $T_{subD}$  is the lowest temperature for polarization gradient cooling:

$$T_{subD} = \frac{\hbar^2 k^2}{2k_B m}, \quad (2.6)$$

where  $k$  is wave vector and  $m$  is atomic mass. For rubidium,  $T_{subD} \simeq 370\text{nK}$ .

<sup>1</sup>Atoms that fall back in  $|g, m_F = +1/2\rangle$  continue their motion down from the potential hill. Their internal energy transforms back into kinetic and process starts again.

Since real experiments includes three pairs of mutually orthogonal counter propagating beams, the polarization pattern becomes complicated. Even though circularly polarized beams are used, (lin  $\perp$  lin) cooling is also present [44].

### 2.1.3 Optical dipole trap

For large detunings  $|\delta| \gg \Gamma$ , stimulated emission dominates over spontaneous [45]. During the stimulated process, the emitted photon has the same direction as the absorbed, and there is no net momentum change for atom and no force. But, the electromagnetic wave interacts with the induced atomic dipole moment. This interaction causes a force acting on the atom which is called the dipole or optical dipole force. The force creates an intensity dependent potential [46]:

$$U_{dip}(\mathbf{r}) = \frac{3\pi c^2 \Gamma}{2\omega_0^3} \frac{I(\mathbf{r})}{\delta}, \quad (2.7)$$

where  $I(\mathbf{r})$  is light field intensity,  $\delta = \omega - \omega_0$  is the detuning of light frequency  $\omega$  from atomic resonant frequency  $\omega_0$ , and  $\Gamma$  is the natural linewidth.

The absorptive part of the dipole interaction is responsible for energy transfer from the driven field to the oscillator which cause re-emission. Since dipole radiation has the same frequency as the driven field, the process can be treated as scattering with rate:

$$\Gamma_{sc}(\mathbf{r}) = \frac{3\pi c^2}{2\hbar\omega_0^3} \left(\frac{\Gamma}{\delta}\right)^2 I(\mathbf{r}). \quad (2.8)$$

Equations 2.7 and 2.8 can be used in these case where  $|\delta| \gg \Gamma$  and  $|\delta| \ll \omega_0$ .

Two important consequences follow from the equations: 1) the type of potential created by light for atoms depends on the sign of detuning  $\delta$ . An atom is attracted into the high intensity region of red detuned ( $\delta < 0$ ) light and is pushed away from blue detuned ( $\delta > 0$ ) beam; 2) the scattering rate drops faster ( $1/\delta^2$ ) with detuning than the potential ( $1/\delta$ ). To reduce scattering, which leads to atoms heating and escaping from the trap, large detunings must be used. To compensate for the weaker potential associated with this large detuning, the beams should have high intensity.

Since, the potential is intensity dependent, red detuned Gaussian beams have an intensity gradient that can create a harmonic<sup>2</sup> trap for cold atoms with trapping potential:

$$U(r, z) = U_0 \left( 1 - \frac{2r^2}{w_0^2} - \frac{z^2}{z_R^2} \right), \quad (2.9)$$

where  $w_0$  is the beam waist,  $z_R$  is the Rayleigh range and  $U_0$  is the trap depth

$$U_0 = \frac{3\pi c^2 \Gamma}{2\hbar\omega_0^3} \frac{2P}{\delta \pi w_0^2}, \quad (2.10)$$

and  $P$  is power in the beam. For small deviations from the centre of this beam, the potential can be considered harmonic, with corresponding radial  $\omega_r$  and axial  $\omega_z$  trap frequencies

$$\begin{aligned} \omega_r &= \sqrt{\frac{4U_0}{mw_0^2}} \\ \omega_z &= \sqrt{\frac{2U_0}{mz_R^2}}. \end{aligned} \quad (2.11)$$

### 2.1.4 Magneto-optical trap

Optical molasses produces a damping force that is proportional to the atomic velocity (eq. 2.4). But, it does not create a position dependent force. Atoms still can diffuse from the molasses region. So, optical molasses does not create a trap for atoms<sup>3</sup>. But if molasses is complemented with a magnetic field gradient, it can efficiently trap atoms. Such a configuration is called a magneto-optical trap (MOT).

The operational principle of the MOT can be described in 1D (Fig. 2.4). A one dimensional magneto-optical trap consists of two counter-propagating red-detuned beams with opposite (with respect to the X axis) circular polarization and magnetic field gradient, with zero magnetic field in the center of the trap and increasing field to its edges. In the simplest case, consider an atom with one magnetic sublevel in the ground state and three in an excited state moving from the center of the trap towards

<sup>2</sup>Gaussian trap can be approximated as harmonic for cold atoms since they are localized near the trap bottom.

<sup>3</sup>Optical molasses can be used as a trap for short period of time and with capture velocity  $\simeq 6$  m/s [36], which is not sufficient for a real experiment.

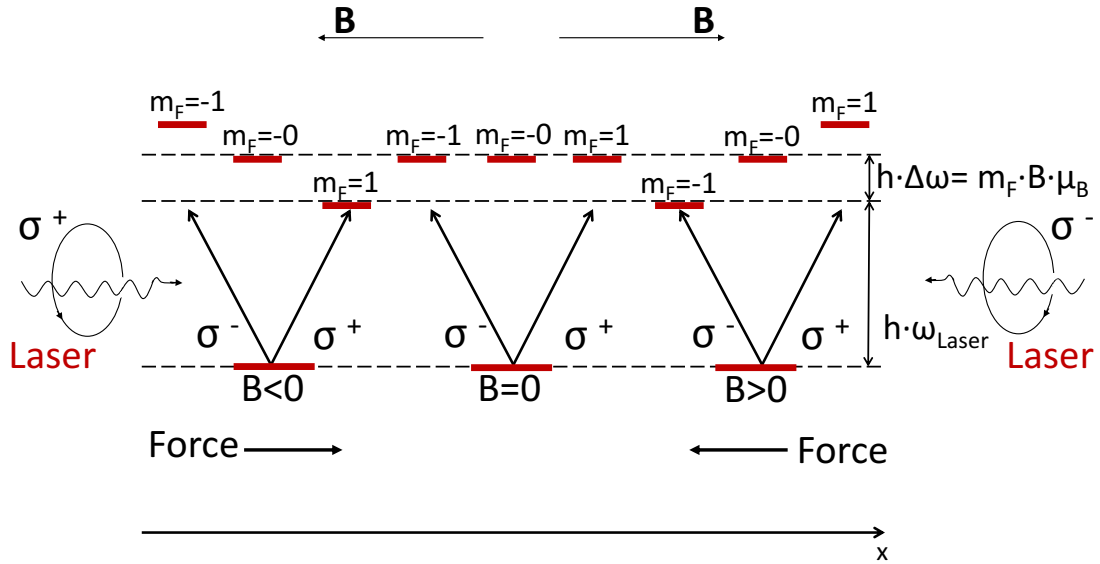


FIGURE 2.4: Operation principle of 1D magneto-optical trap. Adapted from [47].

one of the beams, for example  $\sigma^-$ . Light is red-detuned, so the atom does not absorb. As it moves further, the magnetic field increases and, thus, the Zeeman shift of the magnetic sublevel also increases. The polarization of the beams and magnetic field are tuned in the way that for atom that moves towards  $\sigma^-$ ,  $m_F = -1$  is shifted closer to the ground state. At some point in space, the Zeeman shift compensates the light detuning and the atom absorbs. Since the atom jumps from  $m_F = 0$  to  $m_F = -1$ , it absorbs from the  $\sigma^-$  beam – the beam against which it moves. The same is true for atoms that move towards  $\sigma^+$ . At some point in space, the shift of the  $m_F = +1$  level compensates the detuning and the atom absorbs from  $\sigma^+$  to jump from  $m_F = 0$  to  $m_F = +1$ . This causes a position-dependent force towards the magnetic field zero point, which is the center of the MOT. The expression for the force is the same as 2.4 for molasses but expression for effective detuning 2.3 has an extra term [45]:

$$\delta_{eff} = \delta + \omega_D + \omega_Z, \quad (2.12)$$

where  $\omega_Z$  is the Zeeman shift:

$$\omega_Z = \mu' B / \hbar, \quad (2.13)$$

$\mu' = (g_{exc}m_{Fe} - g_{grd}m_{Fg})\mu_B$  is the effective magnetic moment of the transition from the level with  $m_{Fg}$  to the level with  $m_{Fe}$ , and  $B = B(z)$ . From here, the position-dependent part of the force arises.

With the above described technique, atoms can be trapped in one dimension. For trapping in 3D, usually three pairs of mutually orthogonal beams are used. Two coils in anti-Helmholtz configuration (opposite current direction) create the necessary 3D magnetic field gradient.

The capture velocity of a MOT increases to 30-50 m/s [47] in comparison to  $\simeq 6$  m/s for optical molasses.

The temperature in a MOT is higher than in molasses. This is caused by the presence of the magnetic field that shifts magnetic sublevels which makes sub-Doppler cooling less efficient. So, in the experiment, right after loading a MOT with atoms, the magnetic field is turned off to increase the efficiency of sub-Doppler cooling.

## 2.2 Magnetic trap

For processes that involve laser light near a resonant frequency, like Doppler or sub-Doppler cooling, the limit temperatures  $T_D$  (2.5) and  $T_{subD}$  (2.6) exist. For further cooling and trapping, techniques that do not involve photon absorption-emission processes are required.

For trapping atoms, an optical dipole trap or magnetic trap can be used. The principles of the ODT are described in Subsection 2.1.3. But such traps are narrow (due to the limited size of ODT beam) and often shallow, due to the limited power available, and are useful at late stages of the cooling when atomic cloud is small and dense. To create wide and deep traps, a magnetic field gradient is used.

Due to the Zeeman effect, an atom in a magnetic field experiences a shift of magnetic sublevels. The energy shift  $U$  depends on the state of the atom ( $g_F, m_F$ ) and the

magnetic field magnitude  $B$ <sup>4</sup>:

$$U = g_F m_F \mu_B B, \quad (2.14)$$

where  $\mu_B$  is the Bohr magneton. This means that atomic energy varies with magnetic field. So, the field gradient will cause a force that acts on atoms

$$F = -g_F m_F \mu_B \frac{dB}{dz}. \quad (2.15)$$

The direction of this force depends on the sign of product  $g_F m_F$ : atoms with  $g_F m_F > 0$  will be pulled towards a magnetic field minimum, and are called "low field seekers" meaning that this state is trappable; atoms with  $g_F m_F < 0$  will be pushed out from the trap in the high field direction, and are called "high field seekers" meaning that this state is untrappable.

In real experiments, a quadrupole magnetic field can be used for magnetic trapping. Such a field has a zero magnitude point at the centre from which the field magnitude linearly increases in all directions. Therefore, atoms in a trappable state are pulled to the zero point, the magnetic trap center. A quadrupole magnetic field can be generated with two round coils in anti-Helmholz configuration. For the simplicity of the setup, it is widely used in ultra-cold atoms experiments.

However, the quadrupole configuration has one disadvantage. The projection of total angular momentum is defined with respect to some axis. When a magnetic field is present it sets such an axis and the atom can not change its state. But in the center of the quadrupole trap, the magnetic field is zero. Since there is no quantization axis, atoms can undergo a spin-flip transition into an untrappable state and be pushed out from the trap. This effect is called Majorana spin-flips. The loss region is small – around  $10^{-18} \text{ m}^3$  [45] and for hot atoms is negligible. But as the cloud becomes colder, atoms spend more time around the trap center and Majorana losses become significant. One possible solution of the issue is to transfer atoms into an optical dipole trap.

---

<sup>4</sup>Energy does not depend on field direction since magnetic moment of the atom stays aligned with the field

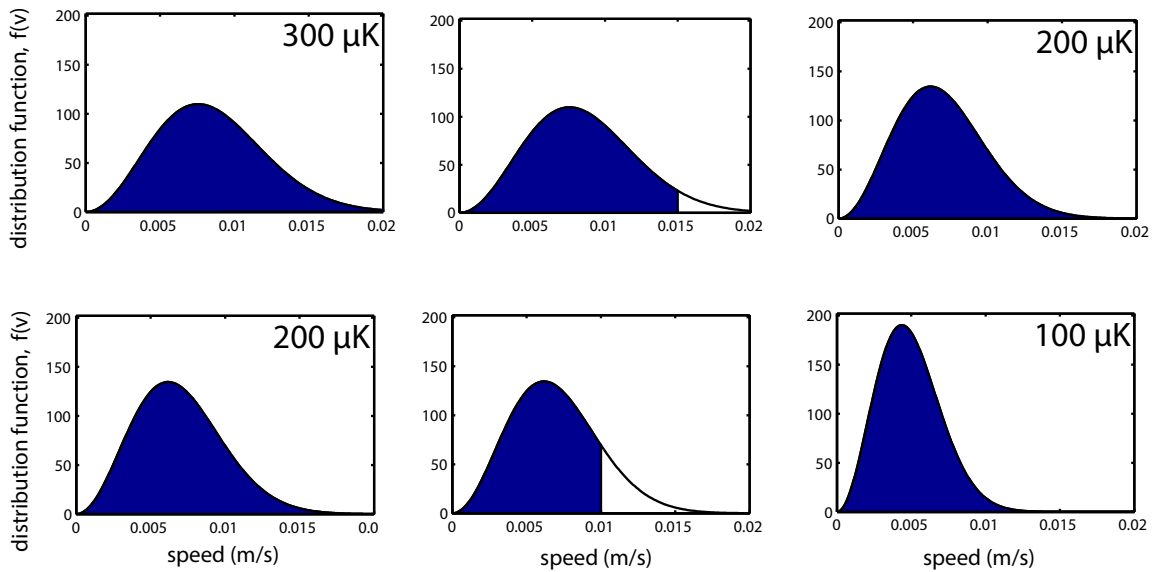


FIGURE 2.5: General principle of evaporative cooling. Total energy of the system is lowered by removing high energetic tail. After each step of evaporation system needs some time for the rethermalization. Image credit: Dr. Lindsay LeBlanc.

## 2.3 Evaporation cooling

At the heart of evaporation cooling lays the simple principle - to remove (evaporate) the most energetic atoms from an atomic cloud. As a result, the average energy of the remaining atoms is lowered.

Evaporative cooling manifests itself by cutting the high energy tail from a Maxwell-Boltzmann distribution and is usually done in few cycles. After each cycle, the cloud must re-thermalize to form a new distribution with a new high energy tail that can be removed (Fig. 2.5). For re-thermalization, atoms must undergo a minimum 2.7 collisions [48]. This means that evaporation must go slowly enough to give atoms time for re-thermalization. On the other hand, the overall evaporation duration is limited by trap lifetime. The speed of the evaporation can be increased by increasing the elastic collision rate. Depending on the efficiency of evaporation, even though

atom number and temperature decrease, density can increase so much that the collision rate also increases and evaporation speed can increase. This regime is called runaway evaporation.

In a quadrupole-type magnetic trap, the average collision rate is proportional to atom number  $N$ , temperature  $T$  and magnetic field gradient in radial direction  $\beta$  [37]

$$R_{col} \propto \frac{N\beta^3}{T^{5/2}}. \quad (2.16)$$

To increase the collision rate and hence make evaporation more efficient, the magnetic trap can be compressed, where the magnetic field gradient is ramped up adiabatically.

During evaporation, the atom number  $N$  and temperature  $T$  are related through the efficiency parameter  $\alpha$  [49]:

$$T \propto N^\alpha, \quad (2.17)$$

where this relationship defines  $\alpha$ . The condition for runaway cooling, based on Eq. (2.16), dictates that the collision rate must increase as both number and temperature decrease. When

$$1 - 2\alpha < 0, \quad (2.18)$$

condition is satisfied, the evaporative cooling process is guaranteed to continue. The main goal of evaporation is to increase phase-space density above some transition value, where Bose-Einstein condensation starts. The overall efficiency of the process can be estimated as [50]:

$$\gamma = -\frac{\log(PSD_f/PSD_i)}{\log(N_f/N_i)}, \quad (2.19)$$

where  $PSD_i$  and  $N_i$  are phase-space density and atom number before evaporation, respectively, and  $PSD_f$  and  $N_f$  are phase-space density and atom number after evaporation. This ratio quantifies the success in increasing phase space density as atom number decreases. The higher this number is, the more atoms remain in the final system, making larger numbers favourable.

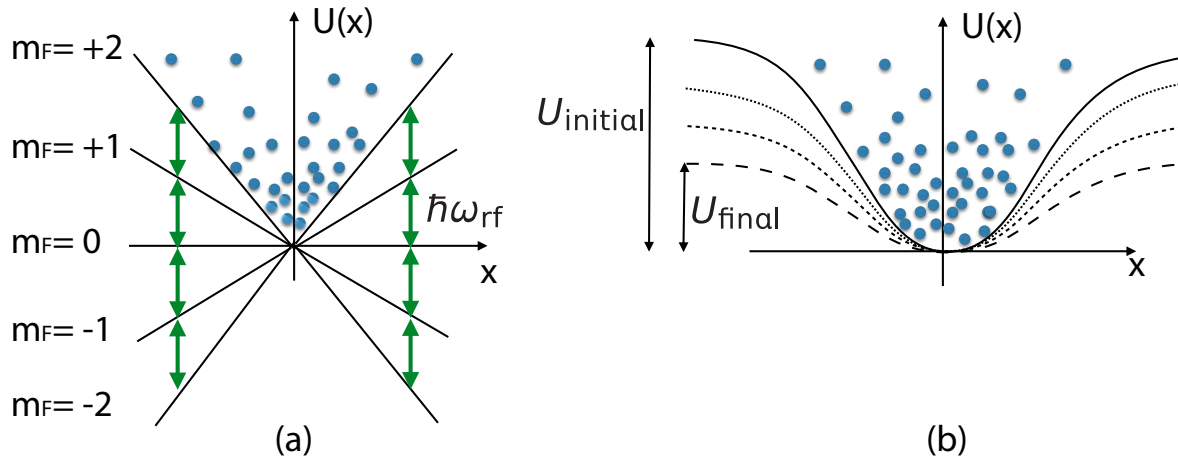


FIGURE 2.6: Scheme for evaporation from a magnetic trap (a) and an optical dipole trap (b). Image credit: Dr. Lindsay LeBlanc.

### RF evaporation from magnetic trap

Evaporation from a magnetic trap can be realized by the forced transition of high energetic atoms into an untrappable state, for example, from  $|F = 2, m_F = 2\rangle$  into  $|F = 2, m_F = -2\rangle$ . The energetic separation between magnetic sublevels is on the order of  $h \times \text{MHz}$ . So, for forced evaporation from the magnetic trap, radiofrequency (RF) radiation is used. RF radiation is tuned in such way that the photon energy  $\hbar\omega_{RF}$  matches the Zeeman splitting between adjacent magnetic sublevels  $g_F\mu_B B(x)$  at those points where only the the most energetic atoms are present: the edges of the trap (Fig. 2.6a). After rethermalization, the RF frequency is swept down to match the level splitting for a new lower-temperature thermal distribution.

### Evaporation from ODT

For evaporation from the optical dipole trap, its depth can be lowered step by step by decreasing power in the laser beams (Fig. 2.6b). Another way is to apply an external force on trapped atoms to modify trapping potential, usually by tilting it so atoms are removed from a "low point" [51].

## 2.4 Bose-Einstein condensate

Bosons are particles of full integer spin and are governed by Bose-Einstein statistics. They have symmetric wavefunctions so, are not subjects to the Pauli exclusion principle. Below some critical temperature  $T_c$ , the population of the lowest quantum state in a bosonic system becomes macroscopic – bosons condense in the single state and form a Bose-Einstein condensate.

BEC is described by a single wavefunction which brings quantum effects to the macroscopic level and makes such system an object of huge scientific interest.

### 2.4.1 Non-interacting Bose gas

Most textbooks treat a uniform system, but we need to consider a trap here because in our experiment condensation occurs in a harmonic optical dipole trap.

For a system of  $N$  noninteracting bosons trapped in potential

$$V(x, y, z) = \frac{m}{2}(\omega_x^2 x^2 + \omega_y^2 y^2 + \omega_z^2 z^2), \quad (2.20)$$

where  $\omega_{x,y,z}$  are the harmonic frequencies of the trapping potential, and  $m$  is the atomic mass, the corresponding energies are

$$\varepsilon_{n_x n_y n_z} = \left(n_x + \frac{1}{2}\right) \hbar\omega_x + \left(n_y + \frac{1}{2}\right) \hbar\omega_y + \left(n_z + \frac{1}{2}\right) \hbar\omega_z, \quad (2.21)$$

where  $n_{x,y,z}$  are the occupations of the harmonic states in each direction. The total number of particles and total energy from the grand canonical ensemble are

$$N = \sum_{n_x, n_y, n_z} \frac{1}{\exp [(\varepsilon_{n_x n_y n_z} - \mu)/k_B T] - 1}, \quad (2.22)$$

$$E = \sum_{n_x, n_y, n_z} \frac{\varepsilon_{n_x n_y n_z}}{\exp [(\varepsilon_{n_x n_y n_z} - \mu)/k_B T] - 1}. \quad (2.23)$$

When the chemical potential  $\mu_c$  reaches the energy of the lowest state  $\varepsilon_{000}$ ,

$$\mu_c = \frac{3}{2}\hbar\bar{\omega}, \quad (2.24)$$

with  $\bar{\omega} = (\omega_x + \omega_y + \omega_z)/3$ , the population of this lowest state  $N_0$ , becomes macroscopic. We separate it in (2.22):

$$N - N_0 = \sum_{n_x, n_y, n_z \neq 0} \frac{1}{\exp[(\hbar(\omega_x n_x + \omega_y n_y + \omega_z n_z)/k_B T) - 1]}. \quad (2.25)$$

For large atom number and closely spaced levels ( $k_B T \gg \hbar\omega_{ho}$  and  $\omega_{ho} = (\omega_x \omega_y \omega_z)^{1/3}$ ) we can replace the sum by an integral

$$N - N_0 = \int_0^\infty \frac{dn_x dn_y dn_z}{\exp[(\hbar(\omega_x n_x + \omega_y n_y + \omega_z n_z)/k_B T) - 1]}, \quad (2.26)$$

which gives the number of thermal atoms.

$$N - N_0 = \zeta(3) \left( \frac{k_B T}{\hbar\omega_{ho}} \right)^3, \quad (2.27)$$

where  $\zeta(3)$  is the Riemann zeta function. With the assumption that at the transition to BEC,  $N_0 = 0$ , this gives the expression for the transition (critical) temperature

$$k_B T_c = \hbar\omega_{ho} \left( \frac{N}{\zeta(3)} \right)^{1/3}. \quad (2.28)$$

If we put this result in (2.27) we will get the fraction of BEC in the system

$$\frac{N_0}{N} = 1 - \left( \frac{T}{T_c} \right)^3. \quad (2.29)$$

Using the peak density for a thermal gas in a harmonic trap:

$$n = N\omega_{ho}^3 \left( \frac{m}{2\pi k_B T} \right)^{3/2} \quad (2.30)$$

from (2.28) we get

$$n \left( \frac{2\pi\hbar^2}{mk_B T_c} \right)^{3/2} = \zeta(3). \quad (2.31)$$

In terms of de-Broglie wavelength

$$\lambda_{dB} = \sqrt{\frac{2\pi\hbar^2}{mk_B T}}, \quad (2.32)$$

(2.31) can be written

$$n\lambda_{dB}^3 = \zeta(3) \approx 1.2. \quad (2.33)$$

The value  $n\lambda_{dB}^3$  is called phase space density (PSD) and means the number of atoms per de-Broglie volume. The PSD shows how BEC can be achieved experimentally - by lowering temperature and increasing atomic density. Equation 2.33 defines the condition for Bose-Einstein condensation in a harmonic trap. For free space and box potential [52]:

$$n\lambda_{dB}^3 = \zeta(3/2) \approx 2.6. \quad (2.34)$$

For comparison, the phase space density of a thermal atomic beam at room temperature is  $10^{-17}$ .

## 2.4.2 Interacting BEC in a trap

In a condensate interactions are usually reasonably strong – the interaction energy is much greater than the kinetic energy in the system and, thus, can not be neglected.

An interacting condensate in a trap can be described by a Schrödinger equation with an extra interaction term. This is known as Gross-Pitaevskii equation [53]:

$$\left( -\frac{\hbar^2 \nabla^2}{2m} + V_{trap}(r) + g |\Phi(r)|^2 \right) \phi(r) = \mu \phi(r), \quad (2.35)$$

where  $g$  is a coupling constant that defines the interaction and is connected with the s-wave scattering length  $a$  via

$$g = \frac{4\pi\hbar^2 a}{m}. \quad (2.36)$$

In the Thomas-Fermi approximation, the kinetic energy term can be neglected since the interaction energy dominates

$$(V_{trap}(r) + g |\Phi(r)|^2)\phi(r) = \mu\phi(r), \quad (2.37)$$

which gives for  $|\Phi(r)|^2$ :

$$|\Phi(r)|^2 = \frac{\mu - V_{trap}(r)}{g}. \quad (2.38)$$

Since  $N |\Phi(r)|^2 = n(r)$  is the density for a cylindrically symmetric harmonic potential

$$V_{trap}(x, y, z) = \frac{1}{2}m(\omega_{\perp}^2 x^2 + \omega_{\perp}^2 y^2 + \omega_{\parallel}^2 z^2) \quad (2.39)$$

the density distribution in a trapped BEC is

$$n(r) = n_0 \left[ 1 - \left( \left( \frac{x}{R_{\perp}} \right)^2 + \left( \frac{y}{R_{\perp}} \right)^2 + \left( \frac{z}{R_{\parallel}} \right)^2 \right) \right], \quad (2.40)$$

where  $n_0 = \mu/g$  is the density in the center of the condensate, and the size of the condensate is given by Thomas-Fermi radii:

$$\begin{aligned} R_{\perp} &= \sqrt{\frac{2\mu}{m\omega_{\perp}^2}}, \\ R_{\parallel} &= \sqrt{\frac{2\mu}{m\omega_{\parallel}^2}}. \end{aligned} \quad (2.41)$$

The chemical potential  $\mu$  depends on number of particles and trap parameters as

$$\mu = \frac{\hbar\omega_{ho}}{2} \left( \frac{15Na}{a_{ho}} \right)^{2/5}, \quad (2.42)$$

where  $\omega_{ho} = (\omega_x\omega_y\omega_z)^{1/3}$  is geometric average of the oscillator frequencies and  $a_{ho} = (\hbar/m\omega_{ho})^{1/2}$  is the oscillator length.

A more detailed derivation can be found in [53].

After releasing from the trap, the BEC expands. This process can be described as a time-dependent change in Thomas-Fermi radii [54]:

$$\begin{aligned} R_{\perp}(t) &= R_{\perp} \sqrt{1 + (\omega_{\perp} t)^2} \\ R_{\parallel}(t) &= R_{\parallel} \frac{\omega_{\perp}}{\omega_{\parallel}} \left[ 1 + \frac{\omega_{\parallel}^2}{\omega_{\perp}^2} \left( \omega_{\perp} t \arctan(\omega_{\perp} t) - \log \sqrt{1 + (\omega_{\perp} t)^2} \right) \right], \end{aligned} \quad (2.43)$$

which is valid for the cylindrically symmetric case.

By understanding these density distributions, we can compare measurements from absorption images to extract information such as the temperature and number of atoms in our ultracold atomic clouds.

## 2.5 Imaging

To get information about the cloud, we use resonant absorption imaging. It is a destructive technique which uses light resonant with atomic transitions. The atomic cloud is released from a trap and after some time-of-flight (TOF), is illuminated with a resonant laser beam. Some part of this light is absorbed and is recorded on a CCD camera. As a result, each image looks like a bright background with a shadow that corresponds to the atomic cloud (Fig. 2.7a). For processing, two more images are taken: the laser beam without atoms (Fig. 2.7b), and the background when the imaging beam is off.

In the next processing step, the background is subtracted from the two other images. These background-free images are divided pixel by pixel and transformed in a new image (Fig. 2.7c) which is a 2D array of fractions

$$\frac{\text{CCD counts, with atoms}}{\text{CCD counts, no atoms}} \quad (2.44)$$

for each pixel. Since CCD counts  $\propto$  light intensity:

$$\frac{\text{CCD counts, with atoms}}{\text{CCD counts, no atoms}} = \frac{I}{I_0}. \quad (2.45)$$

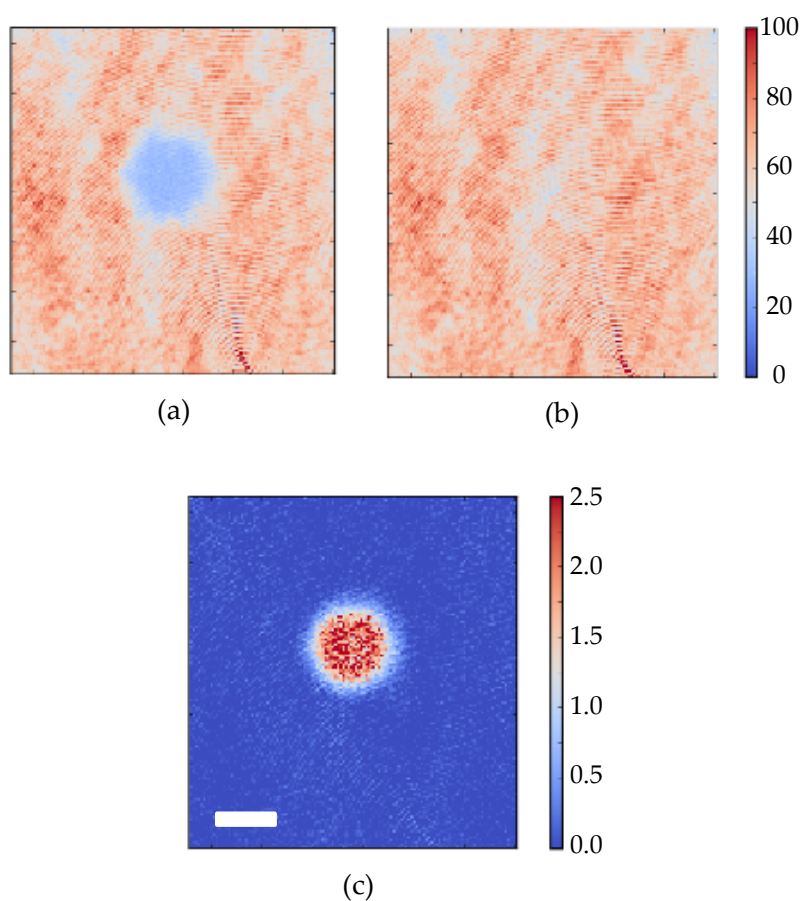


FIGURE 2.7: Example of raw (a,b) and processed (c) images for absorption imaging technique. Software compares images with atoms (a) and without (b). Difference is transformed into a new, processed image (c). White scale bare =  $360 \mu\text{m}$ . Color scale on (a) and (b) shows number of CCD counts, on (c) it shows optical depth.

For atomic cloud with thickness along the imaging direction  $z$  and density  $n$  Beer's law can be written as

$$I = I_0 \exp[-\sigma_{scs}nz], \quad (2.46)$$

where  $\sigma_{scs} = 3\lambda^2/2\pi$  is resonant scattering cross-section, where  $\lambda$  is the wavelength of the imaging light, which is chosen to be resonant with the atomic transition. From here, taking into account (2.45), for one pixel of area  $A_{pix}$  atom number is

$$N_{pix} = \frac{A_{pix}}{\sigma_{scs}} \ln \left[ \frac{\text{CCD counts, no atoms}}{\text{CCD counts, with atoms}} \right]. \quad (2.47)$$

Number of atoms in the cloud can be calculated as sum

$$N_{tot} = \sum_{pix} N_{pix}. \quad (2.48)$$

To measure the temperature of the cloud we can estimate its size and define how it changes with time. For thermal particles, described by a Boltzmann distribution, density is

$$n(\mathbf{r}) = \left( \frac{mk_B T}{2\pi\hbar^2} \right)^{3/2} \exp \left[ \frac{-V(\mathbf{r})}{k_B T} \right]. \quad (2.49)$$

Assuming a harmonic potential  $V(\mathbf{r}) = \frac{1}{2}m\omega^2\mathbf{r}^2$  and translating momentum to position for some time-of-flight  $t$  according to  $\mathbf{p} = m(\mathbf{r} - \mathbf{r}_0)/t$ , the time-dependent density distribution is:

$$n_{TOF}(\mathbf{r}) = \left( \frac{2\pi mk_B T}{h} \right)^{3/2} \frac{1}{1 + \omega^2 t^2} \exp \left[ \frac{-m\mathbf{r}^2}{2k_B T} \frac{\omega^2}{1 + \omega^2 t^2} \right], \quad (2.50)$$

where  $n_{TOF}$  is density distribution of thermal cloud at some time-of-flight  $t$ ,  $\omega$  is trap frequency.  $n_{TOF}$  is a Gaussian function<sup>5</sup> with width

$$\sigma = \sqrt{\frac{k_B T}{m}} \left( \frac{1 + \omega^2 t^2}{\omega^2} \right)^{1/2}. \quad (2.51)$$

---

<sup>5</sup>The function of the form  $\exp(-x^2/2\sigma^2)$

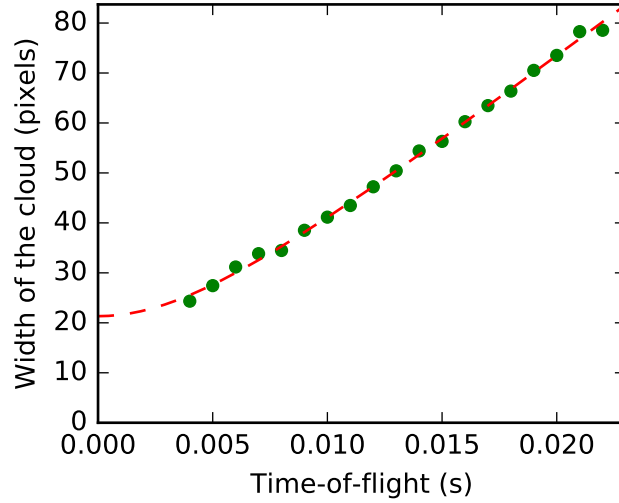


FIGURE 2.8: Example of temperature measurements. Width of the cloud is recorded for various expansion times (green dots). Fit to the data (dashed red line) shows  $v=3522$  pixel/s (pixel size is  $14.4 \mu\text{m}$ ), which corresponds to  $26 \mu\text{K}$ .

By equating the thermal and kinetic energies in the trap

$$\frac{1}{2}m\omega^2\sigma_0^2 = \frac{1}{2}k_B T = \frac{1}{2}mv^2 \quad (2.52)$$

where  $\sigma_0$  is width of the Gaussian fit for the cloud before releasing from the trap, Eq. (2.51) can be re-written

$$\sigma(t)^2 = \sigma_0^2 + v^2 t^2. \quad (2.53)$$

For temperature measurements, the density of the expanding cloud is fitted with a Gaussian which gives cloud's width. Such data is recorded for various times-of-flight and is fitted with Eq. (2.53) (Fig. 2.8). From the fit, velocity is extracted and temperature calculated using Eq. (2.52).

For long time-of-flight  $t \gg 1/\omega$ ,

$$\sigma \approx \sqrt{\frac{k_B T}{m}} t. \quad (2.54)$$

So, data from imaging is fitted with a 2D Gaussian, the atom number and temperature are extracted using above formulas.

Also, in addition to Eq. 1.48, the atom number can be extracted from the fit using

$$N = \frac{4\pi^2 A \sigma_x \sigma_z}{3\lambda^2}, \quad (2.55)$$

where  $A$  is height of the Gaussian,  $\sigma_x$  and  $\sigma_z$  are Gaussian width in two directions along image axis.

To measure BEC properties, we use the imaging system along the vertical direction. Thus, images contain column density along the  $Z$ -direction. The density distribution to fit such data can be extracted from Eq. (2.40) by integrating along imaging direction to find the 2D column density:

$$\tilde{n}(x, y) = \tilde{n}(0) \max \left( 1 - \frac{x^2}{R_{\perp}^2} - \frac{y^2}{R_{\parallel}^2}, 0 \right)^{3/2}, \quad (2.56)$$

where  $R_{\perp}$  and  $R_{\parallel}$  are the Thomas-Fermi radii, and  $\tilde{n}(0)$  is the integrated column condensate density in the center of the cloud. With known density distribution, the atom number can be calculated by integration

$$N = \int \tilde{n}(x, y) dx dy. \quad (2.57)$$

## Chapter 3

### BEC setup

In this chapter I will give the details of the setup that we built to generate a Bose-Einstein condensate (BEC) in an ensemble of  $^{87}\text{Rb}$  atoms. Our setup consists of three main blocks: a laser optics system, an ultrahigh vacuum (UHV) system where atom cooling and trapping are involved, and a control unit. The optics and UHV systems are on separate optical tables, each equipped with pneumatic legs for vibration reduction. In addition, the UHV system optical table stays on a base isolated from the rest of the building.

The laser optics system includes two 780 nm diode lasers, saturation spectroscopy and beat note wavelength lock systems, custom-made 4-to-6 and 4-to-4 fiber beam splitters, a 1064 fiber laser and all intermediate optics.

The UHV system consists of three parts: an atomic vapor source, a 2-Dimensional Magneto-Optical Trap (2D-MOT) and 3-Dimensional Magneto-Optical Trap (3D-MOT) located in what is referred to as the Science chamber.

Our computerized control unit allows us to control the whole experiment through digital and analog boards. The digital board has 26 outputs, each producing "0" and "1" level at 0 V and 3 V, respectively. For analog signals, we use three National Instrument Data Acquisition devices BNC2110. Each of them has eight outputs which can provide voltage ranging from -10 V to 10 V.

The whole setup is located in the same room including an air conditioning system which maintains the temperature and humidity at  $21 \pm 0.5$  °C and 30%, respectively.

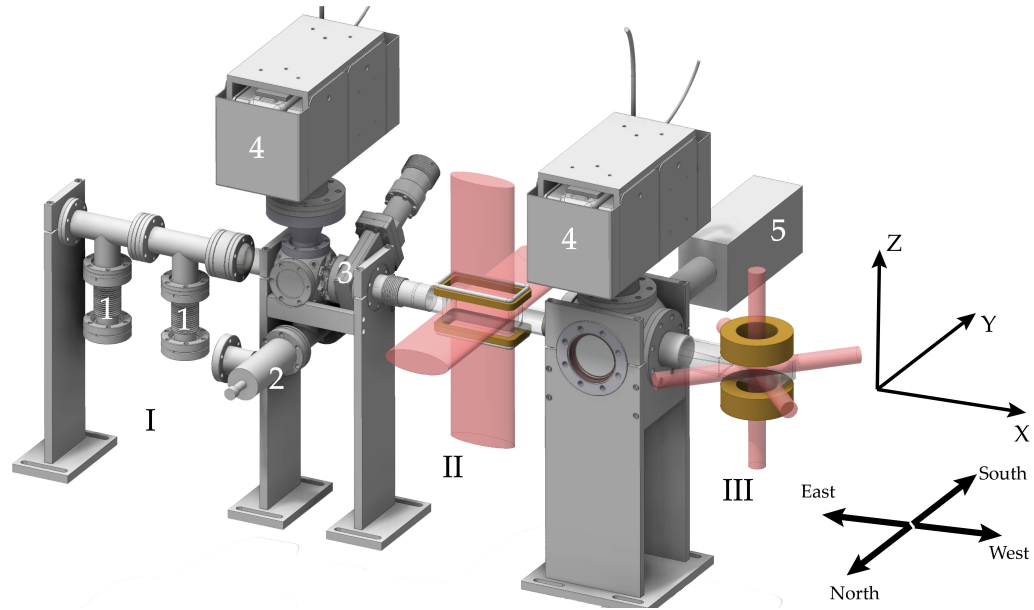


FIGURE 3.1: 3D model of our vacuum system with 2D- and 3D-MOT beams and coils. In addition, lab coordinate system and Cardinal directions are shown. I – Oven; II – 2D-MOT; III – 3D-MOT; 1 – flexible bellow with metal (Rubidium and Potassium); 2 – angle valve; 3 – gate valve; 4 – ion pump; 5 – residual gas analyzer. Image credit: Dr. Lindsay LeBlanc.

### 3.1 Ultrahigh vacuum system

Our UHV system is assembled on an optical table and consists of three main units - a source of Rubidium atoms vapor referred to as the oven, a 2D-MOT chamber, and a 3D-MOT chamber as shown in Fig. (3.1). The lab coordinate system is defined by the vacuum system location. Positive X corresponds to the direction in which atomic beam moves – "Oven→Science chamber". Positive Z corresponds to "Top→Bottom" direction. Positive Y is orthogonal to X and Z and forms with them the right-handed Cartesian coordinate system. In addition, for convenience to mark location of different parts and directions, we use the relative spatial location of the setup with respect to Cardinal directions.

### 3.1.1 Main parts of the vacuum system

For the vacuum system we use non-magnetic stainless steel parts. All home-made holders, adapters etc. are also made from non-magnetic materials - aluminum, brass, and plastic.

The oven chamber (Fig. 3.2) consists of a flexible bellows connected to spherical cold cup chamber from its East side. To this chamber are connected: an ion pump Agilent VacIon 55 Starcell from the top; an all metal angle valve with Agilent Turbo pumping system based on TwissTorr304FS and Ion gauge both through a "T"-piece from the bottom; cold cup from the South; glass window for cold cup condition monitoring from the North; gate valve MDC 302001 from the West.

We load Rubidium into our system in sealed glass ampoules. The ampoule is placed in the flexible bellows which can be bent to break the glass and release the metal. To break the sealing we use home-build aluminum holder and striking rod (Fig. 3.3). This holder keeps the ampoule at a suitable level for the rod to break the thin bottom glass part of the ampoule, releasing the Rb from vacuum inside the ampoule when the rod, which can move due to the bellows, strikes the ampoule. Also, the holder provides thermal conductance from the walls of vacuum chamber to the ampoule's Rubidium metal. The rod is hollow for easier degassing.

To evaporate Rb, we heat the flexible bellows and parts nearest to it to 80 °C. This creates relatively a high pressure of Rb vapors. To protect the rest of the system and keep good vacuum, a nozzle tube between flexible bellows and the spherical chamber is placed. It forms the initial beam of atoms that move towards 2D-MOT and science chamber, eventually to be trapped in 3D-MOT. At the same time the tube prevents atoms with velocities in other directions from escaping source region. Conductance of such tube can be calculated using

$$C = a \frac{v}{4} A$$

where  $v$  is the thermal velocity of the gas,  $A$  is the cross section area of the tube and  $a$  is a transition probability that an atom entering the pipe will leave the pipe on the other end [55]. For long tubes ( $l \gg d$ ) with round cross section,  $a = 4d/3l$ . The short tubes case is more complicated but  $a$  values are already calculated for different  $l/d$

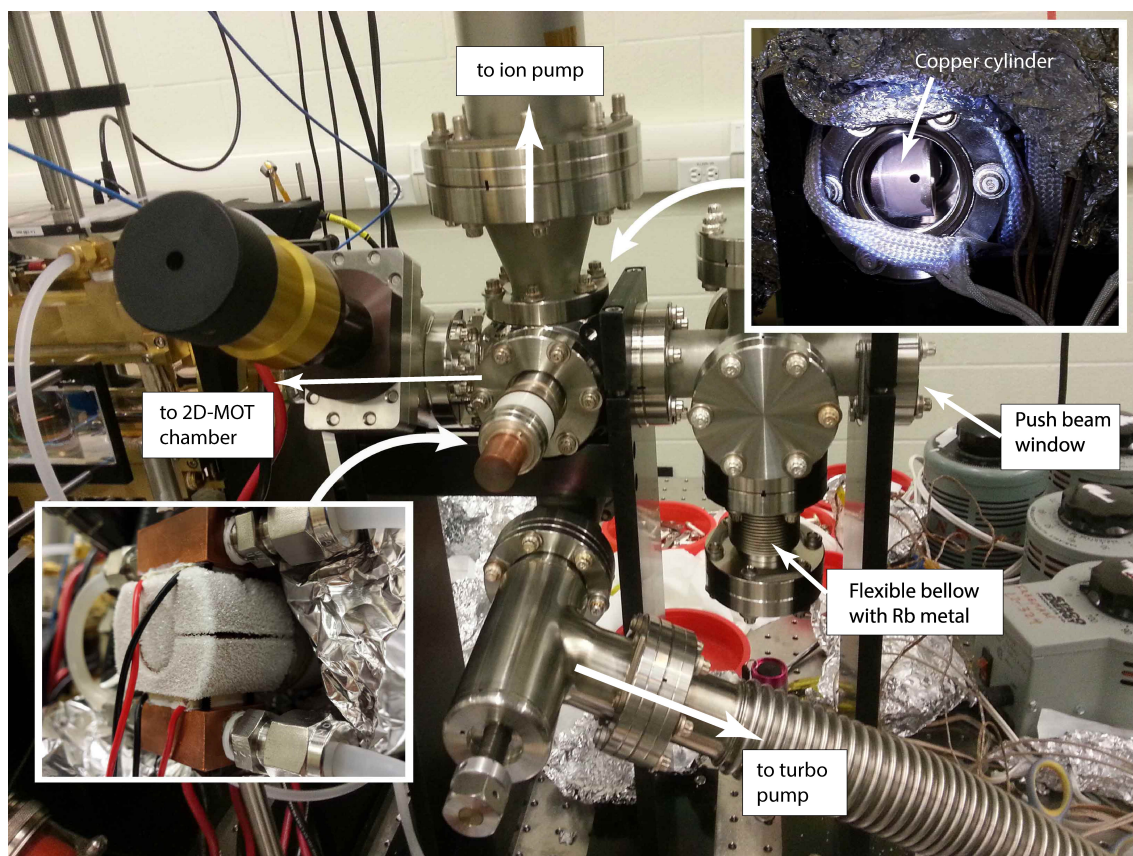


FIGURE 3.2: Rubidium atomic vapor source - Oven. On the main image cold cup is removed and copper feedthrough is visible. Assembled external part of cold cup (partially covered with ice) is shown on the left inset. Right insets shows window on the opposite side of the setup and internal part of the cold cup - copper cylinder.

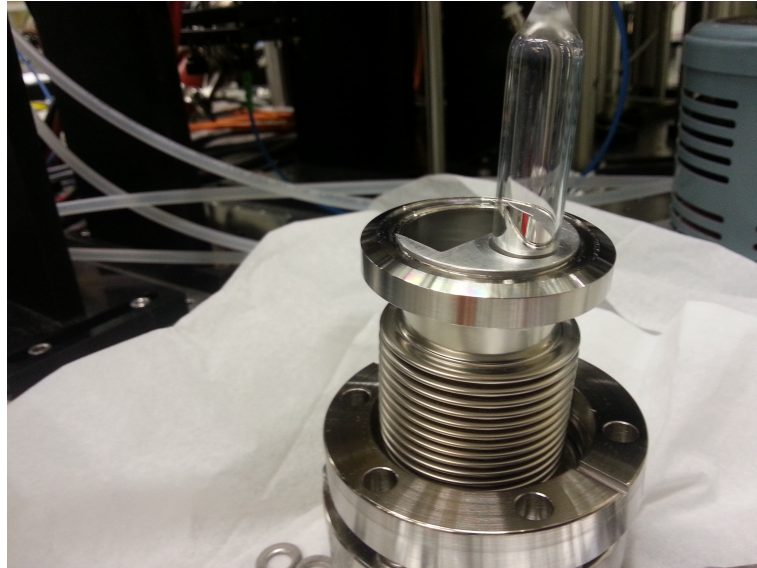


FIGURE 3.3: Flexible bellow and ampule with metallic Rubidium in the home built aluminum holder. Photo credit: Dr. Erhan Saglamyurek

ratios and are given in tables [e.g. [55]]. In our setup we use a tube with diameter 6.5 mm and length 47 mm which gives conductance around 1.77L/s. On the opposite side from the nozzle there is a window for the push beam. The push beam window and the nozzle are heated to 85°C and 90°C respectively.

Each region of the oven has a thermocouple connected and is wrapped with heater tape. Four temperature controllers Omega CN742 keep the temperature stable at the respective set points. While full metal parts can be heated relatively fast, the push beam window region must be heated slowly. Vacuum window specifications determine that thermal gradient should be lower than 25°C/minute. To be on the safe side we increase window's temperature much slower - around 1-2°C/minute.

The end of the nozzle opens inside the cold cup. The cold cup is a hollow cylinder made with copper and connected to one end of a 3/4" diameter copper electrical feedthrough MDC 9451001. The other end of feedthrough (outside the vacuum system) is cooled down with two 3A Peltier thermo-electric coolers that can create temperature difference between their surfaces up to 65°C. Their hot surfaces are cooled down with water(16°C). The main function of the cold cup is to protect the

ion pump from rubidium. Atoms that leave the atomic beam before it enters the 2D-MOT chamber stay in the oven spherical chamber and can be trapped with the ion pump, which causes pump contamination. The cold cup becomes the coldest part in the oven region and all background atoms stick to its surface. Since we do not want atoms and molecules trapped on cold cup surface atoms to be released, the coolers and their water cooling are on all the time. For this reason, we protect the coolers from overheating in case the water cooling is shut down for any reason. The thermocouple is connected to one of the hot surfaces and the temperature controller turns off the power supply that feeds the thermo-electric coolers if the temperature exceeds 20°C. In addition to the cold cup, we always keep the ion pump temperature at 100°C. To remove accumulated Rubidium from the Ion pump we increase its temperature during weekends to 150°C.

The gate valve separates the oven from the rest of the system. So, after metallic source replacement we need to bake only the oven region which is much easier than baking the whole setup. After the gate valve, the 2D-MOT and Science chambers are located. They are custom-made rectangular glass cells with dimensions:

1) 2D-MOT: height - 40 mm, width - 40 mm, length - 100 mm; walls thickness - 3 mm.

2) 3D-MOT/Science: height - 30 mm, width - 45 mm, length - 100 mm; walls thickness - 3 mm.

Between the 2D-MOT and Science chamber there is another spherical chamber. Here, the second ion pump is connected from the top, a titanium sublimation pump Gamma Vacuum 360547 from the bottom, and residual gas analyzer SRS RGA100 from the South. The science chamber is separated from the rest of the system with differential pumping tubes, which makes the pressure in the 3D-MOT spherical chamber two orders of magnitude lower than in the oven spherical chamber.

### 3.1.2 Cleaning and Bakeout

To achieve ultra high vacuum ( $10^{-9}$  Torr and lower), in addition to careful assembling of the vacuum system and pumping everything out, two additional procedures must be done. They are cleaning and baking.

| Component <sup>a</sup>                         | Max. bake temperature ( °C) | Notes   |
|--|-----------------------------|---|
| Ion pump<br>Agilent VacIon<br>Plus 55 Starcell | 350<br>250 (cable)          | Pumping speed for Nitrogen<br>50L/s.<br>Maximum starting pressure<br>$3.75 \times 10^{-2}$ Torr |
| Ion gauge<br>(SRS)NR-F-<br>UHV                 | 450                         | Operating pressure $2 \times 10^{-11}$ to<br>$10^{-3}$ Torr                                     |
| Gate valve<br>MDC 302001                       | 200 Open<br>150 Closed      | Operating pressure to $10^{-11}$ Torr   |
| Angle valve<br>ZCR40R                          | 450 Open<br>300 Closed      | Pressure range $0.75 \times 10^{-12}$ to<br>3000 Torr. Closure torque 7.7-<br>$12.7 N \cdot m$  |
| Copper<br>feedthrough<br>MDC 9451001           | 450                         | Vacuum range $10^{-10}$ Torr  |

TABLE 3.1: Vacuum parts specifications.

<sup>a</sup>Information about components was taken from their manuals.

Before assembling, all parts must be cleaned and dried. To clean vacuum components we use detergent at first. Then we wash off detergent with large amount of hot water. After that, we clean components with acetone, methanol and rinse with distilled water in the end. For any manipulation with vacuum pieces we use gloves - organic compounds are extremely hard to pump. Additional care should be given to knife edges where two separate pieces connect to each other. Scratches or other damages of the knife edge may cause future leaks.

Components are assembled with copper gaskets between them. We use gaskets covered with silver, so that components don't weld to each other under high temperatures. If the vacuum system is disassembled for some reason, the gaskets must be changed. They can not be reused. For assembling we use screws also covered with silver. Screws must be tightened by small portions one by one following clockwise or counterclockwise directions. This prevents skew.

When vacuum parts are assembled we run the turbo pump. If there is no leak in the system, the pump power drops as it pumps out and reaches 6 W. It can pump out the system to pressure around  $10^{-9}$  Torr. To remove water and other substances from the system, bakeout must be done. During this process we increase temperature of our vacuum setup, hold some time at high temperature and then cool it down. During this process one must be careful not to exceed maximum allowed temperatures for components (Table 3.1).

During preparation for bakeout we wrap heater tapes around all parts of the system and connect thermocouples to all components for temperature monitoring. After that, parts are covered with aluminum foil to keep temperature more stable. For glass-metal seals we use two thermocouples – one on the glass and one on the metal, to keep ensure the temperature difference between them is as low as possible. To bake glass cells, special frames were made around them and heater tapes were wrapped not directly on glass but around the frames. The frames were also covered with aluminum foil which created oven effect and reduces any temperature gradient, which is harmful for glass.

At the beginning of baking as temperature increases, pressure inside the system also increases – water and other compounds leave the surface of vacuum parts. As the turbo pump removes them, pressure drops. When the pressure is safe for ion pumps they are turned on. The pressure keep decreasing to some point and then remains the same, usually around  $10^{-8} - 10^{-9}$  Torr. From this point temperature is slowly decreased. We close the turbo pump valve and let the system cool down to room temperature.

After successful bakeout, pressure in the oven region reaches lower  $10^{-10}$  Torr and in the science chamber drops below  $10^{-11}$  Torr, which is out of measurable range so the ion pump controller and monitor shows "Low pressure".

## 3.2 Magnetic field control

To control the magnetic field inside the 2D- and 3D-MOT chambers during experiments, a few sets of coils and power supplies are used.

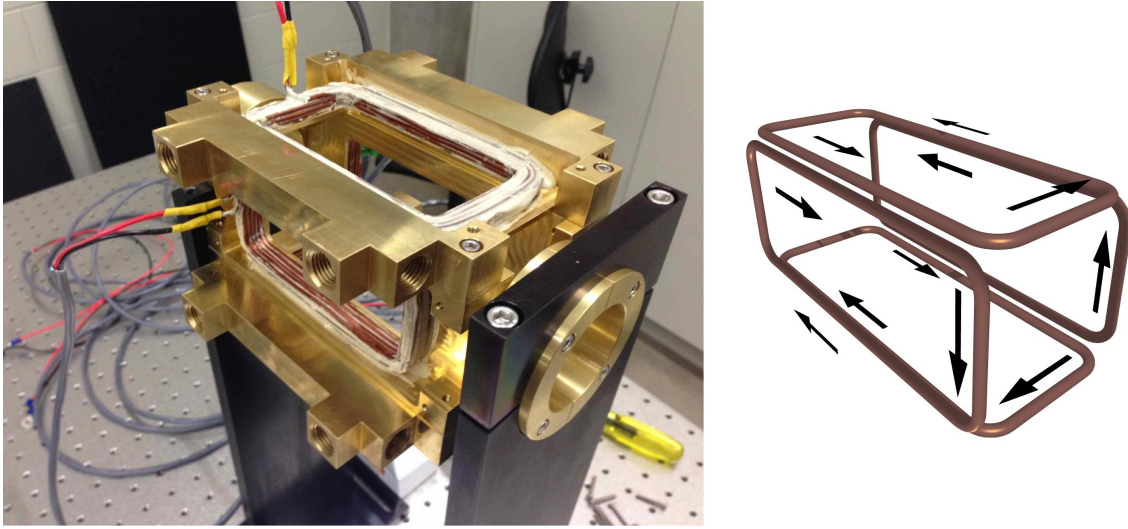


FIGURE 3.4: 2D-MOT coils assembled in home made brass holders(left). There are few threaded holes for water cooling connection. current direction. Right image shows 2D-MOT coils location in space. Arrows indicates current direction through each coil. Photo credit: Dr. Lindsay LeBlanc.

### 3.2.1 2D-MOT coils

The magnetic field for the 2D-MOT is formed by 4 rectangular coils. Each coil consists of 25 turns of 12 AWG wire 2.2 mm in diameter. Their resistances are given in the Table 3.2. For fixing coils in correct positions around the 2D-MOT glass chamber we use 4 home-built brass holders. They assemble together and create a cage around the cell (Fig. 3.4). Two holders are hollow inside and are connected to a water cooling loop. Water under pressure 30 psi and temperature 16°C circulates through them. To keep them at the appropriate height two home-built aluminum holders are used. Also, the 2D-MOT optics are attached to the brass holders.

To feed the 2D-MOT coils, two Agilent 6651A DC power supplies are used. Each of them can provide current up to 50A (0-8V) which is enough for two coils. Current from each power supply is split for two coils (Fig. 3.5). To have individual control on the current through each coil we use transistors. Two MOSFETs IXFN180N25T that

| Coil   | Resistance, Ohm |
|--------|-----------------|
| Top    | 0.031           |
| Bottom | 0.031           |
| North  | 0.033           |
| South  | 0.037           |

TABLE 3.2: 2D-MOT coil resistance.

can handle continuous drain current up to 168A each are used for one coil. Gate voltage control is carried by computer through National Instruments BNC2110. Transistors are mounted on a water cooled aluminum plate to prevent their overheating. The coils are connected in a way that current through each of them runs in the direction shown in Fig. 3.4. This creates a magnetic field gradient with zero field on the long axis of the coils.

### 3.2.2 3D-MOT/MT coils

The main 3D-MOT coils are used at different stages of the experiment - 3D-MOT, Magnetic trapping and Feshbach resonances (in future experiments). Some of them requires a high magnetic field gradient that is achieved by running high current (more than 400A) through the coils. This defines their technical features. The coils are made with Kapton insulated hollow copper wire. It has square cross section with side  $3/16''$  or 4.8 mm. Since, during the experiment high current is used, cooling water is circulated through the hollow cavity inside the wire (round cross-section,  $3/32''$  or 2.4 mm). This protects the coils and their environment from overheating and minimizes coils resistance fluctuations. To increase cooling efficiency, a booster pump Berkeley MGP7D-02 was added to the 3D-MOT coil's water cooling loop. The pump increases water pressure from 30 psi to 220 psi. It maintains the coil's temperature lower than  $35^{\circ}\text{C}$  at all stages of the experiment. To be sure that high current will not be run if the booster pump is off, we added an interlock based on flow meters Proteus 0100C110 into the water cooling loop. If water pressure is low, the signal

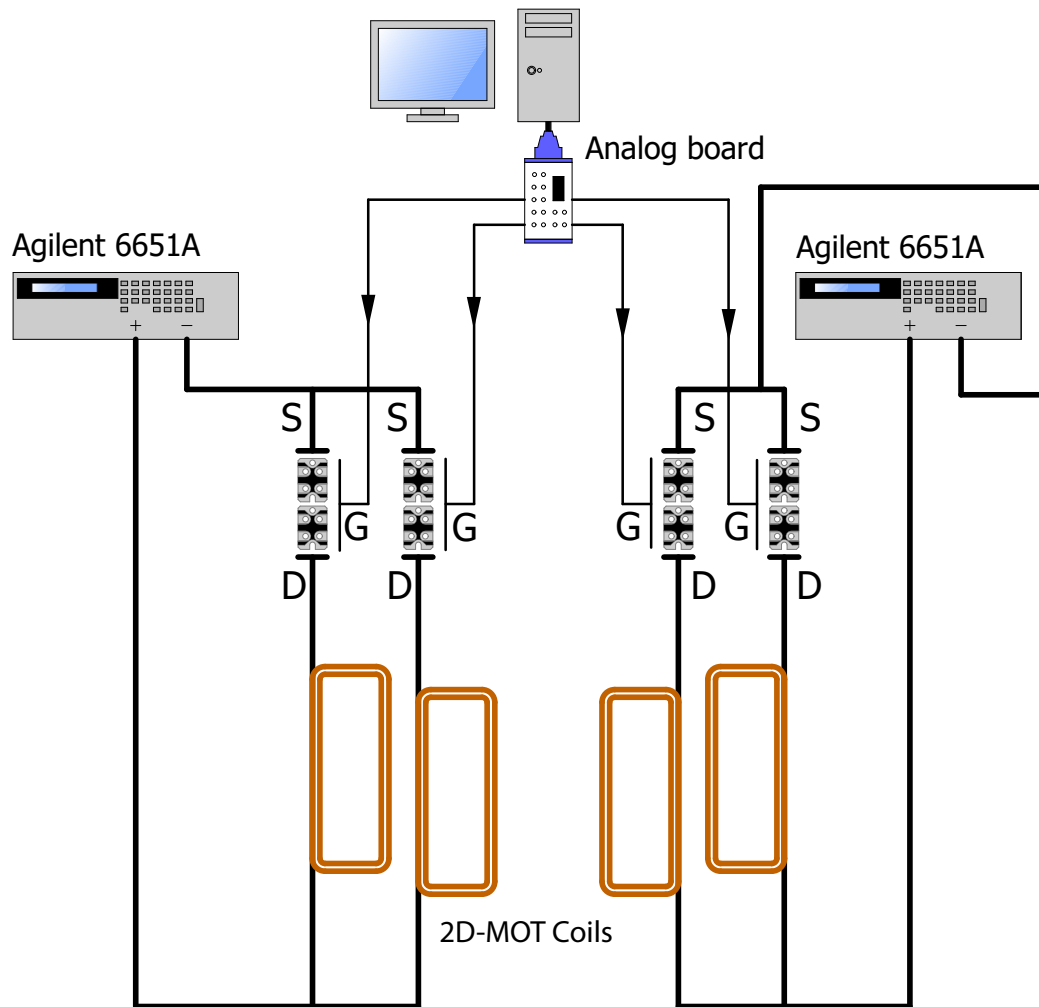


FIGURE 3.5: 2D-MOT coils current control scheme. Transistor terminals are labeled: S: source, G: gate, D: drain

from the flow meters does not close the protection loop of the power supply and it will not start until the booster pump is on.

Each coil consists of 24 turns in configuration  $4 \times 6$  (4 layers 6 turns in each)(Fig. 3.6). The separation between coils is equal to 58 mm and is defined by the glass cell height. Since the distance between coils has some limits, the desired field configuration is achieved by varying the coil's diameter. Inner diameter 130 mm was chosen

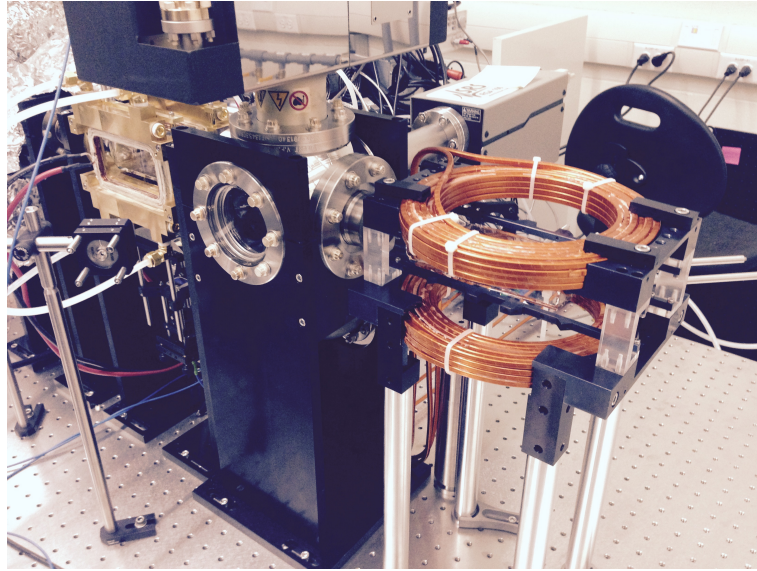


FIGURE 3.6: 3D-MOT coils mounted in their holders around Science chamber. Photo credit: Dr. Lindsay LeBlanc.

because it gives the lowest field curvature<sup>1</sup> for the separation 58 mm. The resistance of one coil is  $0.012 \Omega$ . For the connection between the coils and power supply, 4/0 AWG wires with nominal overall diameter 19.05 mm are used. Together with these wires, the resistance of the coil pair is  $0.033 \Omega$ . The coils provide  $0.197 \text{ G/cmA}$  and  $0.42 \text{ G/cmA}$  field gradients in radial and vertical directions respectively. For these 3D-MOT coils we use an Agilent 6690A DC Power Supply. It can provide 440A current and up to 15V. To control the coil current, a bank of transistors is used. 24 MOSFETs<sup>2</sup> IXFN180N25T are mounted on a water cooled plate in 4 rows - 6 transistors in each (Fig. 3.7).

On the bottom surface of the MOSFETs we apply thermal paste for better thermal conductance between each transistor and the cold plate. The source outputs of all transistors connected together and to the positive output of the power supply. All drain outputs are also connected together and to the first coil input. The first coil is connected to second one in the way that current in them runs in opposite directions

<sup>1</sup>Field curvature is important for future experiments with Feshbach resonances in potassium when coils will work in Helmholtz configuration

<sup>2</sup>Metal-Oxide Semiconductor Field-Effect Transistor

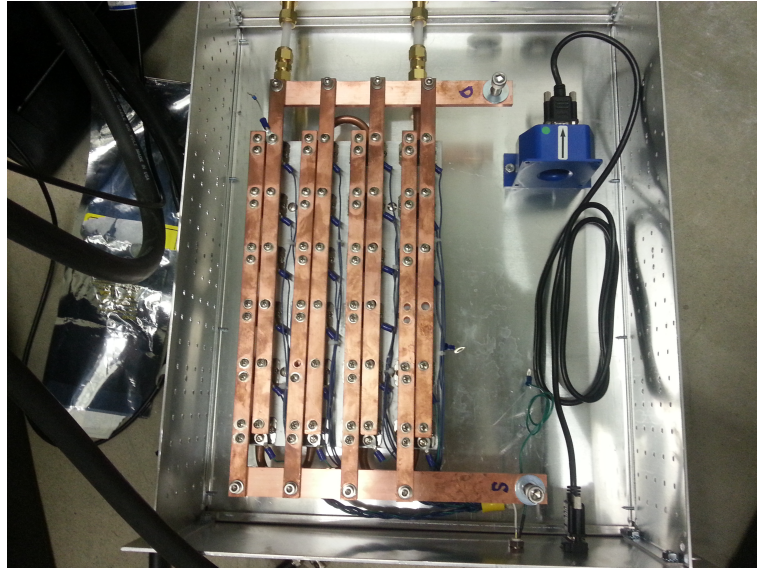


FIGURE 3.7: MOSFETS bank. Photo credit: Dr. Erhan Saglamyurek.

– anti-Helmholtz configuration. This creates a 3D magnetic field gradient with zero field in the center of coil pair. The second coil is directly connected to the positive output of the power supply. The gates of all transistors are also connected together and are controlled from current stabilizer. So, all 24 MOSFETs are connected in parallel and work like one big transistor.

Agilent 6690A has two options for voltage control. It can be set manually and will always remain the same or it can be dynamically changed during an experiment. If the voltage is set manually, it must be high enough to support the highest current that is used during experiment. For example, in our case maximal current in experiment is 420 A. Load resistance is  $0.033\Omega$  so we can estimate that 14 V should be enough. But beside the step with 420 A, we have a few steps where current is not as high. In that case only the voltage necessary to provide desired current through the coils drops at the load. The rest of it drops across the transistors, which causes their heating and damage despite the water cooling. After switching to dynamic voltage control we experienced some grounding problems, where the power supply jumped into "Protection mode" every time we tried to change voltage. Including Analog Devices AD210BN Isolation Amplifier into the voltage control circuit has solved the

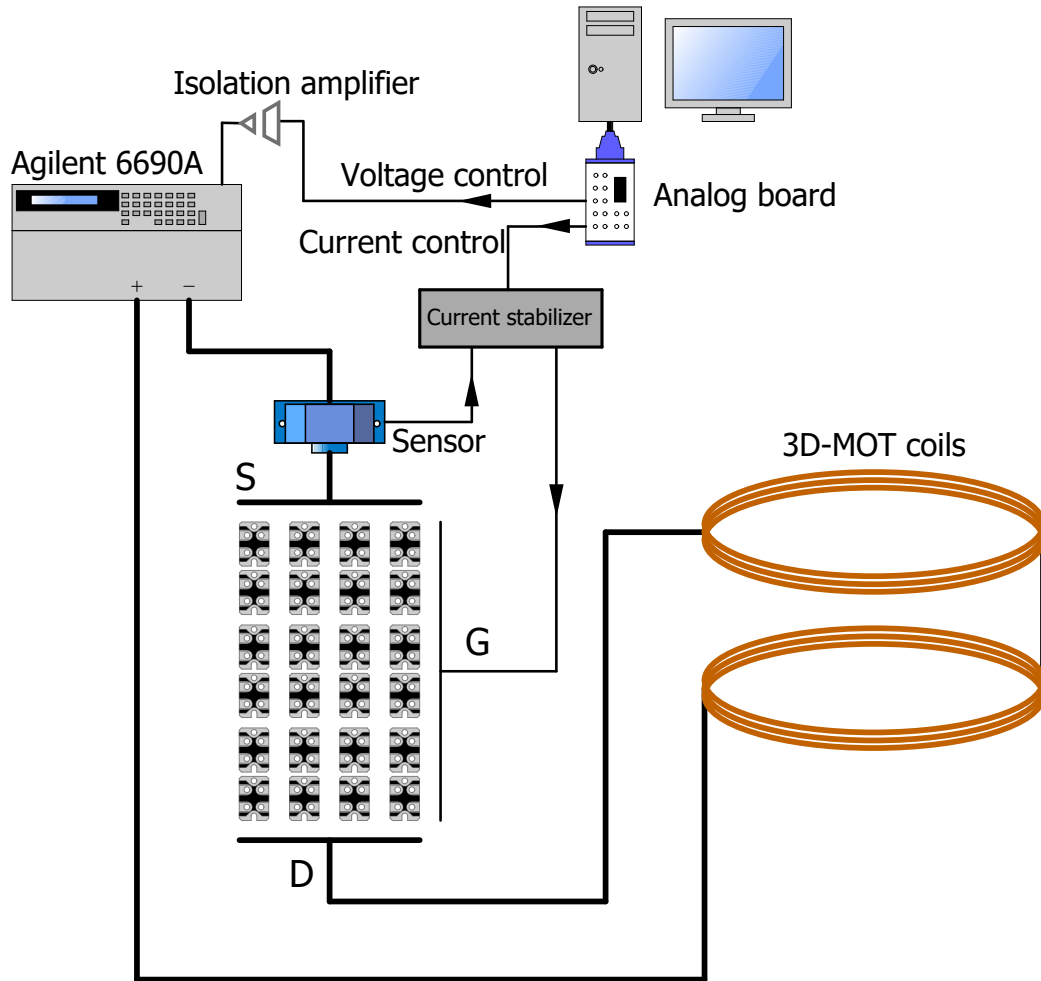


FIGURE 3.8: 3D-MOT/MT current control scheme. Transistor terminals are labeled: S: source, G: gate, D: drain

problem. Important here is that the power supply works in the way that it adds the manually set voltage and dynamically controlled voltage. So, one should keep the manually set value equal to zero. The current control is carried out with computer through the current stabilizer (Fig. 3.8) - a home built feedback board (more details in [56]). The DAQ is connected to input of the board and provides a signal corresponding to the desired current. Current sensor Danfysik Ultrastab 867-400 at

the source wire provides a signal that corresponds to actual current in the coil circle. The feedback box evaluates the difference between signals and adjusts the gate voltage that controls transistors current. Including the feedback stabilizer into the current control system causes some delay in the current's rising and falling time.

### 3.2.3 Bias coils

To make the 3D-MOT efficient, the geometric laser crossing point has to match the magnetic field center. It is fairly difficult to find that point with six 3D-MOT beams aligned to each other. It is easier to move the magnetic field center. Also, for loading the atomic cloud from optical molasses into the magnetic trap, matching their centers is important. The magnetic trap must be created at the same point where atoms are. If the magnetic trap is shifted with respect to the molasses, the cloud will be caught at the edge of the trap and will fall to its center. The resulting sloshing will cause atom heating and losses.

The 3D-MOT coils are fixed in their positions. Hence, their field center is fixed too. Therefore, to move the magnetic field center we need an additional field. These fields also can be used to cancel external magnetic fields (including Earth's magnetic field) and to create the necessary fields for optical pumping and imaging.

To have full spatial control, we set up 6 bias coils - a pair in each of the 3 orthogonal directions. In each pair, current runs through both coils in the same direction. We tried to be as close to the Helmholtz configuration as possible to create a nearly uniform magnetic field along the coil axis. But the bias-coils are mounted around the science chamber and their geometry is restricted by the glass cell, 3D-MOT coils, cage system and desired optical access to Science chamber. Our final configuration (Fig. 3.9) is:

1. X-axis coils consist of 4 layers and 4 turns in each. Coil's inner radius is 50 mm. Separation between coils 210 mm. Field at the center is 0.31 G/A
2. Y-axis coils consist of 1 layer and 4 turns in it. Coil's radius is 47.5 mm Separation between coils ...Field at the center is 0.61 G/A
3. Z-axis coils consist of 4 layers and 1 turn in each. Coil's radius is 66 mm Separation between coils 58 mm. Field at the center is 0.59 G/A

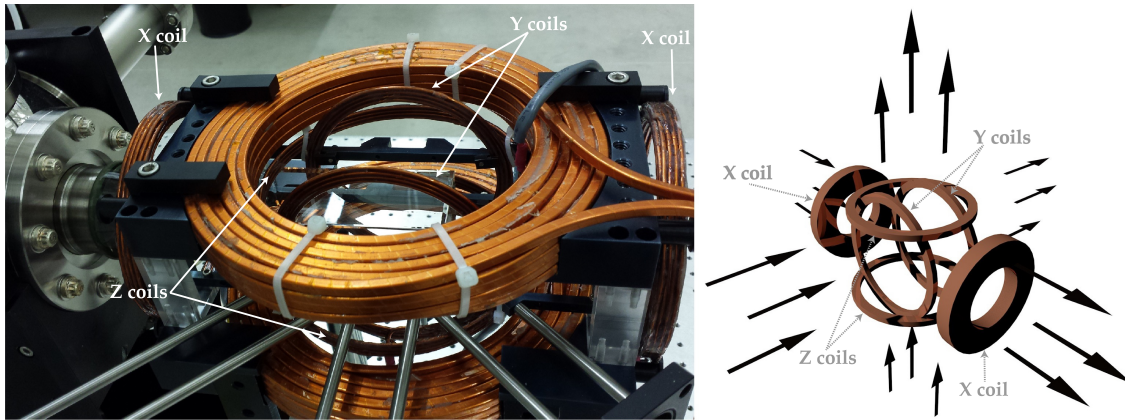


FIGURE 3.9: Bias coils together with 3D-MOT/MT mounted on the cage around glass cell(left). Right image shows bias coils location in space, big 3D-MOT coils are not shown. Arrows indicates magnetic field direction for each pair of coils if positive voltage is applied from power supplies.

For the bias coils we use 12 AWG copper wire. Each coil pair is powered by a KEPCO BOP 20-20M power supply that can provide  $\pm 20$  A and  $\pm 20$  V. These power supplies are bipolar which gives us possibility to change not only magnetic field magnitude but also its direction. Each power supply in addition to manual control has a channel for remote (in our case computer) control. Initially, the power supplies worked in the constant current regime. However, we noticed current oscillation in the bias coils circuits when the 3D-MOT coils current was on. After switching to the constant voltage regime, the oscillations have gone.

### 3.2.4 Radio frequency circuit

In rubidium, the energetic separations between levels split due to the Zeeman effect are in the radio frequency range. To have control over transitions between those levels, we implemented into our setup a radio frequency circuit (Fig. 3.10).

A digital RF radiation source Novatech Direct Digital Synthesized Signal Generator 409B is used. It has 2 programmable outputs in the range from 0.1 Hz to 171 MHz with 0.1 Hz step size. The output power of this device is 2.5 mW per channel. The Ophir 5303055 linear power RF 25 W amplifier increases the power of the signal.

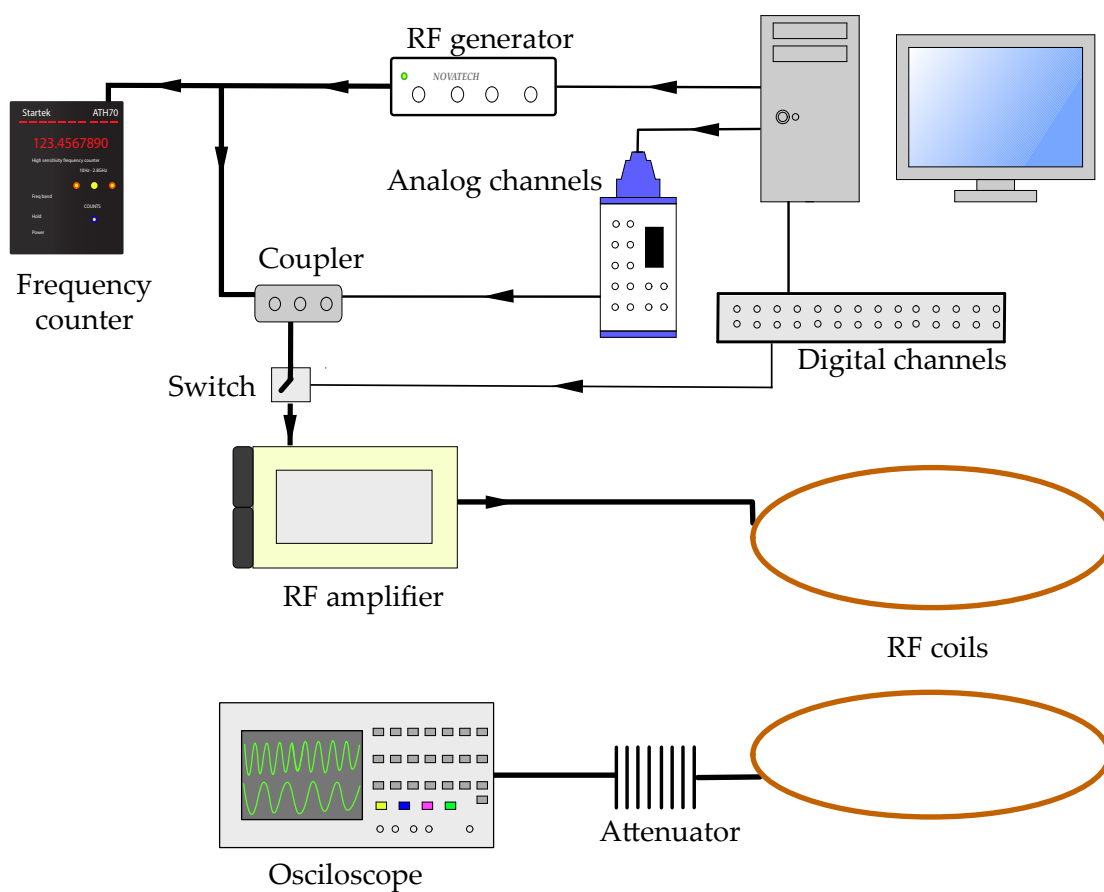


FIGURE 3.10: Radio-frequency circuit

After the signal generator frequency is monitored by a frequency counter, Startech ATH70. It is possible to change signal strength from the signal generator directly, but to avoid delays and leaks (which due to the amplifier may affect the experiment significantly), a fast rf switch Mini-Circuit ZYSWA-2-50DR and coupler Mini-Circuit ZAD-6+ were added in the circuit before the amplifier. When the switch is turned off signal goes to 50  $\Omega$  terminator. The amplified signal is sent through a coaxial cable to 2 coils.

Each RF coil is a single turn of 12 AWG wire with radius 30 mm, and separation between them is 40 mm. Both coils carry current in the same direction. After these coils, the signal is monitored by an oscilloscope, which is protected with a Mini-Circuits BW-S30W20+ 30dB attenuator.

### 3.2.5 Pneumatic mirror mounts

After the optical molasses stage, there is no more need for the MOT beams to access the science chamber. Given this, we can move the 3D-MOT mirrors away to open optical access for other beams that we need during later stages of the experiment – for the top-bottom imaging beam, 2 optical dipole trap beams, 2 Raman beams or 2 quantum memory beams. For this purpose we use pneumatically actuated optical mounts described in [57]. There are two types of mounts – horizontal and vertical. Horizontal mounts (Fig. 3.11) are based on: commercially available pneumatic cylinder SMC NCMR106-0200CS, linear guide rail IKO Nippon Thompson LWLF14R150BPS2 and carriage system IKO Nippon Thompson LWLF14C1BPS2; and a custom-made monolithic base plate, translating optic holder, and return flag. Vertical mounts (Fig. 3.12) are based on pneumatic cylinder SMC NCMKB088-150CS and a custom-made lower cylinder, upper cylinder, kinematic bearing plate, and optic rod. For both types the same standard three point kinematic stops are used. Each of them includes three distinct pieces: a cone (Hitek Hardware KC-1032-TH), a flat (Hitek Hardware KF-1032-TH), and a V-cut groove (Hitek Hardware KS-1032-TH).

In our initial implementation, we experienced alignment drifts and jumps caused by the vertical mounts. Moreover, instabilities were caused by all 4 mounts that we use. A possible reason might be that the vertical mount pneumatic piston's rod, kinematic bearing plate and optic rod were connected rigidly. That is why kinematic

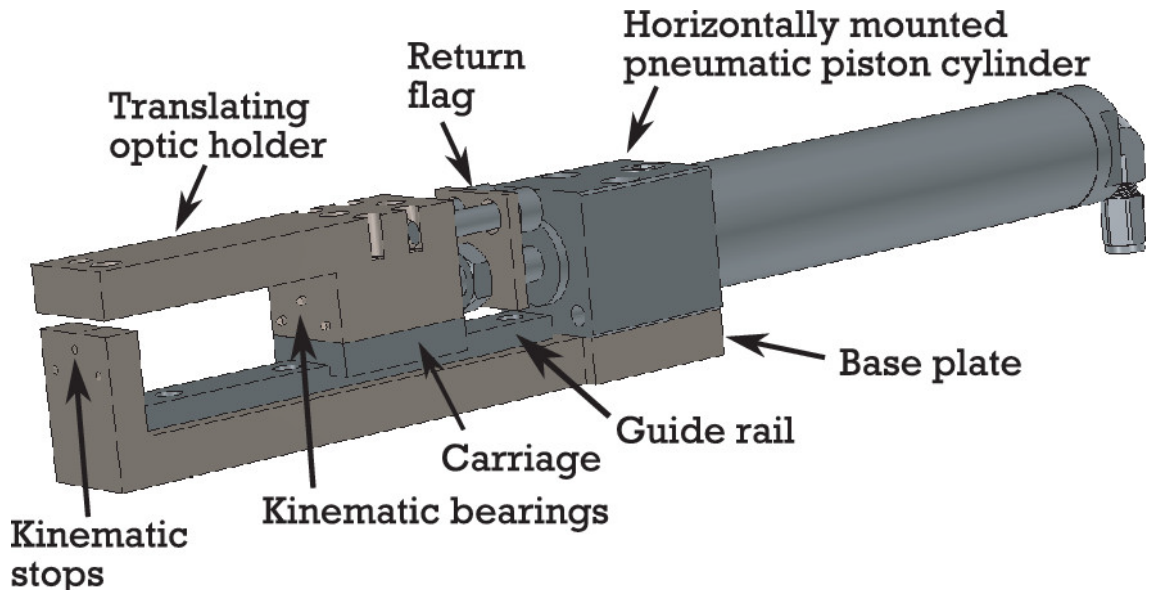


FIGURE 3.11: Horizontal pneumatic mirror mounts [57].

stops can not do their job: they can not shift the kinematic bearing plate because it is connected to the pneumatic piston. The vertical mount will work properly only if the kinematic bearing plate is perfectly aligned with the kinematic stops - if no adjustment is needed from them. But to succeed in such alignment is very difficult. That is why we made one change in vertical pneumatic mount construction. To break the rigid connection, we inserted a helical flexible shaft coupler between the pneumatic piston's rod and kinematic bearing plate. In the horizontal mounts pneumatic piston's rod and carriage are not connected rigidly. They work perfectly without any changes.

Also important is the amount of time during which mirrors go up or down. While they extend quickly  $<1$  s, retraction takes more than 2 s. To be sure that mirrors are completely removed and optical path is clear we start retraction 3 s in advance.

### 3.3 Lasers and Optics

Our BEC production apparatus includes 3 lasers: Repump, Cooling, and Trapping. The Repump laser is locked via saturated spectroscopy 80 MHz below the Rb  $D2$

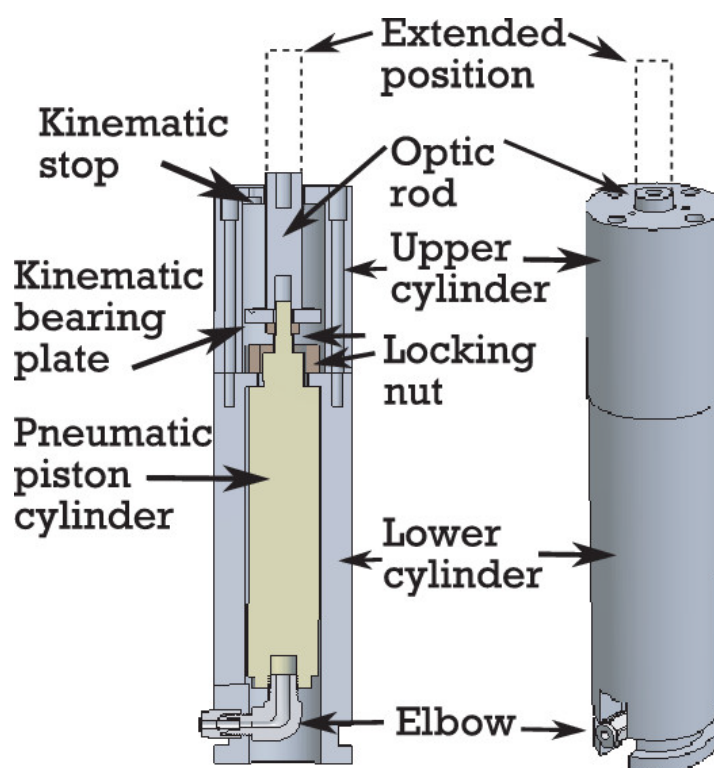


FIGURE 3.12: Vertical pneumatic mirror mounts [57].

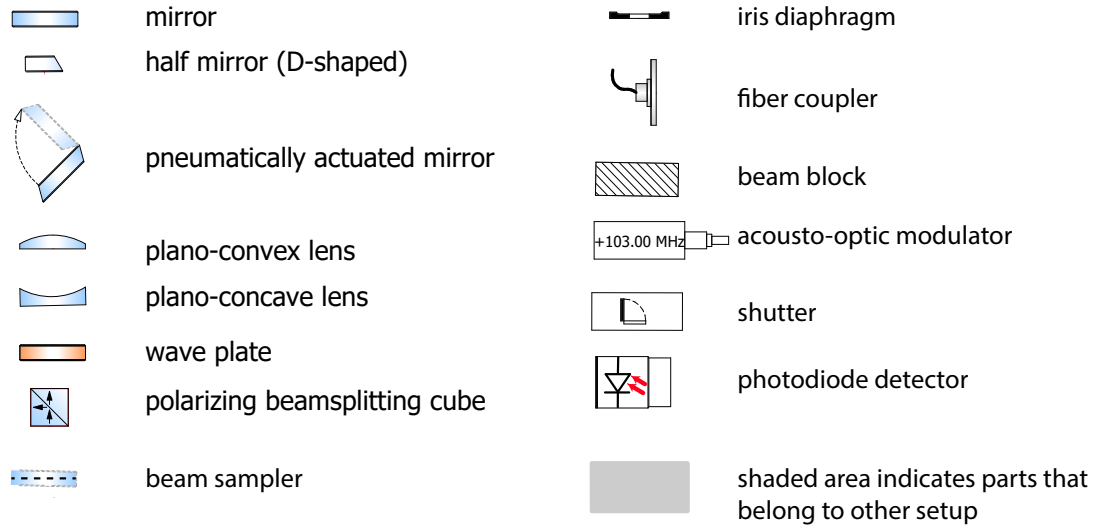


FIGURE 3.13: Legend for optical components. It is applicable to all optical schemes presented in this thesis.

transition  $F = 1 \rightarrow F' = 2$  (Fig. 4.1), which corresponds to wavelength 780.231 nm. The Cooling laser is locked 6.7 GHz above the Repump laser transition using a beat note technique. Its frequency is 160 MHz red detuned from the Rb  $D2$  transition  $F = 2 \rightarrow F' = 3$  (Fig. 4.1). The Trapping laser operates at 1064 nm far off-resonance and is used to create an optical dipole trap.

### 3.3.1 Repump laser

To pump atoms from  $F=1$  level to  $F=2$  level  $F = 1 \rightarrow F' = 2$ , a repump transition is used. For the repump laser, we use Toptica DL100 - a narrow linewidth highly coherent diode laser with output power 110 mW. The repump laser's optical setup is shown on the Fig. 3.13, 3.14.

The repump laser is locked directly to the Rb atomic transition using Doppler-free saturated absorption spectroscopy [36]. For that purpose, a small portion of the light (3.3 mW) is picked off from the main beam and is split into 2 beams: the first one (1.1 mW) is split again into two – probe (0.02 mW) and pump (1.08 mW)

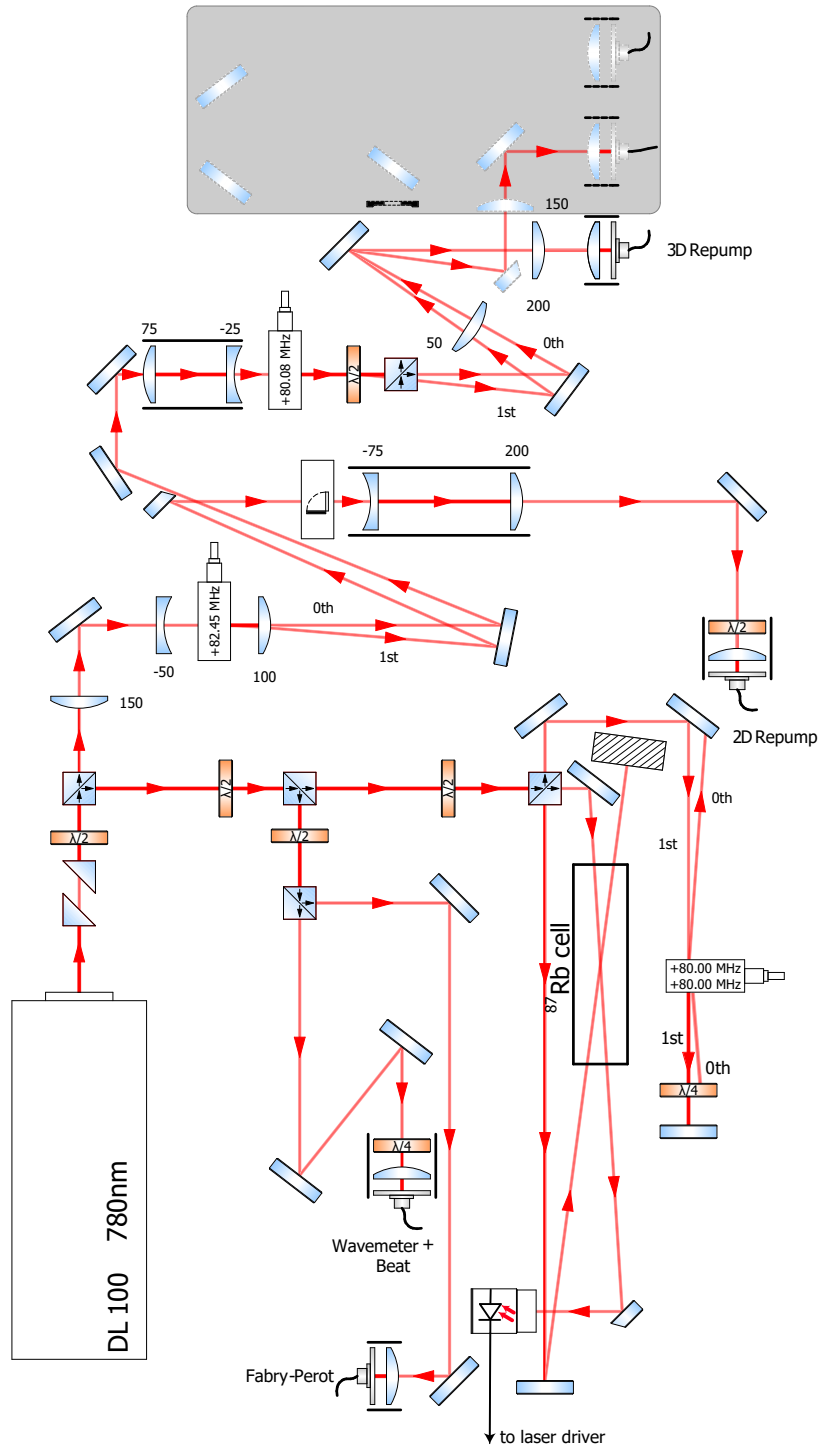


FIGURE 3.14: Cooling laser's optical setup. For legend see Fig. 3.13.

for saturated spectroscopy; the second one (2.2 mW) is also split again: 0.1 mW is used for laser's mode monitoring and goes to the Thorlabs Scanning Fabry-Perot Interferometer SA200-5B which is connected to an oscilloscope. 2.1 mW is coupled to one of a fiber beam splitter's inputs and is used for beat note locking of the cooling laser (described below).

For saturated absorption spectroscopy, two beams are used - which we call the probe and the pump. The probe goes through Thorlabs GC25075-RB Rubidium Reference Cell to the photo-diode detector. Inside the cell, the pump beam propagates in opposite to the Probe direction and crosses it. Before the cell Pump beam goes through a double-pass AOM that shifts the frequency by  $+80 \text{ MHz} \times 2 = +160 \text{ MHz}$ <sup>3</sup>. The frequency of the double pass AOM can be dynamically changed during the experiment and it will not cause power changes in the beam or misalignment. It is important in our case since the saturation spectroscopy AOM is modulated at a frequency of 48 kHz to obtain an error signal. Toptica Digilock software provides analysis of the signal from the photo detector and based on it makes adjustments to the laser's wavelength.

If the probe beam is 160 MHz shifted with respect to the saturation spectroscopy laser, it will be locked to a frequency  $160 \text{ MHz}/2 = 80 \text{ MHz}$  below resonance. So, we use AOMs to compensate this detuning and bring the 2D- and 3D-MOT repump beams to resonance. This AOM also gives us control over the power in the beams.

The main beam from the repump laser is split by the "2D-repump" AOM into two beams. The first order diffraction from the AOM (50 mW) with an +80 MHz shift is in resonance with  $F = 1 \rightarrow F' = 2$  transition and is used as repump for the 2D-MOT. It goes to a "4 to 4" fiber beam splitter (Fig. 3.15). The zeroth order diffraction (50 mW) is still red detuned, and to be resonant goes through another AOM - "3D-repump". After it, first-order diffraction goes to "4 to 6" fiber beam splitter (Fig. 3.16) and is used as repump for the 3D-MOT.

---

<sup>3</sup>Since AOM can be aligned in two ways – to increase or to reduce light frequency - here and next "+" means AOM increases light frequency by stated value; "-" means AOM decreases light frequency by stated value

### "4 to 4" and "4 to 6" fiber beam splitters

Both beam splitters (Fig. 3.15 and Fig. 3.16) are designed to support present Rubidium and future Potassium experiments.

Each fiber beam splitter has 2 inputs for Rb repump and cooling light and 2 inputs for K repump and cooling. From each input 0.5 % of optical power is separated for monitoring into separate fiber outputs. So, we are able to monitor continuously repump and cooling light for 2D- and 3D- MOTs. In the 2D-MOT splitter, cooling light is divided equally between 4 outputs and in 3D-MOT splitter - between 6 outputs. In both splitters, the repump is divided into two parts which are mixed with cooling light.

The fiber outputs from the splitters go to the vacuum system and form MOT beams. For the 2D-MOT, the output fibers are sent into the beams labelled Top, Bottom, North and South beams; where the two last contain repump light. For the 3D-MOT, the output fibers are sent into the beams labelled Top, Bottom, North-East, South -West, North -West and South-East; the two last contain repump light. Before entering the glass cell, each initially linearly polarized beam goes through a quarter-waveplate to become circularly polarized, and through a lens to collimate the fiber output. With lenses, in addition to collimation, we change the size and shape. The 3D-MOT beams have a round cross section with diameter 2 cm, and the 2D-MOT - beams have an elliptical cross section with diameters 6 cm (in X direction) and 2 cm in the y-direction.

### 3.3.2 Cooling laser

In our cooling scheme we use  $F = 2 \rightarrow F' = 3$  as the cooling transition. As the cooling laser, we use Toptica TAPro, a narrow linewidth high coherent diode laser, internally amplified by a tapered amplifier. The laser has 2 apertures - one for the seed beam and one for the main amplified beam. The seed output provides 18 mW and main output - 1.6 W.

The seed beam is split into 2. One is used for monitoring the laser mode in the Fabry-Perot cavity. Another one is coupled to the second input of the same fiber beam splitter that is used for repump (described above). So, at the both outputs of

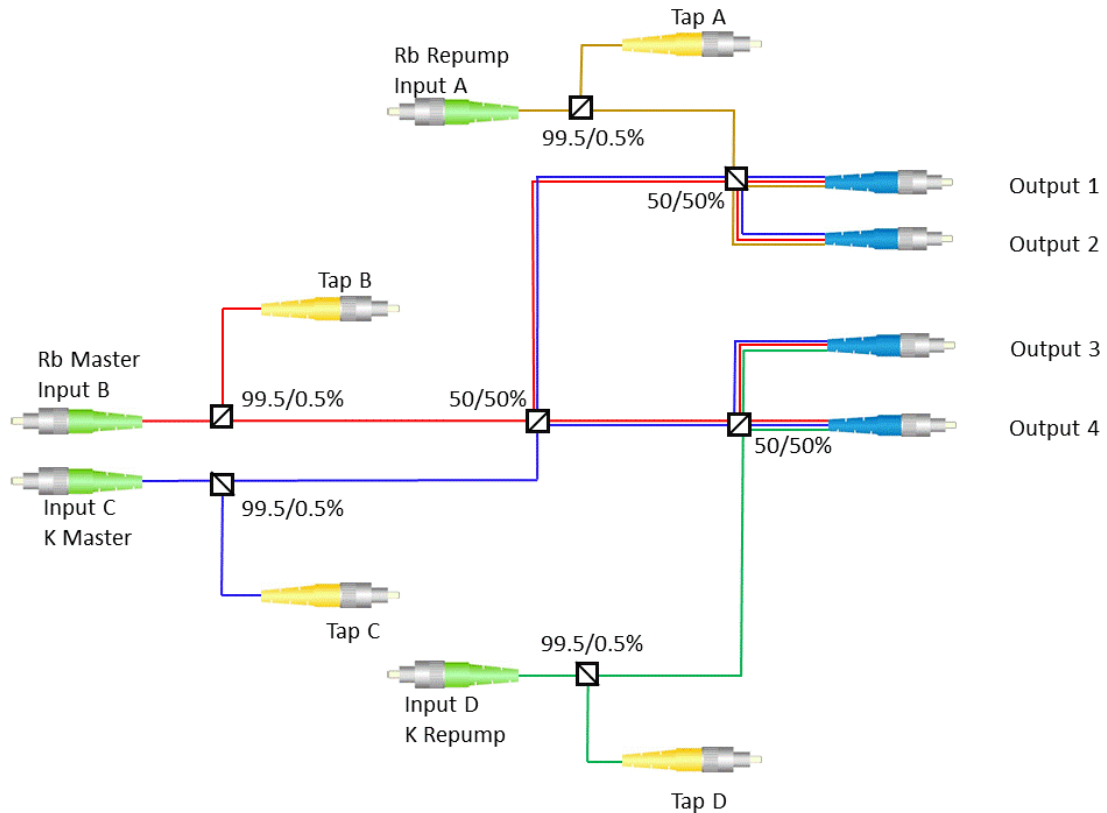


FIGURE 3.15: 2D-MOT 4 to 4 splitter (custom-made from Evanescent Optics). All fibers are polarization maintaining; all polarization is parallel. Beam splitters are amplitude splitters only. All connectors are FC/APC. Devices are able to handle upto 1 W on inputs and outputs. Inputs A and B are 780 nm; Inputs C and D are 767 nm.

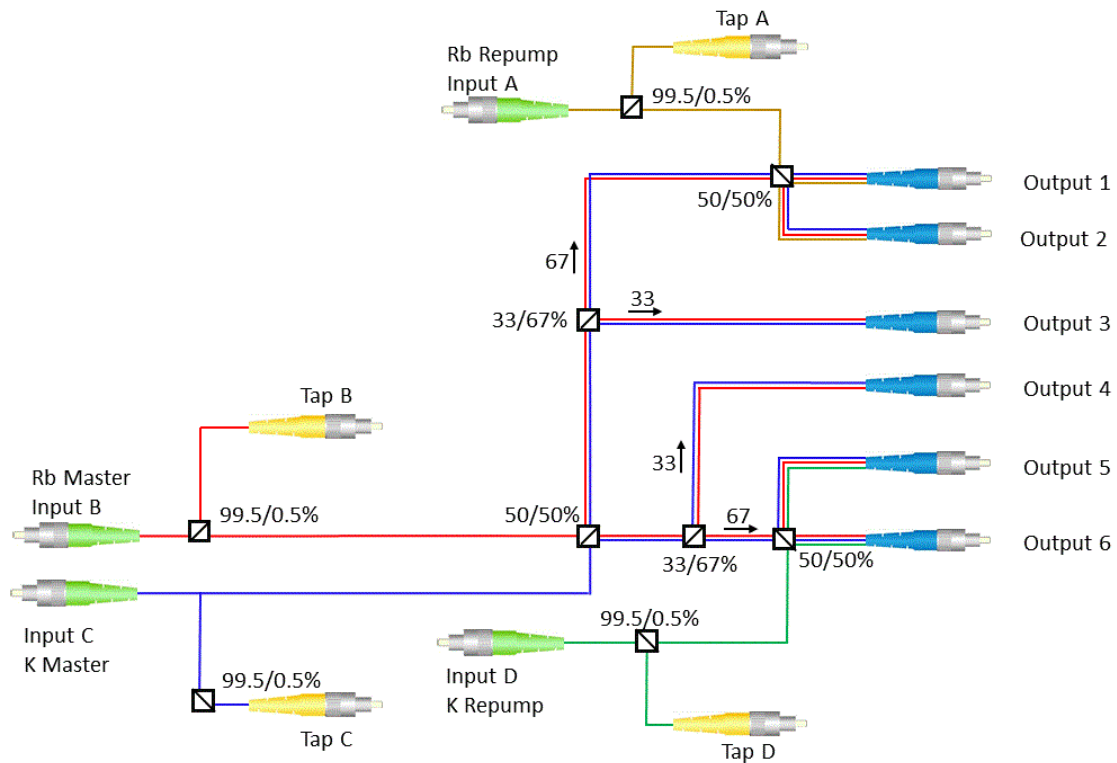


FIGURE 3.16: 3D-MOT 4 to 6 splitter (custom-made from Evanescent Optics). All fibers are polarization maintaining; all polarization is parallel. Beamsplitters are amplitude splitters only. All connectors are FC/APC. Devices are able to handle upto 1W on inputs and outputs. Inputs A and B are 780nm; Inputs C and D are 767 nm.

the beam splitter we have mixed repump-cooling light. This light is used for beat note locking and wavemeter monitoring.

### Beat note locking

For beat note locking, mixed light from the fiber beam splitter is detected with an amplified high-speed fiber photodetector ET-4000AF (Fig. 3.17).

The detector produces an RF-signal corresponding to the difference frequency between repump and cooling laser light. The beat note signal goes through 2 Mini-circuits amplifiers ZJL-7G+ to evaluation board EVAL-ADF4007EBZ1 where the frequency is divided by 64. A small portion of the divided signal goes through a Mini-Circuits ZFL-2AD+ amplifier to the frequency counter Startek ATH70 for monitoring. The evaluation board receives a reference signal from a digital frequency generator, Novatech 409B. Before the board, the reference signal is amplified with Mini-Circuits ZX60-4016E-S+, doubled with Mini-Circuits FD-2<sup>4</sup> and filtered with high pass filter Mini-Circuit BHP-150+. The evaluation board takes the reference signal and beat note signal and produces an output proportional to the frequency difference between them. The output signal goes through a low pass filter to the PID<sup>5</sup> block Toptica PID-110 in the cooling laser's controller.

An important part in beat note locking is to choose the correct reference signal. It can be calculated as follows: the frequency  $f_{rep}$  of the repump transition  $F = 1 \rightarrow F' = 2$  with respect to frequency  $f_0$  of the central transition  $5^2S_{1/2} \rightarrow 5^2P_{3/2}$  is

$$f_{rep} = f_0 + 4271.677 \text{ MHz} - 72.911 \text{ MHz}.$$

In addition Repump laser is locked 80 MHz below resonance:

$$f_{rep,laser} = f_0 + 4271.677 \text{ MHz} - 72.911 \text{ MHz} - 80 \text{ MHz}.$$

<sup>4</sup>Reference signal is divided by 2 inside the evaluation board EVAL-ADF4007EBZ1. That is why we multiply the signal before the input of the board

<sup>5</sup>Proportional Integral Differential

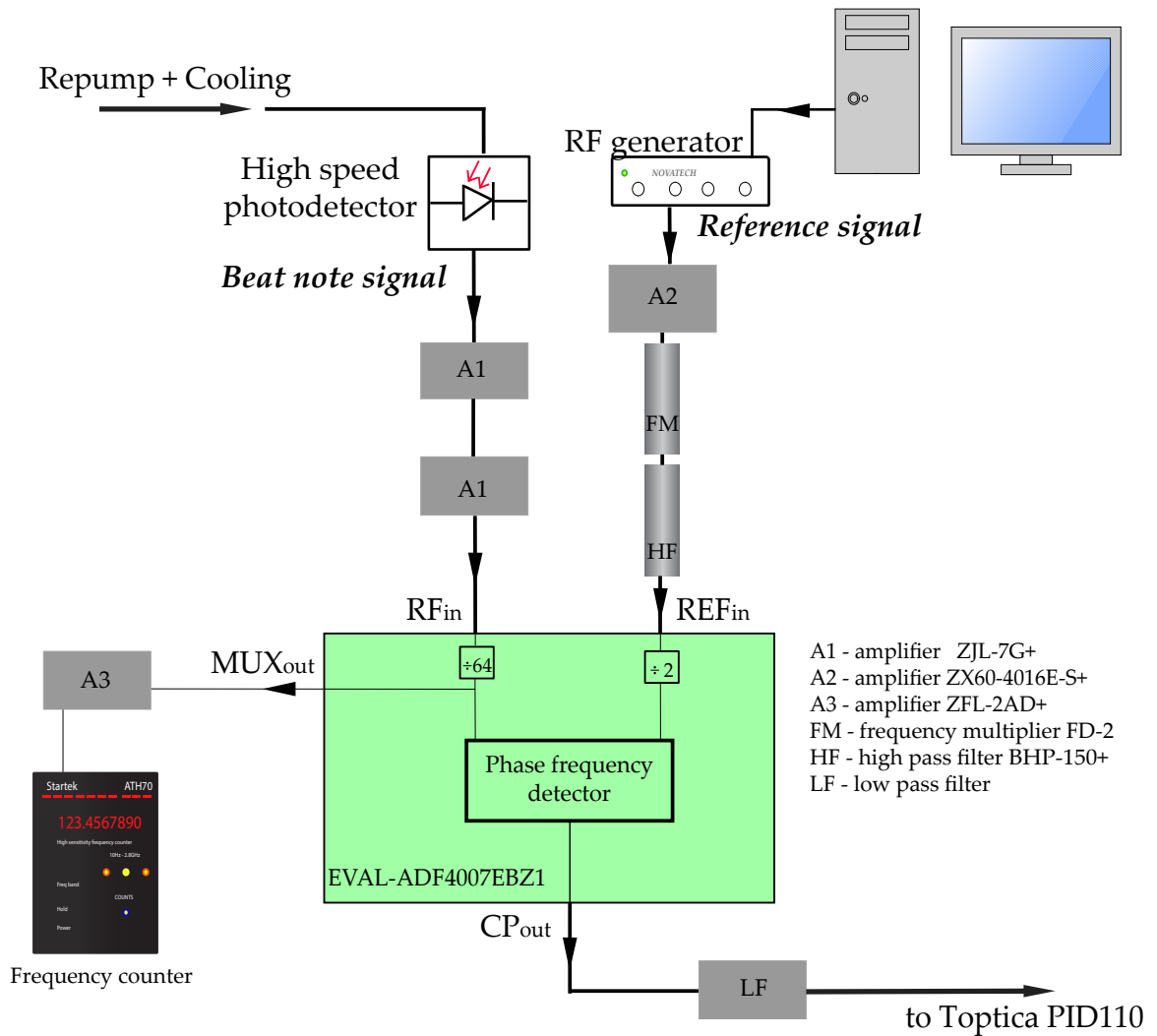


FIGURE 3.17: Beat note locking scheme

The frequency  $f_{cool}$  of the Cooling transition  $F = 2 \rightarrow F' = 3$  with respect to frequency  $f_0$  is

$$f_{cool} = f_0 - 2563.006 \text{ MHz} + 193.741 \text{ MHz}.$$

In the cooling laser optical setup, we use double-pass AOMs to have control on optical power and frequency. But that introduces +160 MHz shift to the light. So, we compensate this shift by locking the laser 160 MHz below resonance. In addition, for laser cooling the light must be red shifted. We use detuning equal to  $3\Gamma^6$ . So, the actual frequency that we want for the cooling laser is:

$$f_{cool,laser} = f_0 - 2563.006 \text{ MHz} + 193.741 \text{ MHz} - 160 \text{ MHz} - 18.198 \text{ MHz}.$$

Then, the difference between the repump and cooling frequencies is

$$f_{rep,laser} - f_{cool,laser} = f_0 + 4271.677 \text{ MHz} - 72.911 \text{ MHz} - 80 \text{ MHz} - f_0 + 2563.006 \text{ MHz} - 193.741 \text{ MHz} + 160 \text{ MHz} + 18.198 = 6666.2 \text{ MHz}.$$

In our beat note electronics, this frequency difference is divided by 64:

$$f_{beat} = 6666.031 \text{ MHz}/64 = 104.159 \text{ MHz}.$$

So, our reference signal for beat note locking is 104.159 MHz.

### Cooling laser's optical setup

The cooling laser's optical setup is shown on the Fig. 3.18

The cooling laser's main output power is split in two arms: the 2D-MOT path with 1.1 W and the 3D-MOT path with 0.5 W. Right after this splitting 110 mW is taken for optical pumping from the 2D-MOT path. This light goes through "Opt pump" AOM that shifts light -96 MHz and makes it resonant with transition  $F = 2 \rightarrow F' = 2$ . After that, the optical pumping light is combined with imaging light in a fiber beam splitter (see below).

---

<sup>6</sup> $\Gamma$  - Natural Line Width, for Rb  $D_2$  line is equal to 6.066 MHz

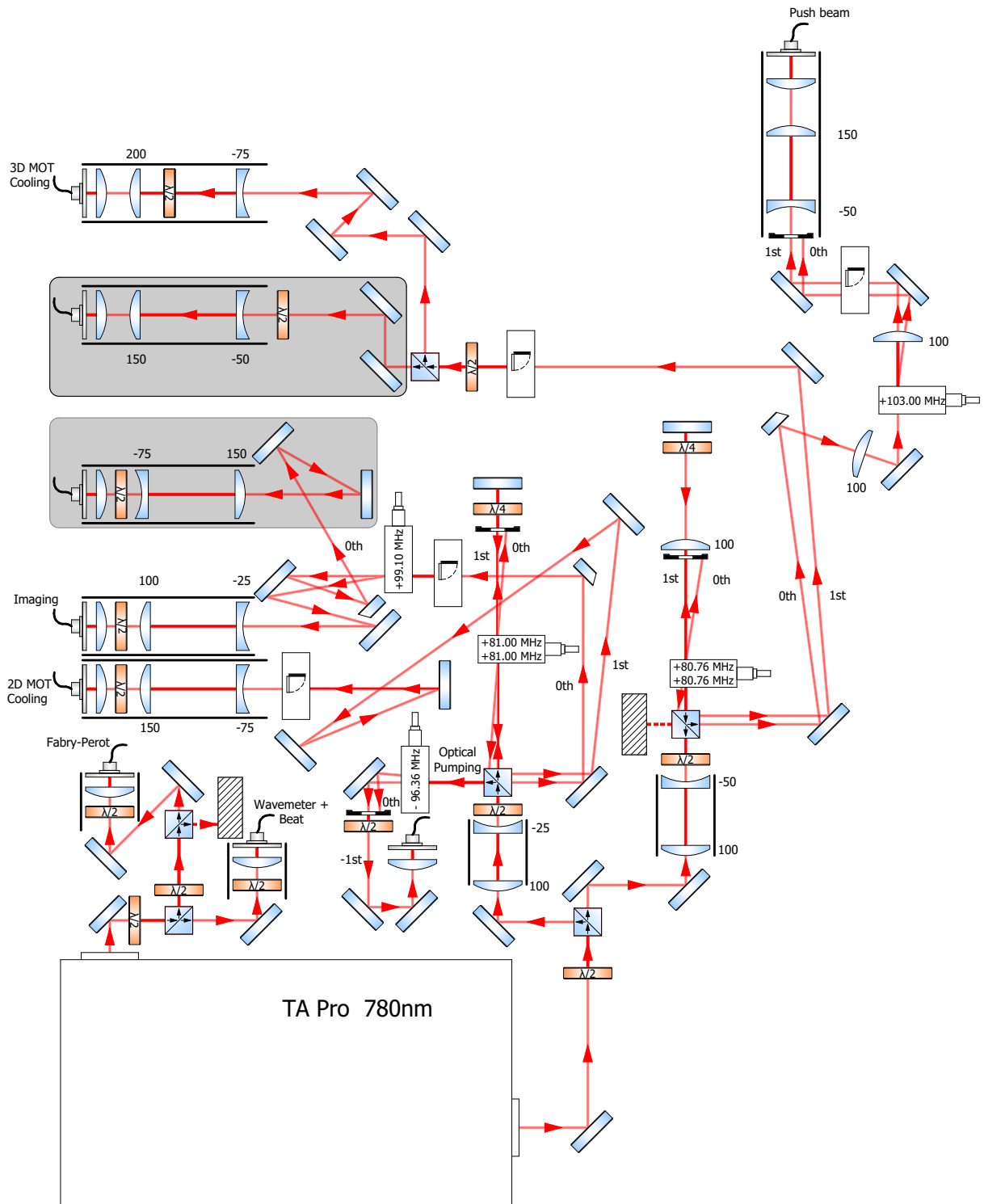


FIGURE 3.18: Cooling laser's optical setup. For legend see Fig. 3.13.

The rest of the 2D-MOT beam goes through the "2D-Cooling" double pass AOM. The first order of the first pass is shifted +81 MHz. Then this light is reflected to the same AOM. The first order of the second pass is now  $2 \times 81$  MHz up-shifted and has 350 mW power before the coupler. It goes to the 2D-MOT chamber through "4 to 4" beam splitter. The zeroth order of the second pass remains +81 MHz shifted and is used for imaging. Since we use an imaging technique based on absorption, light must be resonant with the chosen transition ( $F = 2 \rightarrow F' = 3$ ). That is why it is shifted with the "Imaging" AOM by +99.1 MHz. The imaging beam (4 mW) is coupled to the same beam splitter to which the optical pumping is coupled. We do not use optical pumping and imaging at the same time. Two beams just share one fiber, which was done for convenience.

The 3D-MOT beam also goes through a double pass "3D-Cooling" AOM. At the output we have 250 mW in the 1st order which is  $2 \times (+80.76$  MHz) shifted by AOM and has optimal detuning to cool Rb atoms in our setup. Since for the 3D-MOT we need 6 beams, the light is divided into 6 beams in "4 to 6" beam splitter. The zeroth order (77 mW) which is +80.76 MHz shifted, receives an additional +103 MHz shift in the "push beam" AOM and is used as a blue detuned push beam for the 2D-MOT.

### 3.3.3 Imaging

In our setup there are 2 imaging systems to study the atomic cloud, one in the horizontal plane and one in the vertical plane (Fig. 3.19). For imaging in the XY plane, the camera is located below the Science glass cell and the probe beam comes from above the cell. Since the probe beam goes in the  $-Z$ -direction, we call it "vertical" or "Top-Bottom" imaging system. To clear optical access for the imaging beam, the top and bottom horizontal pneumatic mounts for the MOT mirrors must be retracted. A colimated imaging beam with radius 1 mm goes through the cell and the two lenses right below it. After these lenses, the beam is reflected in the horizontal  $+X$  direction. Since it is already quite expanded we use a 2" – diameter protected gold-coated mirror Thorlabs PFE20-M01 to do this reflection. After the mirror the beam goes through two more lenses (also 2" in diameter) and, finally it hits the camera - Pointgrey BFLY-U3-13S2M-CS charge-coupled device with resolution 1288 x 964 and pixel

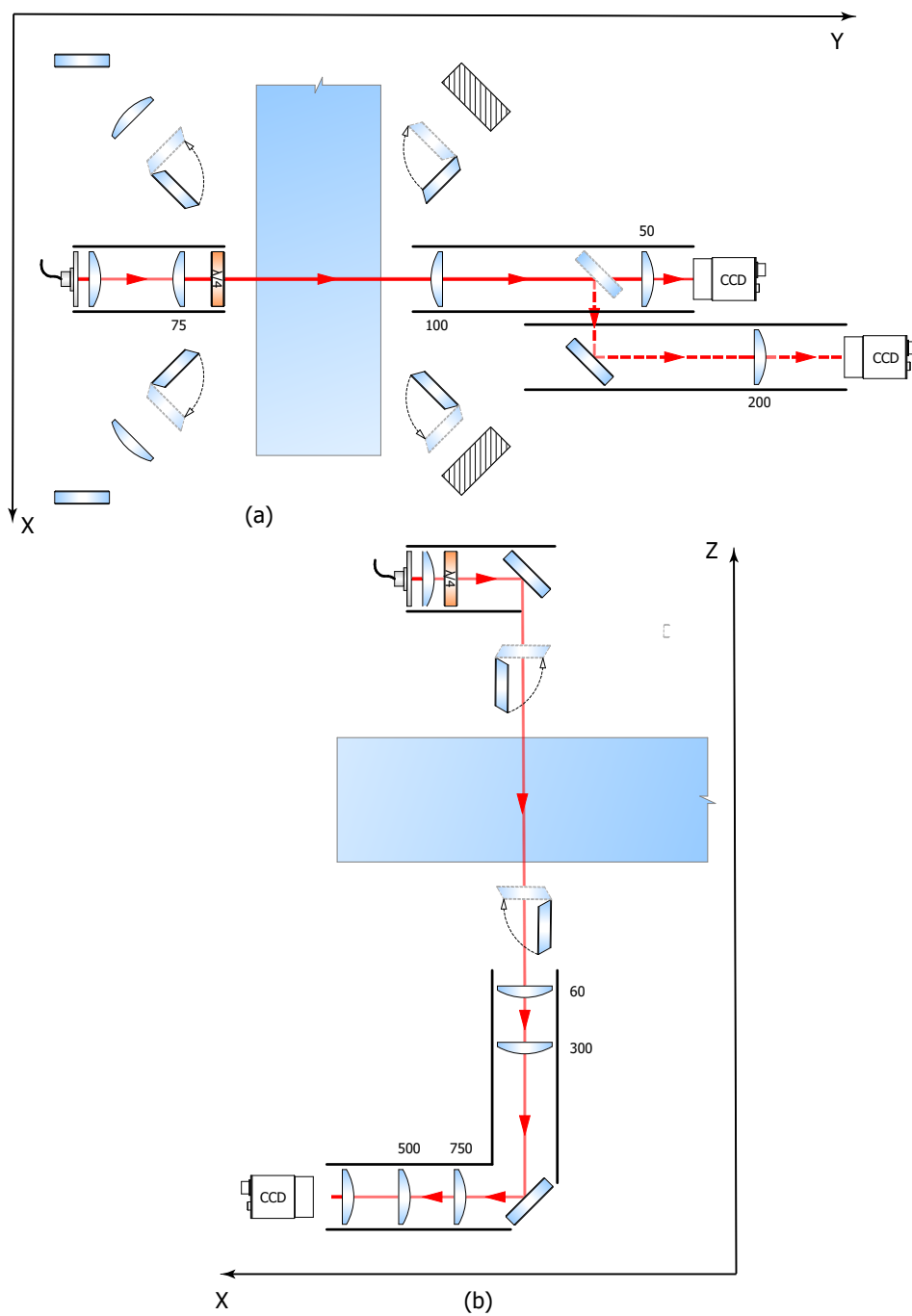


FIGURE 3.19: Optical setups for side (a) and vertical (b) optical systems. For legend see Fig. 3.13.

size (with no magnification) equal to  $3.75 \mu\text{m}$ . The camera sits on a translation stage with micrometer which allows us to focus it precisely.

The magnification of our XY imaging system is 6 times, so we expect that the effective pixel size is  $0.625 \mu\text{m}$ . The field of view of this system is approximately  $600 \times 600 \mu\text{m}$  meaning that the Top-Bottom imaging system can be used only on the latest stages of the experiment where the cloud is small enough. Also, there is a limitation connected with the fact that for using the vertical imaging system, the pneumatic mounts must be retracted which takes 3 s.

To get information about the atomic cloud in the initial stages of the experiment, we use the side imaging system. The imaging beam in this case propagates in the +Y direction and enters the glass cell from the North side. On the opposite side of the cell there are 2 imaging optical setups. One of them provides 2 times magnification, the second one - 2 times demagnification. To switch between them, a removable mirror is installed. For side imaging, we use Pointgrey BFLY-U3-03S2M-CS charge-coupled device with resolution  $648 \times 488$  and pixel size with no magnification equal to  $7.4 \mu\text{m}$ .

### Pixel size calibration

All information we get during the experiment about the atomic cloud comes from the imaging system. Any measurements that can be done directly from images are in pixel units. Further image analysis is impossible without a precise calibration of pixel size for each imaging system. For the side imaging system pixel size calibration, we use gravitation constant measurements. To do that, we release a small cloud (usually after RF evaporation) from the trap and record its position as it falls due to gravity. The cloud falls in an ultra high vacuum region, so we assume no resistance from background atoms. As a result, we have data of the cloud's vertical displacement with time and fit it with motion kinematic equations for the case of constant acceleration (Fig. 3.20).

From the fit we get acceleration due to gravity in  $\text{pixels}/\text{s}^2$  and compare it with known value for  $g$ <sup>7</sup>. This gives us the pixel-to-meter conversion. In addition, we check if measured the pixel size matches what is expected. The expected value is

---

<sup>7</sup>For Edmonton  $g = 9.811\text{m}/\text{s}^2$

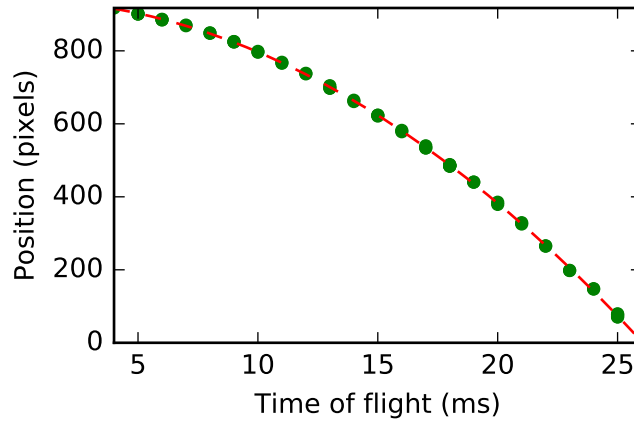


FIGURE 3.20: Free fall measurements for pixel calibration. Cloud was released from the optical dipole trap and its vertical position was recorded with time. Green dots represent raw data. Red dashed line is a fit to data using expression  $z_0 + vt + 0.5gt^2$ . From the fit pixel size  $(3.62 \pm 0.03)\mu m$  for side imaging system with 2 times magnification

| Magnification | Expected pixel size,<br>$\mu m$ | Measured pixel size,<br>$\mu m$ |
|---------------|---------------------------------|---------------------------------|
| Side 1/2      | 14.8                            | 14.4                            |
| Side 2        | 3.7                             | 3.62                            |
| Top 6         | 0.625                           | 0.6                             |

TABLE 3.3: Imaging system pixel size

calculated as the actual camera's pixel size divided by the predicted magnification of the imaging system.

It is impossible to do the same measurements for the vertical imaging system. So, to calibrate it we compare images of the same stage of the experiment from the Top-Bottom imaging system with images from The Side imaging system. From side images we extract information about the cloud in real units and from the Top-Bottom imaging system, in pixels. Then we determine the pixel size such that images from both imaging systems give the same results. The measured and expected pixel sizes for our imaging systems are presented in the Table 3.3

### 3.3.4 Optical dipole trap

To trap atoms in the last stage of the experiment, we use a far-red-detuned crossed beam optical dipole trap (ODT) (Fig. 3.21). It is based on IPG Photonics YLR-10-1064-LP - 1064 nm 10 W fiber laser. For the ODT optics, an aluminum optical breadboard was mounted on the level of the science chamber. The laser's output fiber is fixed on the plate. Right after the fiber we installed Thorlabs IO-8-1064-VHP high power isolator to protect laser from back reflection. After the isolator, the beam size is reduced by a telescope to fit within the "Power" AOM's window. For this ODT, we use two Gooch and Housego 3080-1990 high-power AOMs. They are mounted on home-made aluminum holders which work also as heat sinks. The AOMs are controlled by Gooch and Housego 1080AF-AINA-3.0 RF drivers. The first AOM is set to control overall power in the ODT setup and is called "Power" AOM. Its zeroth order is absorbed in a high power beam block Thorlabs BT610. The first order is reflected to the "Split" AOM. The second AOM is used to split beam into two and to control the power distribution between them. The zeroth and first order beams after the Split AOM are expanded with a telescope, separated and focused with lenses to the science chamber. These beams intersect inside the chamber with angle  $90^\circ$ . Since the trap depth depends on light intensity, high laser power and relatively small beams sizes are required. But, because of the 3D-MOT optics and pneumatic mirrors, we can not put ODT lenses closer than 200 mm from the center of the cell. We use the smallest focal distance lenses that we can – 200 mm – and with the expansion of the beams with the telescope after the second AOM which helps to, we can focus the beams tighter. As a result, we achieve  $75 \mu\text{m}$  for the  $1/e^2$  beam radius at the crossing point.

After losses in the optical isolator, Power AOM, losses for reflections in lenses and the glass cell, the maximal power in each ODT beam is 2.6W inside the Science chamber. Taking into account  $\omega_0 = 75 \mu\text{m}$  our optical dipole trap has maximal depth  $76 \mu\text{K}$ .

The optical power in the ODT is dynamically stabilized with feedback control. For that purpose, a beam sampler is placed right before the Split AOM. It reflects 5% of the power to a photodiode detector. The signal from the detector is compared with a reference signal from the control computer by Newport LB1005 high-speed

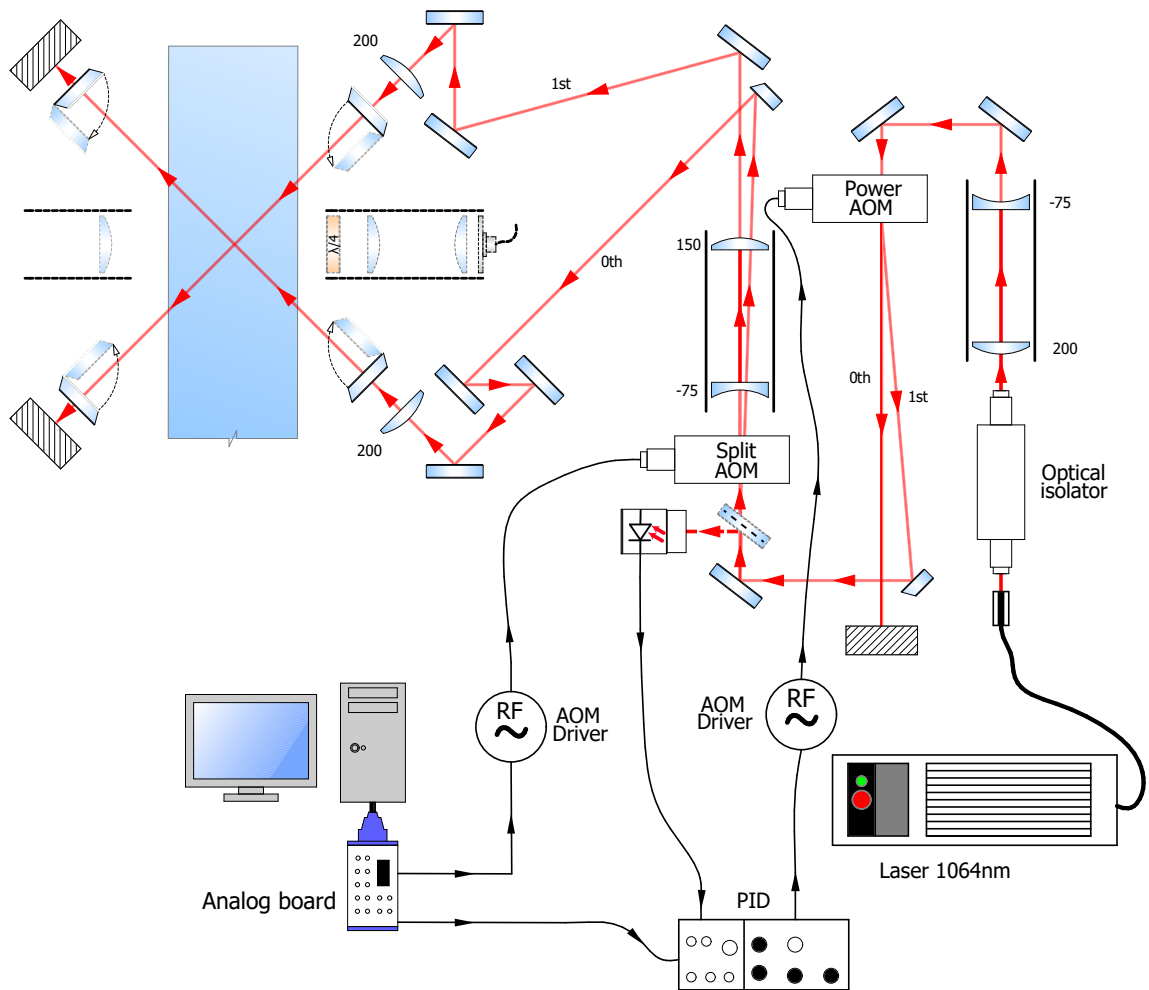


FIGURE 3.21: Optical dipole trap setup. For legend see Fig. 3.13.

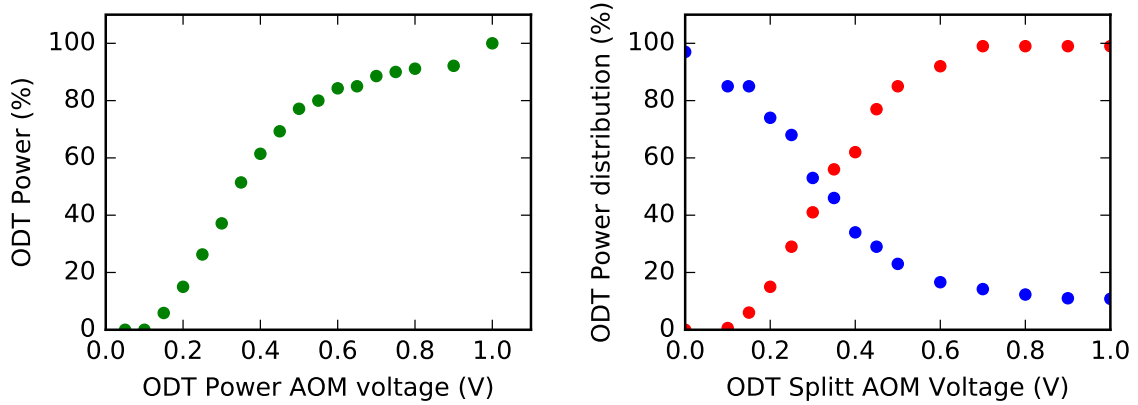


FIGURE 3.22: ODT Power and Splitt AOM calibration. Left graph shows overall power of ODT with respect to Power AOM voltage. Right graph shows distribution of power between two ODT beams at different Splitt AOM voltage. Blue graph shows trend for 0th order, red one - for 1st order. Equal power is reached at 0.32 V.

servo controller. It creates an output signal that controls the Power AOM's driver. If the signal from the detector does not match the reference signal, PID electronics adjust the optical power in the ODT by sending more or less light into the first order diffraction of the Power AOM. PID parameters were selected experimentally, and in the final configuration, the response time of the feedback control is  $100 \mu\text{s}$ .

### Optical dipole trap alignment

The most sensitive part of the ODT is alignment inside the glass cell. It is a difficult task because beams with waist  $75 \mu\text{m}$  must be precisely aligned with respect to each other and to the cloud in both the horizontal and vertical planes.

The optical dipole trap is loaded from the magnetic trap in the final stage of RF evaporation. For that to be successful, the ODT beams should cross each other at the center of the atomic cloud. The best position for crossing point would be the center of magnetic trap where the coldest atoms are. But, due to Majorana spin flips, atoms leave the trap. If the ODT beams are aligned to that point the loading efficiency is low. As a result, the highest efficiency is achieved if beams intersect  $\omega_0$  below the center of the cloud [58].

Directly before the glass cell the ODT beams share an optical path with the 3D-MOT beams. These MOT beams define the cloud position. So, initially we align ODT beams inside 3D-MOT cages using alignment targets. Such rough alignment is enough to hit the cloud with both beams. From that point we use cameras for further alignment since some portion of atoms are trapped inside each beam and they become visible in absorption images.

For precise alignment, we use the effect of Majorana losses in the center of the cloud. With the side view, we roughly align the beams to the center of the cloud, us-

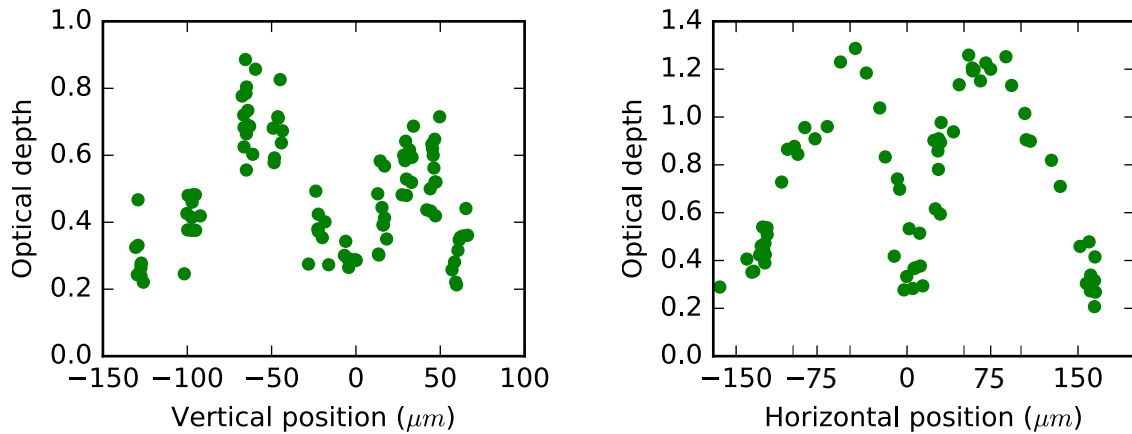


FIGURE 3.23: Optical depth (OD) as a function of ODT 1st order beam position in vertical(left) and horizontal(right) planes. OD represents the number of atoms trapped in the beam. 0 corresponds to the center of the atomic cloud(which matches the magnetic trap center). The number of trapped atoms is the highest when beam is placed below 0.

ing absorption images as our guide. Then with top view we do the same – roughly align beams to cross in to the center, and switch back to side view. First, we align beams in vertical direction. For that we block the first order beam and move the zeroth order to the edge of the cloud. From that point we start to move the unblocked beam through the cloud with the smallest steps possible with our mirror mounts. After each displacement, we record beam’s position and the optical density of trapped atoms (Fig. 3.23).

As we move the beam closer to the center of the cloud, we trap more atoms and the imaged optical depth (OD) increases. But at some point directly near the center,

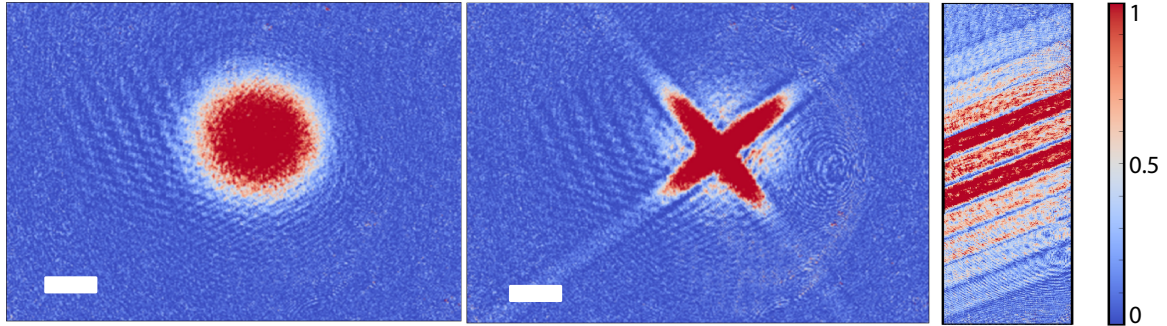


FIGURE 3.24: Absorption images of the atomic cloud before(left) and after (center) transfer to the aligned ODT. Images were taken with bottom camera after RF evaporation to 1 MHz. White scale bare = 100  $\mu\text{m}$ . Right image is a compilation of 10 images with trapping beam at different position in horizontal plane from the left edge to the right edge of the cloud. A clearly visible Majorana scale region appears in the center between the two brightest lines. Color scale shows optical depth.

the beam reaches the Majorana losses region and the OD drops. When the beam leaves these losses region, the number of trapped atoms jumps up. As the beam moves further, the OD decreases until the beam exits the cloud. From the recorded data, we estimate the position of the beam which corresponds to the OD dip and set it at that position. After that we block the zeroth order, unblock the first order and repeat this procedure. As a result, both beams are aligned to the center of the cloud in the vertical direction. It is clear from the data that the ODT loading efficiency is higher if beam is located below magnetic trap center.

After vertical alignment, we switch to the Top-Bottom imaging system. In the horizontal plane we align beams one by one in the same way as in the vertical. Unlike the vertical scan, the horizontal one does not show different loading efficiency on the opposite sides from the cloud's center. It is important to use only horizontal displacement here and not to touch the vertical displacement knobs. If they were touched by mistake, the vertical alignment must be done again. Now beams cross right in the center of the atomic cloud where Majorana losses are the strongest. To maximize ODT loading efficiency, we switch back to the vertical imaging system and move each beam  $\omega_0$  below its current position.

After successful alignment we are able to load 60 % of the atoms from final stage of RF evaporation into the optical dipole trap (Fig. [3.24](#)).

# Chapter 4

## Results

In order to achieve Bose-Einstein condensation, the temperature of an atomic cloud must be lowered to its transition temperature, which, for dilute gases, is typically equal to a few hundreds of nanokelvins. At the same time, atom number must be kept at an appropriate level to reach high phase space density, which defines the condition for condensation to start. So, during characterization and optimization of our experimental steps we were focused mainly on two quantities - temperature and atom number. In this chapter I will give description of our experimental sequence, laser cooling scheme, operating parameters and brief characterization for each cooling step. In the end of the chapter evaporation paths for RF and ODT evaporation that lead to quantum degeneracy and two signatures of BEC (bimodal distribution and inversion of aspect ratio) are presented.

### 4.1 Experimental sequence

Our experiments run in cycles. In the end of each cycle a destructive imaging measurement is performed. Therefore the BEC needs to be prepared again for the next measurement. A typical cycle consists of all steps necessary for BEC production and lasts about 30 s. An experiment starts by loading the 3D-MOT. During that time 2D-MOT is also on. After loading, we turn off the 2D-MOT and keep it off during the next steps until a new cycle of the 3D-MOT loading begins.

When the MOT is fully loaded, we turn off the quadrupole magnetic field and perform polarization gradient cooling. After this step, the cooling light is turned off. In the next step, atoms are optically pumped into a magnetically trappable state. Our

pneumatic mirrors are moved down to allow the optical dipole beams to access the chamber; these beams are used in the final steps of cooling. After optical pumping the magnetic field is turned on again so that the atomic cloud is trapped in a magnetic trapping potential. During the first part of the magnetic trapping, we set the amount of the current that is just enough to hold the atoms against gravity. Next, the magnetic trap is compressed spatially by linearly ramping the current up. When the trap is fully compressed we initiate radio frequency (RF) induced evaporation. After RF, evaporation, the atoms are transferred to the optical dipole trap (ODT). This process includes simultaneously decreasing the magnetic field to zero and increasing the ODT beams to maximum power. When the atoms are transferred to the ODT, we perform a final evaporation by decreasing the ODT power until condensation starts. In the end of this process we obtain a BEC with typically about  $10^5$  atoms.

## 4.2 Magneto-optical traps

Two key elements of our BEC setup are the magneto-optical traps (MOTs). Our 2D-MOT collects Rb atoms that diffuse from the oven region and creates a collimated atomic beam that propagates along  $+X$ . The atomic flux goes through a differential pumping tube and enters the 3D-MOT region. Here the atoms are trapped and cooled in 3 dimensions, thus forming the initial atomic cloud. The efficiency of the described process determines the success of all subsequent steps.

Our 2D-MOT is formed with a magnetic field gradient, created by 4 coils, and 4 laser beams. Each pair of the beams is counter-propagating and the beams are perpendicular to the magnetic field's zero-field line which coincides with  $X$ -axis. The beam pairs are directed along the  $Y$ - and  $Z$ -directions. The beams have an elliptical cross section with a waist  $\omega_x=2.5$  cm along  $X$ -axis and  $\omega_p=1$  cm along perpendicular directions. While the overall alignment of such large beams is not a difficult task, particular attention should be paid for the alignment in  $X$ -direction. A misalignment in this direction may cause atoms pushed away from  $X$ -axis when the atomic beam exits the 2D-MOT.

All of the 2D-MOT beams are  $\sigma^+$  polarized with respect to their propagation direction and they are red detuned by 16 MHz from the  $F = 2 \rightarrow F' = 3$  transition

| 2D-MOT  |         |        |           |           |           |           |
|---------|---------|--------|-----------|-----------|-----------|-----------|
| Beams   | Top     | Bottom |           | North     | South     |           |
| Cooling | 42 mW   | 37 mW  |           | 46 mW     | 50 mW     |           |
| Repump  | -       | -      |           | 18 mW     | 17 mW     |           |
| 3D-MOT  |         |        |           |           |           |           |
| Beams   | Top     | Bottom | Northeast | Northwest | Southeast | Southwest |
| Cooling | 18.2 mW | 16 mW  | 13.7 mW   | 23 mW     | 20 mW     | 18.3 mW   |
| Repump  | -       | -      | -         | 4.8 mW    | 6.1 mW    | -         |

TABLE 4.1: 2D- and 3D-MOT light power levels.

(Fig. 4.1). This value is determined experimentally by scanning the detuning from  $2\Gamma$  [59] to  $10\Gamma$  until the maximum number of atoms trapped in 3D-MOT are found. The pair of beams along  $Y$ -axis contain repump light on resonant with  $F = 1 \rightarrow F' = 2$  transition. Since there is probability to excite atoms with cooling light in states other than the  $F' = 3$  state, they can fall into both ground levels. Atoms in  $F = 1$  are unreachable by cooling light. Repump is used to close the cooling loop by moving atoms from the ground  $F = 1$  state into the ground  $F = 2$ . It is present also in the 3D-MOT, optical molasses and optical pumping. The typical power of cooling and repump light for each beam is given in Table 4.1.

Because of the described configuration of our 2D-MOT, atoms are cooled down in transverse directions (along  $Y$ - and  $Z$ -axes), but they keep their speed along the  $X$ -axis. As a result, a large atomic flux towards the 3D-MOT chamber is generated. The atoms with high velocities along the  $X$ -axis do not spend enough time in the beam crossing region, and hence can not be cooled sufficiently. They are filtered out by a differential tube with a diameter of 4.5 mm. As a result, the average longitudinal velocity of the atoms also decreases [61].

In the 2D-MOT there are two additional kinds of atoms that do not contribute to the atomic flux in a useful manner; atoms that move in the  $-X$  direction and atoms that move in  $+X$  direction with small speeds. Both of them can contribute to the useful flux by using laser beams with different detunings which are referred to as push beams [59]. In our setup we use a blue-detuned push beam to accelerate slow

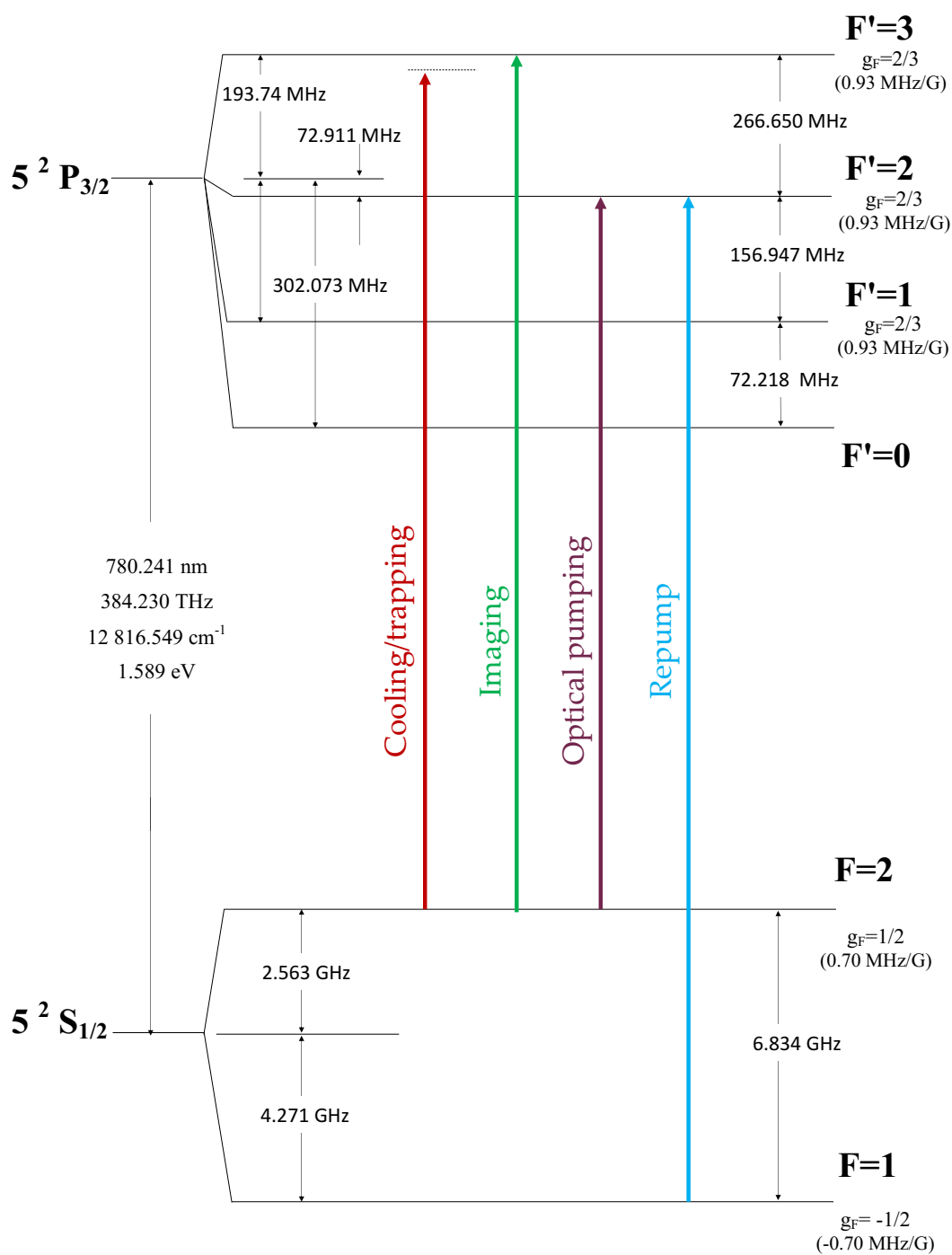


FIGURE 4.1:  $^{87}\text{Rb}$   $D_2$  transition level diagram with marked transitions used for our experiment. Adapted from [60]

atoms.

The push beam is a colimated beam with a waist of  $w_{push} = 1.5$  mm and a power of 20 mW. It is aligned to pass through the entire vacuum system along the X-axis up to the Science chamber. But when it directly hits the atomic cloud of the 3D-MOT the atomic cloud is destroyed (this can be used as a starting point for alignment). The best MOT-loading efficiency is obtained when the beam is aligned above the 3D-MOT cloud. The optimal push beam detuning is determined experimentally by maximizing the number of atoms trapped in the 3D-MOT. It is detuned 5 MHz above the  $F = 2 \rightarrow F' = 3$ . In this way we are able to increase the number of trapped atoms up to ten times in our 3D-MOT.

The atomic flux from the 2D-MOT is collected by the 3D-MOT. This system allows us to trap atoms to a single point and to cool them in all directions. In order to provide this, 6 mutually orthogonal beams are used. They are grouped in 3 pairs of counter-propagating beams: top - bottom; Northeast - Southwest; Northwest - Southeast (Fig. 4.2). This last pair is mixed with repump light. The beams, together with quadrupole magnetic field, form a 3-dimensional magneto-optical trap.

The cooling light in the 3D-MOT is red-detuned by  $3\Gamma$  (18 MHz) below the  $F = 2 \rightarrow F' = 3$  transition. The repump light is resonant with the  $F = 1 \rightarrow F' = 2$  transition. Each 3D-MOT beam is collimated with a radius of  $w_{3D} = 1$ cm and has  $\sigma^+$  polarization with respect to its propagation direction. Ideally, all 6 beams would have the same power, but because of imperfections (mainly imbalance of the arms of the beam splitter) this is not the case, see Table 4.1. However, in general, a MOT is not sensitive to such small deviations in power.

Another important parameter for a MOT is the magnetic field gradient. A too-low magnetic field gradient leads to lower trap depths, resulting in fewer trapped atoms. On the other hand, overly high gradients cause small effective detunings, leading to less efficient cooling [62]. We found an optimal value of 10.5 G/cm for our setup; this was determined experimentally by measuring the number of trapped atoms with respect to various current values in 3D-MOT coils.

Furthermore, for an efficient MOT the beams must cross in a single point, and this point has to match the center of the quadrupole magnetic field. Optical alignment of the MOT beams is done using a CCD camera. By monitoring fluorescence coming



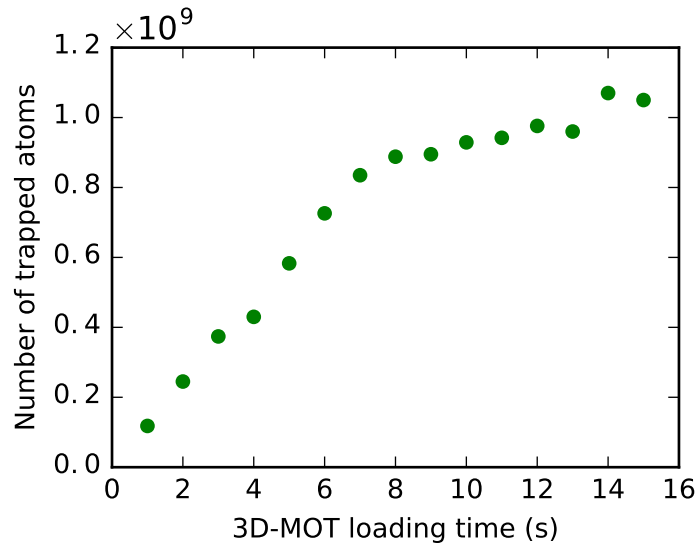


FIGURE 4.3: Atom number trapped in 3D-MOT at different loading time. Steady state is reached after 8 seconds.

from the atoms, the cloud in the MOT is visually made big and round as much as possible. Here, it is important to obtain the right shape. If the 3D-MOT beams are not aligned properly then trapping forces will not be equal in different directions, leading to distortion of the MOT. After this step, the alignment is fine-tuned to maximize the number of atoms in the MOT. At this stage, we use absorption imaging to evaluate the atom number. When the optical alignment is completed, the magnetic trap center can be moved with bias fields to match the beams' crossing point. By scanning the bias fields and via absorption imaging, we find the configuration which produces the highest atom number in the 3D-MOT. For the bias field optimization, it is necessary to make at least 2-3 iterations of scanning. Usually, the alignment and bias field optimizations lead to an increase in the number of atoms in the MOT, but there is a limit. At some point, the atom number will reach its maximum (Fig. 4.3) because of two competing processes: atom trappings and atom losses. The growth rate of the number of atoms is described as [63],

$$\frac{dN}{dt} = R - \frac{1}{\tau}N,$$

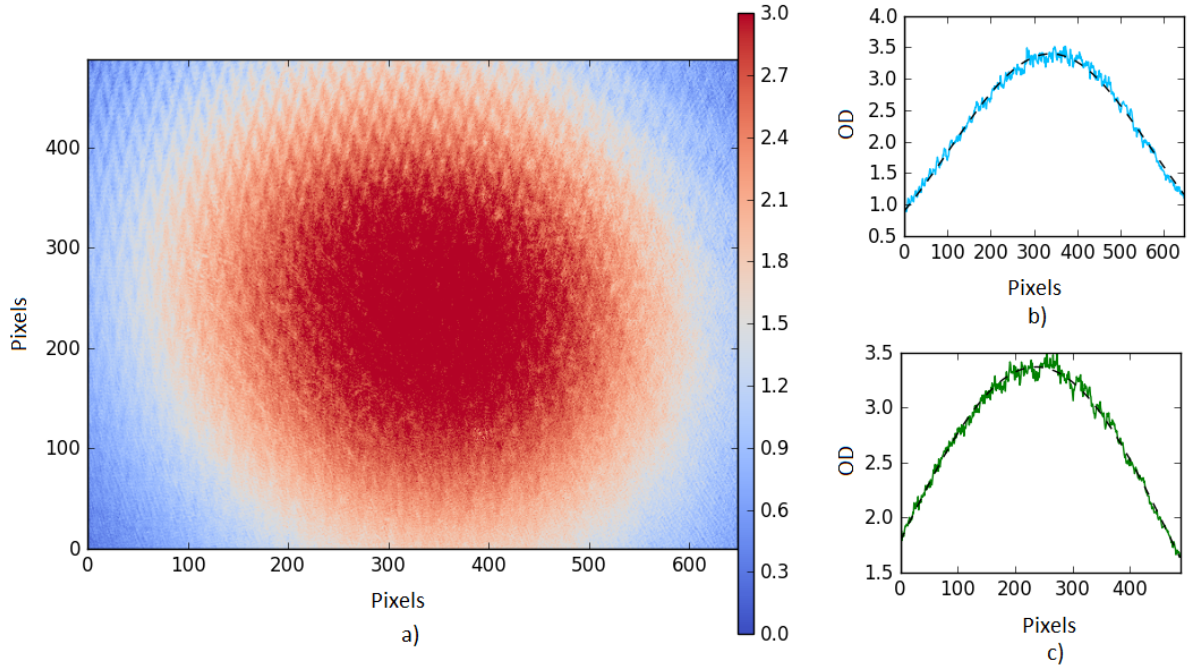


FIGURE 4.4: a) Typical 3D-MOT absorption image taken after 10 ms time-of-flight. MOT load time is 15 s. Color scale indicates optical depth. b) and c) are X and Y cross sections respectively. Atomic density distribution in 3D-MOT is well fitted with a Gaussian function. Pixel size is  $14.4 \mu\text{m}$ .

where  $R$  is loading rate,  $1/\tau$  is loss rate due to collisions between trapped atoms, and  $N$  is number of atoms trapped. As  $N$  grows over time, at some point these processes balance each other and a steady state in atom number is reached. In our experiment we load the MOT for 10-15 s. During this time typically  $\sim 10^9$  atoms are trapped and the cloud temperature is around  $500 \mu\text{K}$ . In our absorption imaging, a large optical depth of the atomic cloud might cause us to underestimate the number of atoms. A typical 3D-MOT absorption image is shown in Fig. 4.4.

| Optical molasses |        |        |           |           |           |           |
|------------------|--------|--------|-----------|-----------|-----------|-----------|
| Beams            | Top    | Bottom | Northeast | Northwest | Southeast | Southwest |
| Cooling          | 5.4 mW | 4.8 mW | 4.2 mW    | 6.0 mW    | 5.6 mW    | 5.4 mW    |
| Repump           | -      | -      | -         | 0.2 mW    | 0.24 mW   | -         |

TABLE 4.2: Optical molasses light power levels.

### 4.3 Polarization gradient cooling

When the MOT is fully loaded, we turn off the 2D-MOT light and magnetic field such that they do not affect the next cooling/trapping processes. After the 3D-MOT stage, the atomic cloud is further cooled with a polarization gradient cooling technique. In this process we set the current of the 3D-MOT coils to zero in order to remove the quadrupole magnetic field. The cooling and repump light powers are lowered to their optimal levels for obtaining so called "optical molasses" (Table. 4.2). Next, the cooling light detuning is immediately red-shifted to  $-24\Gamma$ , and it is swept linearly to  $-3\Gamma$  over 18 ms (molasses duration). An AOM can't provide such a large frequency shift, but this is easily achieved by changing the beat note frequency from 106.43 MHz to 104.15 MHz.

While in the 3D-MOT stage, all parameters were optimized to maximize the atom number. In the polarization gradient cooling step, however, optimization is typically a trade-off between low temperature and high atom number. Generally the molasses step is sensitive to residual magnetic field; it starts losing its efficiency when the residual field exceeds 100 mG [64]. This is why bias fields should be carefully scanned in order to cancel external fields. In addition, when a magnetic trap is set up (with no optical fields) we re-scan the bias fields in the molasses stage to minimize the atomic cloud temperature in the trap.

With 20 ms of polarization gradient cooling we are able to keep almost all atoms trapped in the MOT ( $\sim 10^9$ ) and cool the cloud down to  $50 \mu\text{K}$ . After molasses, cooling light is turned off for the rest of the experiment.

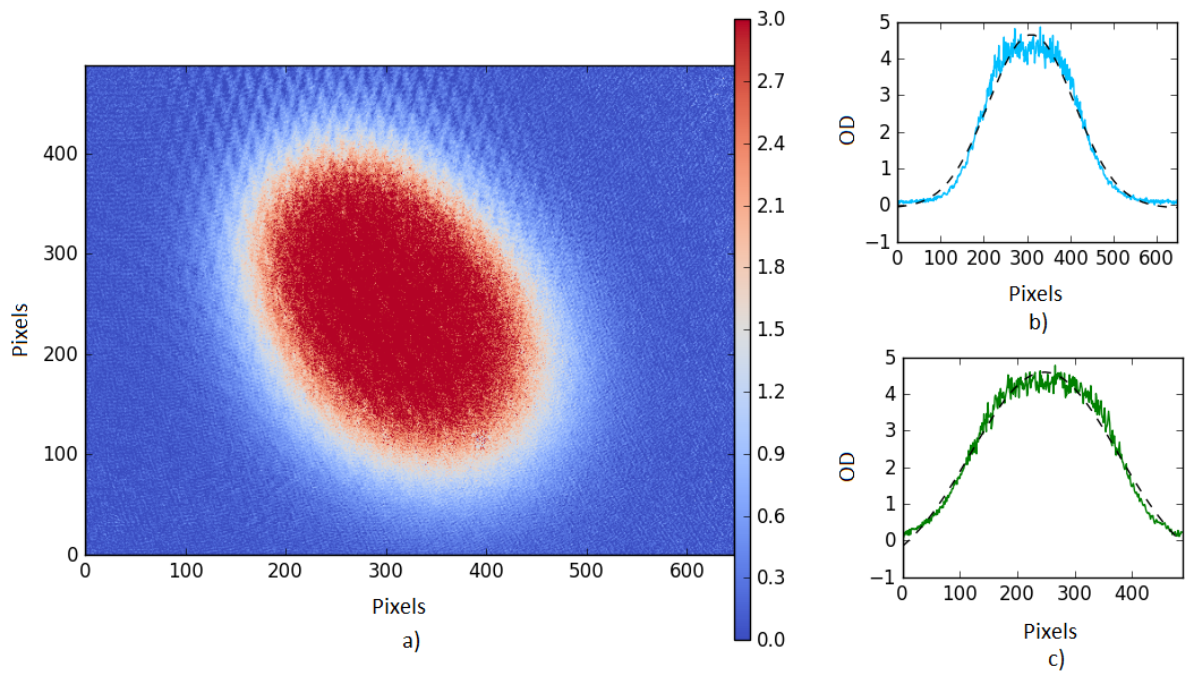


FIGURE 4.5: a) A typical molasses absorption image taken after 10ms time-of-flight. Atom number in molasses is  $10^9$ . Atomic cloud temperature is  $50 \mu\text{K}$ . Color scale indicates optical depth. b) and c) are X and Y cross sections, respectively. At OD of more than  $\sim 3$ , the images are saturating and the flat tops are likely an imaging artifact. Pixel size is  $14.4 \mu\text{m}$ .

## 4.4 Magnetic trapping

With optical molasses we reach the lowest temperature that we can achieve in our setup via laser cooling. To cool down the atomic cloud further, we use forced evaporative cooling from the magnetic trap. Before transferring atoms to the magnetic trap we optically pump them into a magnetically-trappable state. By using circularly polarized light atoms can be moved between  $m_F$  levels. Each absorption of  $\sigma^+$  polarized photon increases  $m_F$  by 1; and decreases by 1 for  $\sigma^-$  polarization (Fig. 4.6). When an atom is moved into the state with maximal possible  $m_F$  it cannot absorb pumping light and such state is called "dark state".

### 4.4.1 Optical pumping

For pumping, we use light resonant with the  $F = 2 \rightarrow F' = 2$  transition. A bias field of 1.525 G in the  $-Y$ -direction is on to set quantization axis.  $X$  and  $Z$  bias currents are equal to 0. The pumping beam has 0.45 mW of power and is  $\sigma^+$  polarized with respect to the magnetic field direction  $-Y$ . To remove atoms from the  $F = 1$  state, the repump light is turned on with the same power as for 3D-MOT. To optimize optical pumping parameters, we check load efficiency into the magnetic trap. During 0.6 ms we are able to pump almost all  $10^9$  atoms in the desired  $|F = 2, m_f = 2\rangle$  state.

### 4.4.2 Magnetic trap (MT)

Once the atoms are pumped into a magnetically-trappable state we turn on a quadrupole magnetic field. Since during the optical pumping stage no trapping mechanism is present, the magnetic field rising time should be kept as small as possible to re-catch the atoms until they fall due to gravity. To lower the turning-on time, we set the coil current of the magnetic trap to 200 A for the first millisecond. However, after 1 ms it only reaches 65 A, which corresponds to our optimal trapping magnetic field gradient of 27.2 G/cm. So, after this time, we switch the coil current to 65 A and hold the atomic cloud for an additional 100 ms. A magnetic field gradient of 27.2 G/cm was chosen as the maximal gradient that can hold against gravity atoms in the  $|F = 2, m_f = 2\rangle$  state but can not hold atoms in the  $|F = 2, m_f = 1\rangle$  state. Cleaning the trap

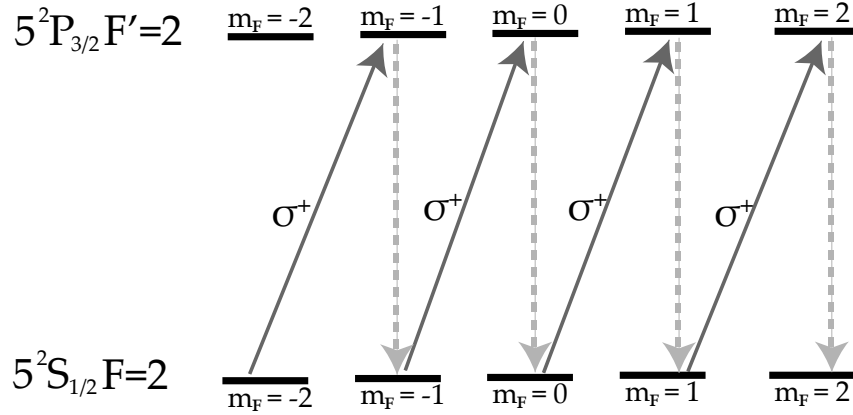


FIGURE 4.6: Optical pumping scheme for moving  $^{87}\text{Rb}$  atoms into  $|F = 2, m_F = 2\rangle$  state. Light polarization is defined with respect to magnetic field direction. Only transitions involved in pumping are shown.

of atoms in the  $m_f = 1$  state reduces spin-flip collisions and their associated losses [65].

Making the magnetic trap center coincide with the center of the optical molasses cloud prevents sloshing during MT loading; this can cause heating and atom losses. To make sure that centers match, we scanned the bias fields and optimized them for the lowest temperature configuration.

As preparation for evaporation cooling, we compress the magnetic trap and measure its lifetime.

### MT compression

The efficiency of evaporation cooling depends on elastic collision rates. To increase collision rate, we adiabatically compress the magnetic trap. In other words, we ramp its gradient linearly to 176.4 G/cm in 100 ms. Atomic density growth increases the average collision rate to 4.8 collisions per second, enough to start evaporation. At the same time the atomic cloud temperature increases from  $50 \mu\text{K}$  up to  $450 \mu\text{K}$ . Because of losses, only  $8.5 \times 10^8$  atoms are left in the magnetic trap after the compression

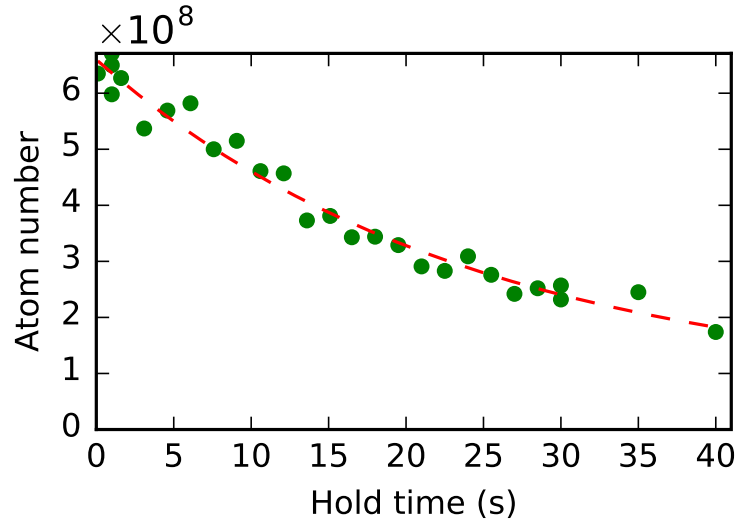


FIGURE 4.7: The number of atoms left in the compressed magnetic trap (176.4 G/cm) after various holding times. The dashed line is an exponential fit to the data. From the fit, the trap lifetime is 24.3 s.

stage. So, the evaporative cooling stage begins with phase-space density and average collision rate equal to  $8 \times 10^{-8}$  and 4.8 coll/s, respectively.

### Magnetic trap lifetime

The optimal duration of forced evaporative cooling from a quadrupole magnetic trap depends on the trap lifetime. To be efficient, with respect to phase-space density growth, the evaporative cooling duration should not exceed the trap lifetime [66]. The main factors that cause reduced magnetic trap lifetime include both trapped atom collisions with background ones, and stray resonant light scattering by trapped atoms [67]. That is why a good vacuum is necessary for this kind of experiment.

To measure magnetic trap lifetimes, we hold atoms in a fully compressed trap for various times. For each trap duration the remaining atom number is recorded (Fig. 4.7). An exponential fit to the data shows a magnetic trap lifetime  $\tau_{MT}=24.3$  s, which is typical in our experiments.

## 4.5 Evaporative cooling

In our experiment we do evaporative cooling in two stages: radio frequency (RF)-induced evaporation from the quadrupole magnetic trap and forced evaporation from the crossed beam optical dipole trap. This was done to avoid Majorana losses at the latest stages of RF evaporation and to achieve a Bose-Einstein condensate in a purely optical trap.

### 4.5.1 Radio frequency induced evaporation from quadrupole magnetic trap

During RF evaporation we hold atoms in the magnetic trap and illuminate them with radiofrequency radiation. Since the frequency of the radiation changes during the process, besides evaporation duration, the important parameters also are start and end frequencies, and the shape of the path between them. Initial parameters were taken from descriptions of similar setups [58, 56, 68] and optimized experimentally for our setup. Evaporation and all optimization for it were done in the compressed 176.4 G/cm trap.

To define the starting frequency for RF evaporation, we hold atoms in the trap for 1 s and illuminate them with constant-frequency RF radiation. We start with 40 MHz and for each subsequent sequence lower it by 1 MHz. Atom number in the trap remains the same until 25 MHz; after that it drops. This means we "touch" the outer shell of the cloud at 25 MHz, which defines the starting point for RF evaporation.

The end point was initially set to the lowest value at which we still were able to see a cloud of good quality. In our case this was 1 MHz. When the optical dipole trap was set up and aligned, the optimal end frequency was found to be 0.7 MHz by maximizing atom number transferred to ODT and minimizing their temperature.

The first working evaporation path was a linear sweep in frequency from 25 MHz to 1 MHz in 3 s. During optimization it was split in five steps and the final configuration is:

- Step 1: linear frequency sweep from 25 MHz to 10 MHz in 4 s; magnetic trap gradient 176.4 G/cm.

- Step 2: linear frequency sweep from 10 MHz to 7 MHz in 0.3 s; magnetic trap gradient 176.4 G/cm.
- Step 3: linear frequency sweep from 7 MHz to 4 MHz in 0.5 s; magnetic trap gradient 176.4 G/cm.
- Step 4: linear frequency sweep from 4 MHz to 2.1 MHz in 0.3 s, magnetic trap gradient 176.4 G/cm.
- Step 5: Decompression – linear frequency sweep from 2.1 MHz to 0.7 MHz in 0.4 s; magnetic trap gradient is linearly removed from 176.4 G/cm to 0.

As a consequence of RF evaporation, the temperature drops to  $\sim 10 \mu\text{K}$ , the atom number to  $\sim 10^7$ , while the phase-space density and average collision rate increase to  $10^{-2}$  and 400 coll/s, respectively (Fig.4.8). The evaporation steps were optimized to provide phase-space density growth during the process (Fig. 4.9).

The efficiency of our RF evaporation path was estimated as  $\eta = 2.93$  using formula (2.19). It was checked for the described above path but without decompression during fifth step.

### **Transfer to ODT and Decompression.**

When atoms become colder they spend more time near the magnetic trap center, which increases Majorana losses. The coldest atoms are lost from the trap center, making evaporation less efficient. So, at that point we start transferring to the optical dipole trap.

At the beginning of the third RF evaporation step, we turn on the ODT power at 100% which is equally distributed between two beams. As the atoms are held by the optical trap, the magnetic field can be removed. Along with the main trapping gradient, bias fields should be removed. This must be done carefully to avoid cloud sloshing, which causes atomic losses, heating and inefficient transfer to the ODT. So, the currents in all coils (trapping and bias) are linearly ramped to 0 during 0.3 s. during the last RF evaporation step. As a result, the atomic cloud sits in a pure optical trap and further cooling can be done. When the atoms are transferred from a linear to a harmonic trap, the density of states is modified in such a way that it leads

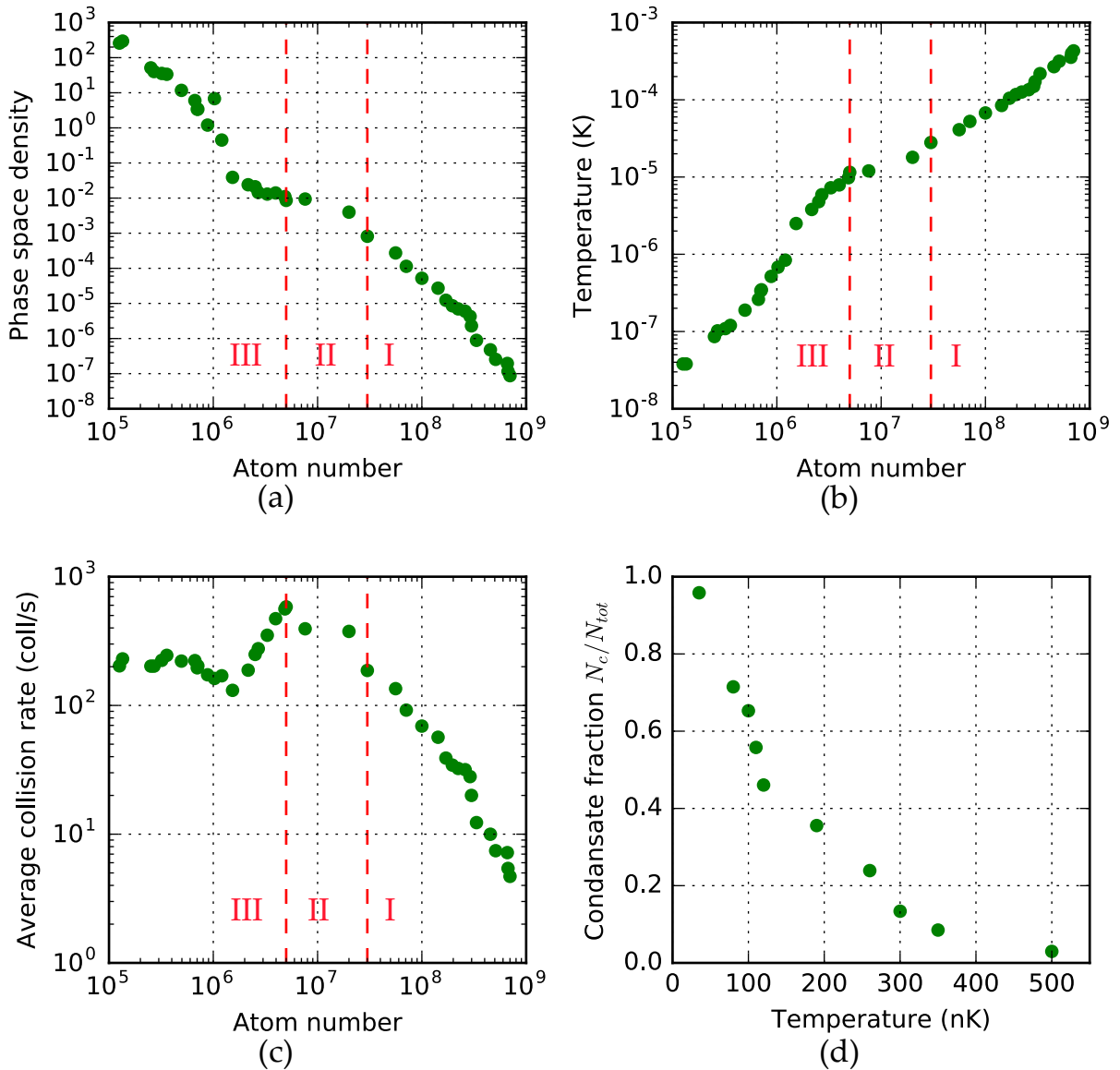


FIGURE 4.8: Characteristics of the evaporation cooling. The first three graphs show how phase space density (a), temperature (b) and average collision rate (c) change as atoms are removed from the traps during radio frequency-induced evaporation from the magnetic trap (region I), decompression and transfer to the ODT (region II), and forced evaporation from the ODT (region III). (d) Graph shows the fraction of BEC in the cloud achieved at different temperatures with ODT evaporation. It represents one measurement for each temperature. Statistical uncertainties in atom number and temperature are on the order of 10%.

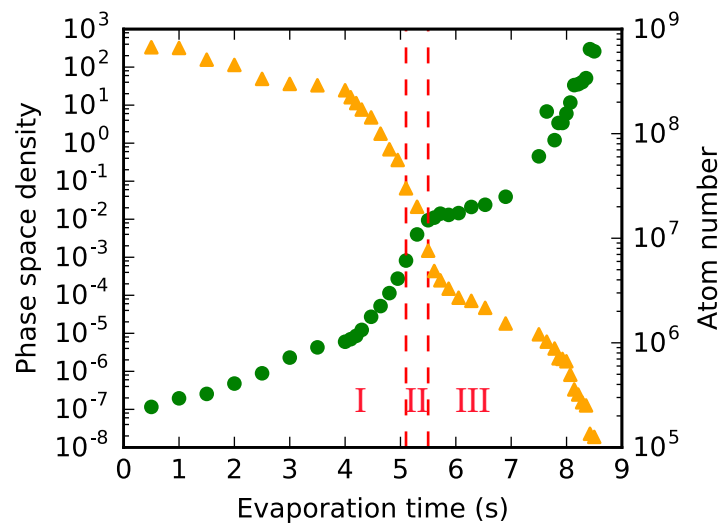


FIGURE 4.9: Phase space density (green dots) and atom number (yellow triangles) change as function of evaporation time. The graph is split in three regions: RF induced evaporation from the magnetic trap (region I), into decompression and transfer to optical dipole trap (region II), and evaporation from ODT (region III).

to a jump in phase-space density [58]. A gain factor of 30 was observed in a similar experiment [50].

## 4.5.2 Forced evaporation from optical-dipole trap: Achieving BEC

Two Gaussian beams, crossed at 90 degrees, are used to form the optical dipole trap. Each of the beams has a waist of  $75 \mu\text{m}$  and a maximal power inside the science chamber of 2.6 W. This creates a trap for the atoms with a depth of  $76 \mu\text{K}$ .

After loading in the ODT, the average atomic density reaches  $8 \times 10^{13}$  particles/ $\text{cm}^3$ . In such a dense cloud, three-body collisions become significant. That is why the optical dipole trap lifetime is only 3 s. The trap lifetime limits the duration of evaporation from the optical trap. We split up the evaporation process into two steps:

- Step 1: exponentially lowering the ODT power (with  $\tau = -1$  s) from 100% (2.6 W per beam) to 20% (0.52 W per beam) during 2 s.
- Step 2: linearly lowering the ODT power from 20% to 13% during 1 s.

The resulting changes in PSD, temperature and collision rate of this evaporation path are shown in Fig. 4.8. After the first, the cloud remains thermal. The transition point is around 17.5 - 18% of the ODT power. Here, the phase-space density surpasses 1.2 and the cloud temperature reaches the calculated critical temperature  $T_c = 286$  nK. By the end of the second step we get a pure Bose-Einstein condensate with  $10^5$  atoms (Fig. 4.10). The temperature of the remaining thermal cloud is approximately 40 nK. By changing the final evaporation power we can control the fraction of BEC in the cloud (Fig. 4.8 d).

### Trap frequency

Since the ODT beams cross inside the glass chamber, we don't have any possibility of measuring beams parameters directly, at the crossing point. To double check if the estimated parameters for the beams are correct, we measure the frequency of the optical dipole trap. Experimental value then can be compared with those calculated from beam parameters using Eq. (2.11). We measure the trap frequency using 20% of the maximum ODT power. The cloud is evaporated with usual path until 13.5% of

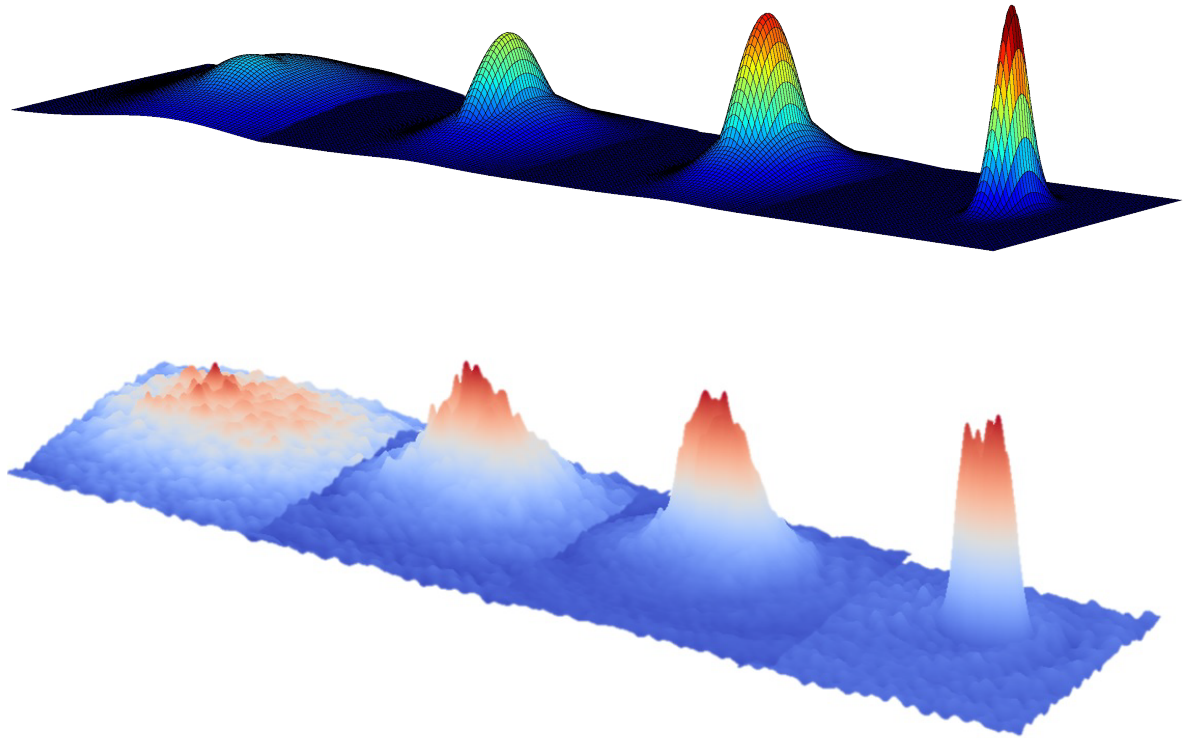


FIGURE 4.10: Velocity distribution for thermal, transition and condensed clouds. On the bottom image experimental data is presented, on the top one - fit to data. On both images from left to right: thermal cloud, evaporation was stopped at 20% ; two transition clouds with a clear bi-modal distribution, fraction of BEC = 32.4% and 44.2%, evaporation was stopped at 15% and 14.5%, respectively; quasi pure (90%) Bose-Einstein condensate with  $10^5$  atoms and radius  $20 \mu\text{m}$ ; evaporated until 13% of ODT power. Images were taken after 26 ms of free expansion. Image credit: Dr. Lindsay LeBlanc.

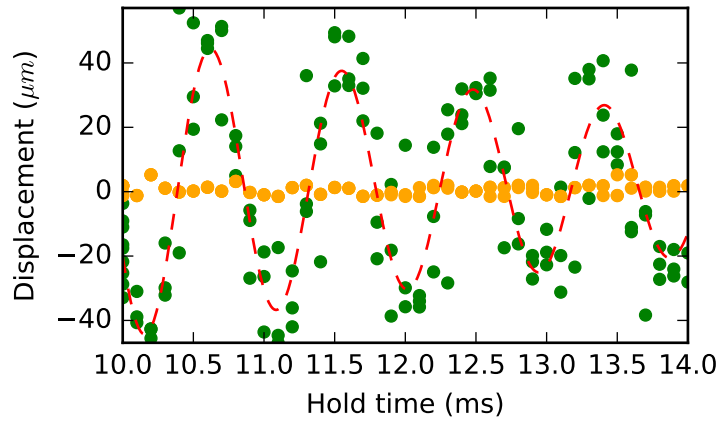


FIGURE 4.11: Optical dipole trap frequency measurements. The green dots represent the displacement of the cloud when the trap was shaken. Yellow dots represent control data taken without shaking the trap. Measurements were done for 20% of power. The red-dashed fit curve shows trap frequency  $\omega_x/2\pi = 107$  Hz, which is compatible with the calculated value of 110 Hz.

ODT power. Then, the power is rapidly increased to 20%. This fast change pushes the atomic cloud and it starts to oscillate inside the trap. The cloud is held inside the trap for different amounts of time, and released. The displacement along the  $X$ -direction was recorded for each holding time. Time-of-flight was kept constant during measurements so that the vertical displacement was always the same. Without shaking the cloud, identical time-of-flight measurements were performed to be sure that the oscillations were caused by us (Fig. 4.11). The measured value for radial trap frequency at 20% of the ODT power  $\omega_x/2\pi = 107$  Hz. This is close to the calculated trap frequency for this configuration:  $\omega_x/2\pi = 110$  Hz.

## 4.6 BEC signatures

There are two features that can be observed only in the condensate regime and are used as undeniable BEC signatures: an inversion of aspect ratio during free expansion, and a bimodal velocity distribution of atoms.

### 4.6.1 Aspect ratio inversion during free expansion

The velocity distribution in a thermal cloud is a Maxwell-Boltzmann distribution and is isotropic. This kind of cloud, when released from a trap, eventually takes a spherical shape.

Unlike thermal clouds, the kinetic energy in a condensed cloud can be neglected. Thus the expansion of a BEC is defined by its interaction energy. Repulsive forces (and the initial acceleration in a free expansion) in a condensate are proportional to the density gradient [4]. Stronger confinement causes a higher density gradient and consequently a higher acceleration after releasing the cloud from the trap.

For small or non-interacting condensates, where interactions can be neglected, the aspect ratio inversion arises from the Heisenberg uncertainty principle: higher spatial confinement leads to broader momentum distribution [69].

In both cases the BEC, initially elongated in the weak direction of the anisotropic trap, expands faster in the orthogonal, strong-confinement direction when released from the trap. As a result, its aspect ratio inverts. A quantitative description of the process can be found in [69, 70, 54, 71].

When both optical dipole trap beams have the same power they create an isotropic trap that is symmetrical in the radial direction. That is why the condensate has the same size in the  $X$ - and  $Y$ - directions and looks round from the bottom camera. In this case, aspect ratio inversion cannot be observed. So, we change the balance between the ODT beams to make the trap anisotropic. In the usual cooling cycle, the BEC is produced by evaporation in the ODT until 13% of trap's maximum power with equal power in both trapping beams. Then, over the next 200 ms we change the balance between the beams. To compensate for the power drop that occurs in the weaker beam, we simultaneously ramp up the total power to 14%. As a result, the BEC cloud acquires the shape of a cigar. Fig. 4.12 shows the free expansion of a cigar-shaped cloud, with the aspect ratio inversion is clearly visible.

### 4.6.2 Bimodality in velocity distribution

An atomic cloud above critical temperature is governed by Maxwell-Boltzmann statistics. The velocities of thermal atoms are normally distributed and can be described

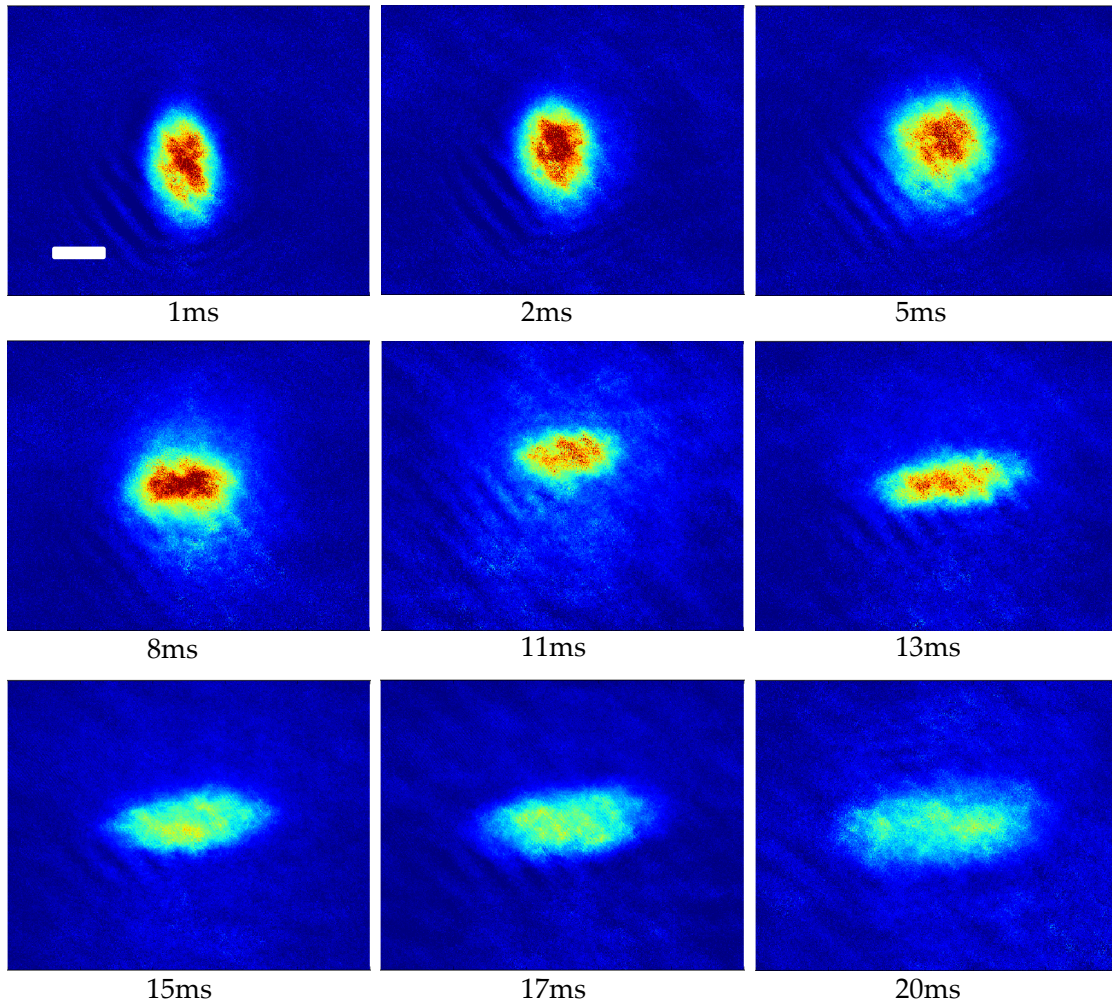


FIGURE 4.12: Inversion of aspect ratio in free expanding BEC cloud released from an anisotropic optical trap. The time of free expansion is indicated under each image. Images were taken using the vertical imaging system, meaning the cloud falls into the camera. The scale bar is equal to  $150 \mu\text{m}$ . Image credit: Dr. Lindsay LeBlanc.

with Gaussian function.

The velocity distribution in a condensate cannot be described by a Gaussian. As was discussed in previous section, the velocity distribution in a condensate depends on the initial atomic density distribution, this kind of distribution given by a Thomas-Fermi function (Section 2.4.2). In a harmonic trap with axial symmetry, and this kind of distribution has the shape of an inverted parabola.

Since the thermal and condensed clouds have distinct velocity distributions, a bimodality of the velocity distribution appears in clouds that include both thermal and condensed phases. This phenomena is used as a BEC signature.

To check for a bimodal distribution, four clouds were prepared: with 32.4%, 44.2% and 90% fraction of BEC and thermal cloud for comparison (Fig. 4.10). The thermal cloud is perfectly fitted with Gaussian function. In addition, the pure BEC is fitted with an inverted parabola. In the case of thermal-condensate mixture, the bimodal distribution is clearly visible: the condensate's parabola sits on top of the Gaussian that corresponds to thermal atoms.

After implementation and optimization of laser cooling and trapping, magnetic trapping and finally evaporative cooling, we are able to produce BECs of  $N = 10^5$  atoms and  $T \leq 40$  nK in our system.

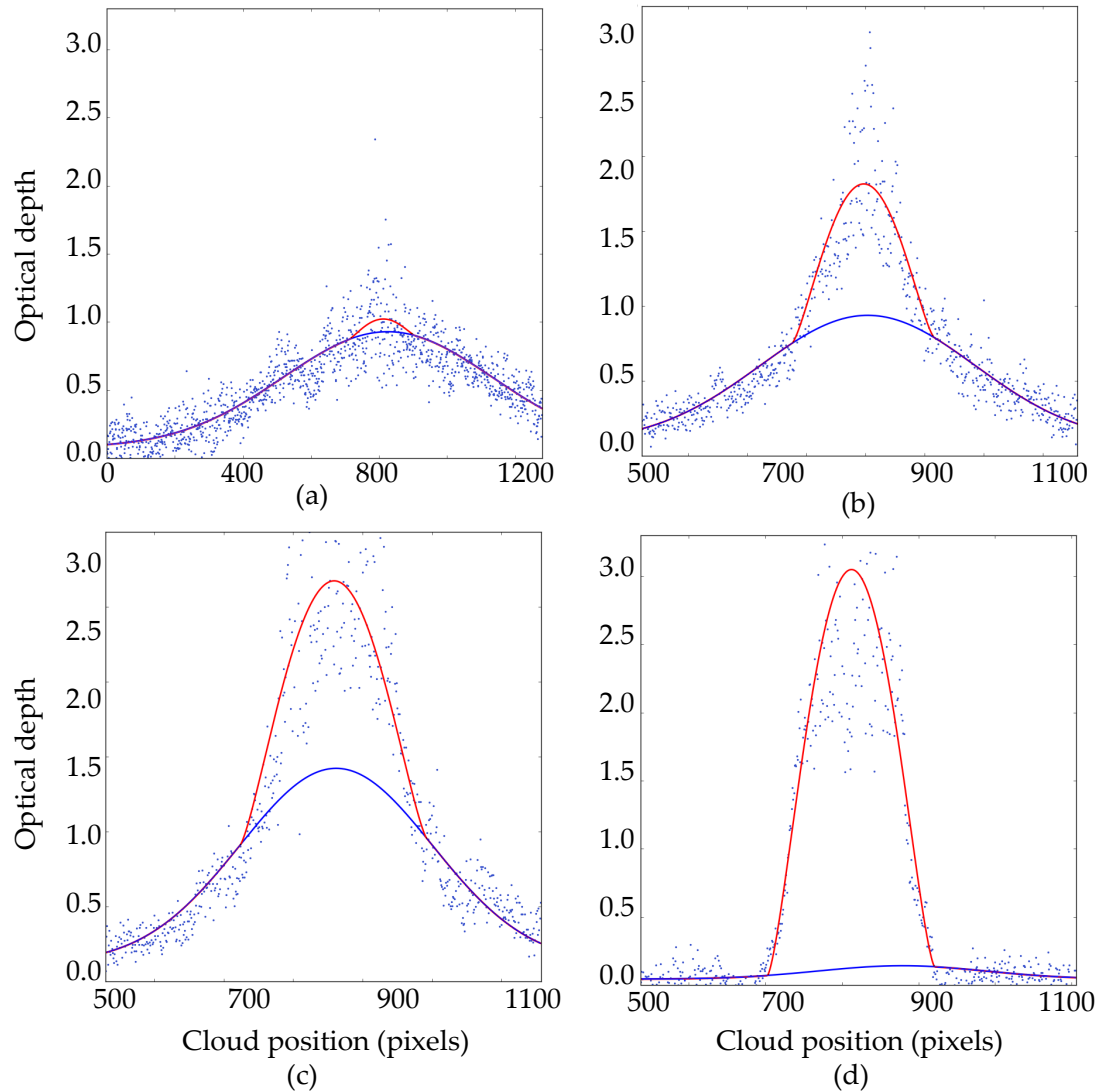


FIGURE 4.13: Bimodal fits to the cross sections of the clouds with different condensate fraction: (a) thermal cloud; (b) fraction of BEC = 32.4%; (c) fraction of BEC = 44.2%; (d) pure (90%) Bose-Einstein condensate. The cross sections correspond to the stages presented in Fig.4.10. Fits to a Gaussian (blue) and an inverted parabola (red) are shown.

## Chapter 5

### Conclusions

In conclusion, we built an ultracold quantum gases apparatus that is able to produce a Bose-Einstein condensate in an optical trap with  $10^5$   $^{87}\text{Rb}$  atoms every 30 s.

To achieve quantum degeneracy atomic cloud is formed by a hybrid 2D-3D-MOT system that precools the system to  $500\ \mu\text{K}$ . After the MOT stage, the cloud is cooled below the Doppler limit to  $50\ \mu\text{K}$  with polarization gradient cooling in optical molasses. Since the limit for laser cooling is reached here, the atoms are further cooled by evaporation cooling. First, RF evaporation from the quadrupole magnetic trap cools the atoms to a temperature around  $10\ \mu\text{K}$ . Then, forced evaporation from the ODT reduces the temperature to  $286\ \text{nK}$  and condensation starts. With further evaporation, the temperature drops to  $40\ \text{nK}$  and the BEC fraction increases to  $\sim 90\%$ .

In the future, the experimental steps can be further optimized to lower the time of each sequence or/and increase atom number in condensate, but as it is, the apparatus is basically ready to move to direct experiments with ultracold atoms and BECs.

As first experiments with the rubidium BEC, spin-orbit coupling using Raman transition [28, 72] and studying vortex formation [29, 73] are planned. For that, tunable a Ti-sapphire laser was installed and its optical setup is finished.

A main goal for future is to achieve BEC with  $^{39}\text{K}$  [74, 75]. But potassium can not be evaporatively cooled efficiently, so it will be cooled sympathetically with rubidium [7].  $^{39}\text{K}$  has atomic transitions at different from  $^{87}\text{Rb}$  wavelengths. In addition, hyperfine splitting of its  $D2$  excited level is very narrow and for cooling  $D1$  line is used [76, 77, 78, 79]. So, to perform experiments with potassium we need a new

---

laser system, which is in progress now. These technical challenges are worth it because potassium interatomic interactions can be conveniently tuned with Feshbach resonances [80, 81] which, in conjunction with spin-orbit coupling, will open possibility to perform interesting experiments in many-body physics [82, 83] looking at phases related to magnetism and superfluidity.

As a possible parallel research direction, experiments in slowing, stopping and storing light with ultracold atoms or even BECs might also be performed.

# Bibliography

- [1] M. H. Anderson et al. "Observation of Bose-Einstein condensation in a dilute atomic vapor". In: *Science* 269.5221 (1995), p. 198.
- [2] D. G. Fried et al. "Bose-Einstein condensation of atomic hydrogen". In: *Physical Review Letters* 81.18 (1998), p. 3811.
- [3] C. C. Bradley et al. "Evidence of Bose-Einstein condensation in an atomic gas with attractive interactions". In: *Physical Review Letters* 75.9 (1995), p. 1687.
- [4] K. B. Davis et al. "Bose-Einstein condensation in a gas of sodium atoms". In: *Physical Review Letters* 75.22 (1995), p. 3969.
- [5] G. Roati et al. "<sup>39</sup>K Bose-Einstein condensate with tunable interactions". In: *Physical Review Letters* 99.1 (2007), p. 010403.
- [6] S. Kraft et al. "Bose-Einstein Condensation of Alkaline Earth Atoms: <sup>40</sup>Ca". In: *Physical Review Letters* 103.13 (2009), p. 130401.
- [7] G. Modugno et al. "Bose-Einstein condensation of potassium atoms by sympathetic cooling". In: *Science* 294.5545 (2001), pp. 1320–1322.
- [8] Q. Beaufils et al. "All-optical production of chromium Bose-Einstein condensates". In: *Physical Review A* 77.6 (2008), p. 061601.
- [9] S. Stellmer et al. "Bose-Einstein condensation of strontium". In: *Physical Review Letters* 103.20 (2009), p. 200401.
- [10] S. L. Cornish et al. "Stable <sup>85</sup>Rb Bose-Einstein condensates with widely tunable interactions". In: *Physical Review Letters* 85.9 (2000), p. 1795.
- [11] S. Stellmer et al. "Bose-Einstein condensation of <sup>86</sup>Sr". In: *Physical Review A* 82.4 (2010), p. 041602.
- [12] P. G. Mickelson et al. "Bose-Einstein condensation of <sup>88</sup>Sr through sympathetic cooling with <sup>87</sup>Sr". In: *Physical Review A* 81.5 (2010), p. 051601.

- 
- [13] T. Weber et al. "Bose-Einstein condensation of cesium". In: *Science* 299.5604 (2003), pp. 232–235.
- [14] M. Lu et al. "Strongly dipolar Bose-Einstein condensate of dysprosium". In: *Physical Review Letters* 107.19 (2011), p. 190401.
- [15] K Aikawa et al. "Bose-Einstein condensation of erbium". In: *Physical Review Letters* 108.21 (2012), p. 210401.
- [16] S. Sugawa et al. "Bose-Einstein condensate in gases of rare atomic species". In: *Physical Review A* 84.1 (2011), p. 011610.
- [17] G.-B. Jo et al. "Matter-wave interferometry with phase fluctuating Bose-Einstein condensates". In: *Physical Review Letters* 99.24 (2007), p. 240406.
- [18] T Schumm et al. "Matter-wave interferometry in a double well on an atom chip". In: *Nature physics* 1.1 (2005), pp. 57–62.
- [19] P. Navez et al. "Matter-wave interferometers using TAAP rings". In: *New Journal of Physics* 18.7 (2016), p. 075014.
- [20] N. Rosanov et al. "Applications of Bose-Einstein condensate soliton states to quantum metrology and nanotechnology". In: *Quantum Electronics Conference, 2003. EQEC'03. European*. IEEE. 2003, p. 307.
- [21] M Schioppo et al. "Ultrastable optical clock with two cold-atom ensembles". In: *Nature Photonics* (2016).
- [22] S Bize et al. "Cold atom clocks and applications". In: *Journal of Physics B: Atomic, molecular and optical physics* 38.9 (2005), S449.
- [23] J. Abo-Shaeer et al. "Observation of vortex lattices in Bose-Einstein condensates". In: *Science* 292.5516 (2001), pp. 476–479.
- [24] M. R. Matthews et al. "Vortices in a Bose-Einstein condensate". In: *Physical Review Letters* 83.13 (1999), p. 2498.
- [25] D. Frantzeskakis. "Dark solitons in atomic Bose-Einstein condensates: from theory to experiments". In: *Journal of Physics A: Mathematical and Theoretical* 43.21 (2010), p. 213001.

- 
- [26] S. Burger et al. “Dark solitons in Bose-Einstein condensates”. In: *Physical Review Letters* 83.25 (1999), p. 5198.
- [27] V. Galitski and I. B. Spielman. “Spin-orbit coupling in quantum gases”. In: *Nature* 494.7435 (2013), pp. 49–54.
- [28] Y.-J. Lin et al. “Bose-Einstein condensate in a uniform light-induced vector potential”. In: *Physical Review Letters* 102.13 (2009), p. 130401.
- [29] Y.-J. Lin et al. “Synthetic magnetic fields for ultracold neutral atoms”. In: *Nature* 462.7273 (2009), pp. 628–632.
- [30] L. V. Hau et al. “Light speed reduction to 17 metres per second in an ultracold atomic gas”. In: *Nature* 397.6720 (1999), pp. 594–598.
- [31] C. Liu et al. “Observation of coherent optical information storage in an atomic medium using halted light pulses”. In: *Nature* 409.6819 (2001), pp. 490–493.
- [32] D. Tiarks et al. “Optical  $\pi$  phase shift created with a single-photon pulse”. In: *Science Advances* 2.4 (2016), e1600036.
- [33] S. Wildermuth et al. “Bose–Einstein condensates: microscopic magnetic-field imaging”. In: *Nature* 435.7041 (2005), pp. 440–440.
- [34] J. Dalibard and C. Cohen-Tannoudji. “Atomic and Molecular Beams, The State of Art 2000”. In: ed. by R. Campargue. Springer-Verlag, 2001. Chap. Laser Cooling and Trapping of Neutral Atoms, pp. 43–62.
- [35] T. W. Hänsch and A. L. Schawlow. “Cooling of gases by laser radiation”. In: *Optics Communications* 13.1 (1975), pp. 68–69.
- [36] C. J. Foot. *Atomic physics*. Vol. 7. Oxford University Press, 2005.
- [37] A. Tretiakov. “Versatile apparatus for ultracold atomic hybrid systems”. MSc thesis. University of Alberta, 2016.
- [38] W. D. Phillips and H. Metcalf. “Laser deceleration of an atomic beam”. In: *Physical Review Letters* 48.9 (1982), p. 596.
- [39] J. V. Prodan, W. D. Phillips, and H. Metcalf. “Laser production of a very slow monoenergetic atomic beam”. In: *Physical Review Letters* 49.16 (1982), p. 1149.

- 
- [40] K. J. Günter. "Design and implementation of a Zeeman slower for  $^{87}\text{Rb}$ ". In: *Report, Ecole Normale Supérieure, Paris* (2004).
- [41] W Ertmer et al. "Laser manipulation of atomic beam velocities: Demonstration of stopped atoms and velocity reversal". In: *Physical Review Letters* 54.10 (1985), p. 996.
- [42] S. Chu et al. "Three-dimensional viscous confinement and cooling of atoms by resonance radiation pressure". In: *Physical Review Letters* 55.1 (1985), p. 48.
- [43] P. D. Lett et al. "Optical molasses". In: *JOSA B* 6.11 (1989), pp. 2084–2107.
- [44] J. Dalibard and C. Cohen-Tannoudji. "Laser cooling below the Doppler limit by polarization gradients: simple theoretical models". In: *JOSA B* 6.11 (1989), pp. 2023–2045.
- [45] H. J. Metcalf and P. van der Straten. "Laser cooling and trapping of atoms". In: *JOSA B* 20.5 (2003), pp. 887–908.
- [46] R. Grimm, M. Weidemüller, and Y. B. Ovchinnikov. "Optical dipole traps for neutral atoms". In: *Advances in atomic, molecular, and optical physics* 42 (2000), pp. 95–170.
- [47] H Daerr et al. *Ultra-Trace analysis of krypton-85*. Tech. rep. Funding organisation: Deutsche Stiftung Friedensforschung (DSF)(Germany), 2010.
- [48] H. J. Metcalf and P. Straten. *Laser cooling and trapping of neutral atoms*. Wiley Online Library, 2007.
- [49] K. Dieckmann. "Bose-Einstein condensation with high atom number in a deep magnetic trap". PhD thesis. Van der Waals-Zeeman Institute, 2001.
- [50] A. Marchant et al. "Bose-Einstein condensation of  $^{85}\text{Rb}$  by direct evaporation in an optical dipole trap". In: *Physical Review A* 85.5 (2012), p. 053647.
- [51] C.-L. Hung et al. "Accelerating evaporative cooling of atoms into Bose-Einstein condensation in optical traps". In: *Physical Review A* 78.1 (2008), p. 011604.
- [52] D. Rychtarik. "Two-dimensional Bose-Einstein Condensate in an optical surface trap". PhD thesis. University of Innsbruck, 2004.

- [53] F. Dalfovo et al. "Theory of Bose-Einstein condensation in trapped gases". In: *Reviews of Modern Physics* 71.3 (1999), p. 463.
- [54] Y Castin and R Dum. "Bose-Einstein condensates in time dependent traps". In: *Physical Review Letters* 77.27 (1996), p. 5315.
- [55] J. F. O'Hanlon. *A user's guide to vacuum technology*. John Wiley & Sons, 2005.
- [56] K. Jiménez-García. "Engineering Hamiltonians for Ultracold Neutral Atoms". PhD thesis. Joint Quantum Institute National Institute of Standards, Technology, and the University of Maryland, 2012.
- [57] R. C. Brown et al. "Note: Pneumatically actuated and kinematically positioned optical mounts compatible with laser-cooling experiments". In: *Review of Scientific Instruments* 84.9 (2013), p. 096101.
- [58] Y.-J. Lin et al. "Rapid production of  $^{87}\text{Rb}$  Bose-Einstein condensates in a combined magnetic and optical potential". In: *Physical Review A* 79.6 (2009), p. 063631.
- [59] S. J. Park, J. Noh, and J. Mun. "Cold atomic beam from a two-dimensional magneto-optical trap with two-color pushing laser beams". In: *Optics Communications* 285.19 (2012), pp. 3950–3954.
- [60] D. A. Steck. "Rubidium 87 d line data (2001)". In: URL <http://steck.us/alkalidata> 83 (2016).
- [61] K Dieckmann et al. "Two-dimensional magneto-optical trap as a source of slow atoms". In: *Physical Review A* 58.5 (1998), p. 3891.
- [62] T. Opdam. "Magneto-optical trap of  $^{39}\text{K}$ : setup and characterisation". Report of a 36 EC master project. University of Amsterdam, 2012.
- [63] C. Y. Park, M. S. Jun, and D. Cho. "Magneto-optical trap loaded from a low-velocity intense source". In: *JOSA B* 16.6 (1999), pp. 994–997.
- [64] A. Arnold. "Preparation and Manipulation of an  $^{87}\text{Rb}$  Bose-Einstein Condensate". PhD thesis. University of Sussex, 1999.
- [65] W. Ketterle and N. Van Druten. "Evaporative cooling of trapped atoms". In: *Advances in atomic, molecular, and optical physics* 37 (1996), pp. 181–236.

- [66] D. Frese. "Bose-Einstein Condensation of Rubidium: Towards Ultracold Binary Bosonic Mixtures". Dissertation zur Erlangung des Doktorgrades (Dr. rer. nat.) Rheinischen Friedrich-Wilhelms-Universität Bonn, 2005.
- [67] M. S. Yoon. "Experiments on magnetic transport, magnetic trapping, and Bose-Einstein condensate". PhD thesis. University of Oxford, 2009.
- [68] D. Yum et al. "Systematic study of the rf-induced evaporation of  $^{87}\text{Rb}$  atoms in a spherical magnetic quadrupole trap". In: *Journal of the Korean Physical Society* 60.1 (2012), pp. 1–5.
- [69] K. Gawryluk et al. "Free expansion of a Bose–Einstein condensate in the presence of a thermal cloud". In: *Journal of Physics B: Atomic, Molecular and Optical Physics* 43.10 (2010), p. 105303.
- [70] T. Tsurumi and M. Wadati. "Free Expansion of a Bose–Einstein Condensate". In: *Journal of the Physical Society of Japan* 71.4 (2002), pp. 1044–1051.
- [71] E. Castellanos and C. Escamilla-Rivera. "Modified uncertainty principle from the free expansion of a Bose–Einstein condensate". In: *Modern Physics Letters A* (2015), p. 1750007.
- [72] Y.-J. Lin, K Jiménez-García, and I. Spielman. "Spin-orbit-coupled Bose-Einstein condensates". In: *Nature* 471.7336 (2011), pp. 83–86.
- [73] L. LeBlanc et al. "Gauge matters: observing the vortex-nucleation transition in a Bose condensate". In: *New Journal of Physics* 17.6 (2015), p. 065016.
- [74] M. Landini et al. "Direct evaporative cooling of 39 K atoms to Bose-Einstein condensation". In: *Physical Review A* 86.3 (2012), p. 033421.
- [75] R. L. Campbell et al. "Efficient production of large K 39 Bose-Einstein condensates". In: *Physical Review A* 82.6 (2010), p. 063611.
- [76] D. Nath et al. "Quantum-interference-enhanced deep sub-Doppler cooling of 39 K atoms in gray molasses". In: *Physical Review A* 88.5 (2013), p. 053407.
- [77] M Landini et al. "Sub-Doppler laser cooling of potassium atoms". In: *Physical Review A* 84.4 (2011), p. 043432.
- [78] G. Salomon et al. "Gray-molasses cooling of 39K to a high phase-space density". In: *EPL (Europhysics Letters)* 104.6 (2014), p. 63002.

- 
- [79] G. Salomon et al. "All-optical cooling of K 39 to Bose-Einstein condensation". In: *Physical Review A* 90.3 (2014), p. 033405.
- [80] C. Chin et al. "Feshbach resonances in ultracold gases". In: *Reviews of Modern Physics* 82.2 (2010), p. 1225.
- [81] C. D'Errico et al. "Feshbach resonances in ultracold 39K". In: *New Journal of Physics* 9.7 (2007), p. 223.
- [82] W. S. Cole et al. "Bose-Hubbard models with synthetic spin-orbit coupling: Mott insulators, spin textures, and superfluidity". In: *Physical Review Letters* 109.8 (2012), p. 085302.
- [83] J Radić et al. "Exotic quantum spin models in spin-orbit-coupled Mott insulators". In: *Physical Review Letters* 109.8 (2012), p. 085303.